MODELING AND CHARACTERIZATION OF MOBILE-TO-MOBILE COMMUNICATION CHANNELS

by

Muhammad Riaz
PE093010

A thesis submitted to the
Department of Electrical Engineering
in partial fulfillment of the requirements for the degree of
DOCTOR OF PHILOSOPHY IN ELECTRICAL ENGINEERING

Faculty of Engineering
Mohammad Ali Jinnah University
Islamabad
October 2015

i

Dedicated to my beloved grandparents' memories, parents, family and brothers.

ACKNOWLEDGMENT

ABSTRACT

Geometrical propagation channel modeling has a pivotal role in designing most of the emerging wireless communication systems. Scattering is usually considered one of the major phenomena in affecting the propagation of radio signals. The effects of this phenomenon are more severe in mobile-to-mobile (M2M) communication environment because of the large number of scattering objects that reside around both mobile stations (MSs). In recent years, researchers have made significant efforts to model these effects either by their physical description or by their probabilistic trend. Geometrically based spatial scattering modeling is one such popular methodology used so far.

This dissertation focuses on modeling the 3D spatio-temporal channel characteristics for mobile-to-mobile(M2M) communication environment and presents mathematical expressions for their joint and marginal probability distributions. The proposed model is also analyzed for the characterization of Doppler spectrum.

The dissertation begins with the proposal of a 3D semi-ellipsoid geometrical channel model for M2M radio propagation environment assuming uniformly distributed scatterers around the mobile stations (MSs) within the defined regions. In order to model M2M communication environment realistically, a flexible geometry of the semi-ellipsoids is employed whose dimensions are made adjustable and rotatable about their vertical axes according to the directions of the MSs and the shapes of the streets and canyons where MSs reside. Using the proposed geometrical channel model, mathematical expressions for the joint and marginal probability distribution functions (PDFs) of angle-of-arrival (AoA) and time-of-arrival (ToA) in azimuth and elevation planes are derived. Mobility, being an important parameter in radio mobile channel modeling, is also analyzed through the characterization of Doppler spectrum of the proposed channel model. Furthermore, a generalized 3D geometrical channel model is also proposed for M2M communication environment. The generalized 3D spatial channel model consists of independently rotatable concentric semi-ellipsoids such that the inner semi-ellipsoids are scatter-free regions and uniformly distributed scatterers reside outside the inner and inside the outer semi-ellipsoids. By exploiting the proposed generalized 3D channel model, mathematical expressions for the joint and marginal PDFs of AoA and ToA in azimuth and elevation planes are derived. These spatial and temporal characteristics are analyzed for various channel parameters like elevation and orientation of each of the semi-ellipsoids.

The model is validated through its comparison with simulation results and measurement campaigns reported in the literature. Moreover, generalization of the model is confirmed by its comparisons with various existing geometrical models. It is shown that some notable geometrical channel models for F2M and M2M communication environments in the literature can be deduced from the proposed

generalized model through the substitution of certain suitable values for a few channel parameters.

LIST OF PUBLICATIONS

[**J01**] **M. Riaz**, S. J. Nawaz, and Noor M. Khan, "3D Ellipsoidal model for M2M radio propagation environments," *Wireless Pers. Commun.*, vol. 72, no. 4, pp. 2465-2479, Oct. 2013. [ISI impact factor: 0.979]

[**J02**] **M. Riaz**, S. J. Nawaz, and Noor M. Khan, "A generalized 3D scattering channel model for spatio-temporal statistics in mobile-to-mobile communication environment," *IEEE Trans. Veh. Technol.*, vol. 64. no. 10, Oct. 2015, DOI=10.1109/TVT.2014.2371531. [ISI impact factor: 2.64]

[**J03**] S. J. Nawaz, **Muhammad Riaz**, and Noor M. Khan, "Temporal Analysis of a 3D Ellipsoid Channel Model for the Vehicle-to-Vehicle Communication Environments," *Wireless Pers. Commun.*, vol. 82, no. 3, pp. 1337-1350, June 2015. [ISI impact factor: 0.979]

[**J04**] **M. Riaz**, S. J. Nawaz, and Noor M. Khan, "Doppler Spectrum Analysis of a 3D Ellipsoid Channel Model for the Mobile-to-Mobile Communication Environment," Submitted in *"Frequenz - Journal of RF engineering and telecommunications"*. [ISI impact factor: 0.393]

TABLE OF CONTENTS

LIST OF FIGURES

LIST OF TABLES

LIST OF ACRONYMS

VANET	Vehicular Ad Hoc Network
MANET	Mobile Ad Hoc Network
WSN	Wireless Sensor Network
ITS	Intelligent Transportation System
M2M	Mobile-to-Mobile
F2M	Fixed-to-Mobile
V2V	Vehicle-to-Vehicle
2D	Two Dimensional
3D	Three Dimensional
AoA	Angle-of-Arrival
AoD	Angle-of-Departure
ToA	Time of Arrival
MS	Mobile Station
BS	Base Station
Tx	Transmitter
Rx	Receiver
LCR	Level Crossing Rate
AFD	Average Fade Duration
TDL	Tape-delay-line
PDF	Probability Distribution Function
CDF	Cumulative Distribution Function
ISI	Inter Symbol Interference
LoS	Line-of-Sight
NLoS	Non-Line-of-Sight
MIMO	Multiple-Input Multiple-Output
SISO	Single-Input Single-Output
PAS	Power Azimuth Spectrum
PDS	Power Density Spectrum
DS	Doppler Shift

Chapter 1

INTRODUCTION

This chapter begins with an overview of mobile-to-mobile (M2M) communications given in Section 1.1 and proceed towards the significance of the research study and the aims behind this study presented Section 1.2 and 1.3, respectively. Problem statement that motivates the authors for its solution as the outcome of this research work is also given in Section 1.3. The methodology to accomplish the targeted research study is presented in detail is Section 1.4. A brief summary of research contributions contained in this dissertation is given in Section 1.5. Research articles related to the research work included in this dissertation are listed in Section 1.6. Finally, a brief layout of the dissertation is provided in Section 1.7.

1.1 Overview of M2M Communications

Mobile-to-mobile (M2M) communications has recently generated considerable research interest due to its role in emerging paradigms of wireless networks such as wireless sensor networks (WSN) [4], mobile ad hoc networks (MANET) [5], vehicular ad-hoc networks (VANET) [6] and the intelligent transportation system (ITS) [7]. Mobile-to-Mobile (M2M) communication channels differ from conventional fixed-to-mobile (F2M) cellular radio channels, where the base station (BS) is stationary and mounted on elevated structure as shown in Fig. 1.1 [8] whereas in M2M communications, the transmitter (Tx) and receiver (Rx) are both mobile and can communicate directly with one another without requiring an intermediary fixed BS [9, 10]. In M2M communication environment, both the mobile stations are equipped with low elevated antennas and are usually surrounded by local scatterers as shown in Fig. 1.2.

Another characteristic which makes M2M communications different from F2M communications is the enhanced Doppler shift, that results from the motion of the two mobile stations instead of one mobile station as in F2M cellular communication
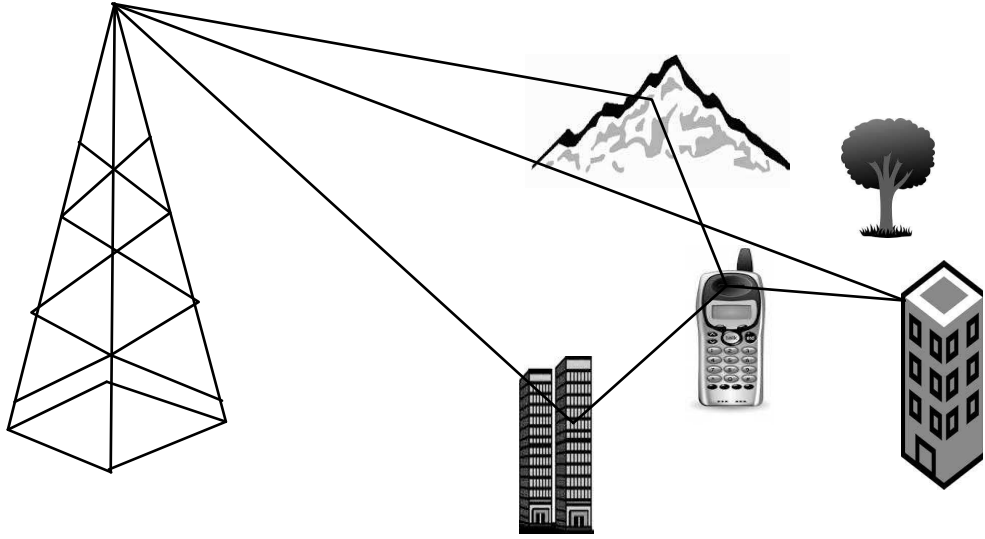
FIGURE 1.1: Example scattering environment around MS in F2M propagation channels.

systems. In M2M communications, the total Doppler shift is equal to the sum of the Doppler shifts due to the motion of transmitting and receiving mobile stations [11]. If α_t and α_r are the directions of velocities v_t and v_r of the transmitting and receiving mobile stations along the signal arrival then the total Doppler shift produced in the carrier frequency of the received signal from the nth propagation path is given by,

$$f_{DS} = f_t^{(n)} \cos \alpha_t + f_r^{(n)} \cos \alpha_r \qquad\qquad Eq\ (1.1)$$

where $f_t^{(n)} = v_t/\lambda$ and $f_r^{(n)} = v_r/\lambda$ are the maximum Doppler frequencies due to the motion of transmitting and receiving mobile stations, respectively. Obviously, as this Doppler shift is more as compared to that in the cellular radio communication, it will result in a faster fading channel with more rapid fluctuations in the signal power. In M2M communication channels, the autocorrelation is the product of the two bessel functions in contrast to the single bessel function that appears in the isotropic scattering model of a cellular communication environment [12]. The autocorrelation function for M2M communication environment is thus given by,

$$R(\tau) = J_o(2\pi f_t \tau) J_o(2\pi f_r \tau) \qquad\qquad Eq\ (1.2)$$

where f_t and f_r are the maximum Doppler frequencies due to the motion of transmitting and receiving mobile stations. If the transmitting MS is fixed then it will become BS like that in F2M cellular environment and the correlation function reduces to,

$$R(\tau) = J_o(2\pi f_r \tau) \qquad\qquad Eq\ (1.3)$$

Furthermore, the Doppler spectrum of F2M cellular communication channels for 2D isotropic scattering environment is given by Clarke [13] as,

$$S(f) = \begin{cases} \dfrac{\Omega_p}{2\pi f_m \sqrt{1-(f/f_m)^2}} & ;\quad |f| \leq f_m \\[3mm] 0 & ;\quad \text{otherwise,} \end{cases} \qquad Eq\ (1.4)$$

3

The above equation of the Doppler spectrum is modified to include a line-of-sight (LoS) component by Aulin [14] and is given by,

$$S(f) = \begin{cases} \dfrac{\Omega_p}{2\pi f_m(K+1)\sqrt{1-(f/f_m)^2}} \\ \qquad\qquad + \dfrac{K\Omega_p}{2(K+1)}\delta(f - f_m\cos\theta_o) & ; \quad 0 \le |f| \le f_m \qquad Eq\ (1.5) \\ \\ 0 & ; \quad \text{otherwise,} \end{cases}$$

where K is the ratio of the received LoS component to the scattered power. Doppler spectrum in Eq(1.5) has the same U-shape as that of Eq(1.4) as shown in Fig. 1.3,
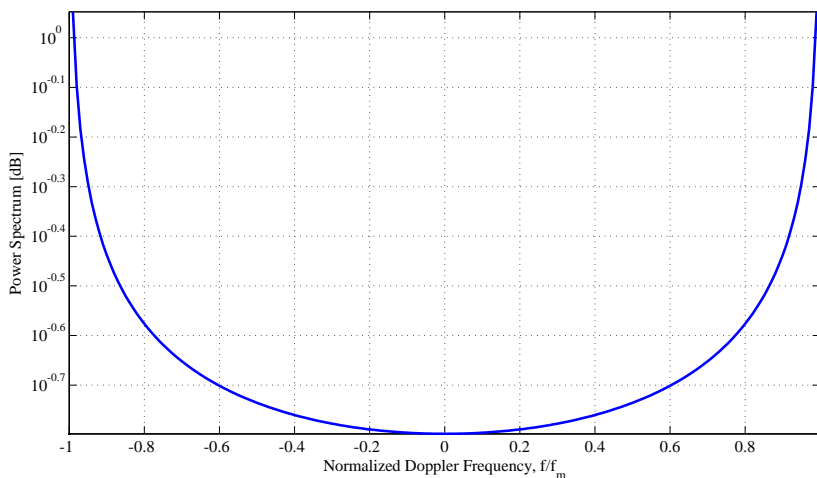
FIGURE 1.3: Normalized Doppler spectrum in F2M communication systems

Doppler spectrum in M2M communication environment can also be obtained by taking Fourier transform of $R(\tau)$ given in Eq(1.2) and can be expressed as,

$$S(f) = \frac{1}{\pi^2 f_t\sqrt{a}}\kappa\left(\frac{1+a}{2\sqrt{a}}\sqrt{1 - \left(\frac{f}{(1+a)f_t}\right)^2}\right) \qquad Eq\ (1.6)$$

where a is the ratio of maximum Doppler frequencies of the receiver to the transmitter (i.e. $a = f_R^{(n)}/f_T^{(n)}$) and $\kappa(\cdot)$ is the complete elliptic integral. Doppler spectrum for M2M and F2M communication channel is shown in Fig. 1.4,

4
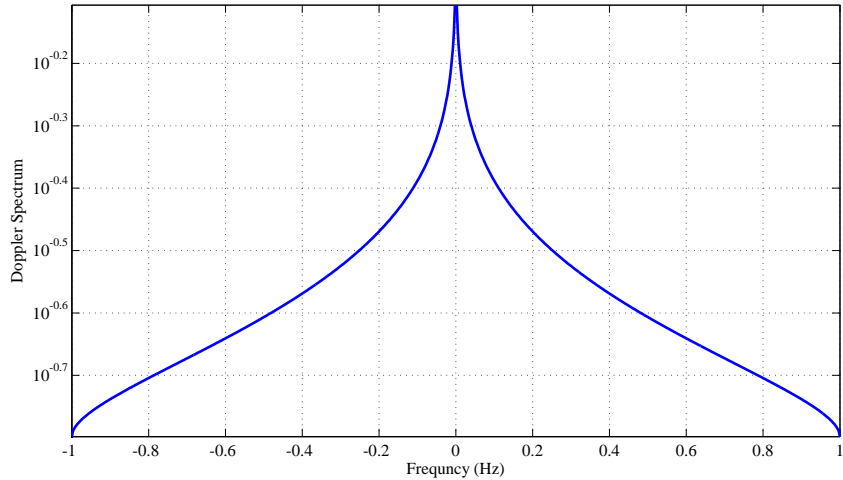
FIGURE 1.4: Doppler spectrum for M2M and F2M channels

Some higher order statistics like level crossing rate (LCR) and average fade duration (AFD) also depend on the scattering environment and speed of the mobile stations. LCR is defined as how often the envelope of the signal crosses a certain level and AFD is defined as how long the envelope of the signal remains below a certain level [15]. As scattering phenomena and speed of the MSs in M2M communication environment are different from those in F2M communication environment, their statistical parameters will also be different.

1.2 Brief Literature Review

Geometrical propagation channel modeling has a pivotal role in most of the emerging wireless communication systems like WSN, MANET, VANET, ITS and cooperative networks etc. As the propagation of radio signal through wireless communication channels is a complicated phenomenon, it is therefore necessary to characterize it by various effects like scattering environment, reflection from shiny surfaces, diffraction, multipath and shadowing [16]. These factors, in contrast to F2M communication environment, affect the signal propagation more severely in M2M communication environment. This is due to the presence of large number of scattering objects that reside around both mobile stations. Researchers have made efforts to model these effects either by their physical description or by their

probabilistic trend. Geometrically based spatial scattering modeling is one such popular methodology used so far in M2M and F2M communication environments. In F2M communication environment, initially, some simple geometrical channel models have been presented to model the physical environment. The hierarchy of the notable channel models proposed for F2M communication environment is from 2D [17–24] to 3D [25–27] channel models. Some of these models have been extended for M2M communication environment.

In contrast with conventional cellular systems, which have BS antenna heights above or at rooftop levels, the antenna heights of the communicating nodes in an M2M link are typically much lower than the surrounding scatterers such as buildings and trees. This difference in propagation environments has led to numerous investigations in the form of various spatial channel models for M2M communication environment categorically from SISO to MIMO [11, 28–33], one ring to two and three ring scattering models [29, 31, 33–36], and 2D to 3D scattering models [1, 2, 6, 30, 34, 36–41].

In [11], a mobile-to-mobile channel model, applicable to SISO case, is proposed. The closed-form expressions (i.e. analytically representation in relation to finite number of parameters and functions) for the spatio-temporal characteristics of the M2M channel are derived. In [28], time autocorrelation function and Doppler spectrum are derived assuming wide-sense stationary channel in 3D multipath scattering environment. The work originally carried out by Akki and Haber [11] on M2M SISO model was extended in [29] by Pätzold *et al.,* proposing a two-ring M2M MIMO model. The authors showed that 3D function can be expressed as a product of 2D space-time correlation functions. In [36], correlated double-ring scattering model is proposed where the authors have developed a sum-of-sinusoid model for M2M Ricean fading channel by taking LoS into account between the mobile stations. The authors have also derived relations for level crossing rate and average fade duration. A MIMO mobile-to-mobile Rayleigh fading channel is proposed in [30]. Closed-form expression for joint space-time correlation function

and power density spectrum are derived assuming a 2D isotropic scattering environment. A geometrical two-erose-ring model for MIMO mobile-to-mobile communication channels is presented in [31]. The authors assumed that the scatterers are only present not at the boundaries of the circles, rather at various distances from the center of the circles within circular region. They derived the channel diffused components of the link from transmit antenna elements to the receive antenna elements for the proposed model. Taking these diffused channel components, closed-form expressions for the correlation functions and power density spectrum are derived in [33]. Baltzis in [41] presented a 2D single-bounce elliptical model for spatial characteristics of mobile-to-mobile radio channels. They derived closed-form expressions for the probability density function (PDF) of Angle-of-Arrival (AoA) at the mobile stations by assuming uniform scatterers within adjustable hollow ellipses around the mobile stations. Time-of-Arrival (ToA) and AoA statistics are investigated in [1] by assuming uniform distribution of scatterers in circular regions around the mobile stations. In [38], a single-bounce geometrical channel model for mobile-to-mobile communications is considered and probability density functions for ToA and AoA are derived assuming uniform distribution of scatterers in an annular strip around each mobile station. A simplified scattering model for M2M is presented in [2], where scatterers are assumed to confine in elliptical regions. Using this model, closed-form expression for PDF of AoA and integral formula for cumulative distribution function (CDF) of ToA are derived.

In [37], a 3D M2M model is proposed for time-varying wideband multi-antenna channels. The authors assume that scatterers are located within cylinders around each MS. From this model, a closed-form joint space-time correlation function is derived with various other correlation functions shown to be its special cases. A 3D spherical model for M2M is introduced in [39]. The authors assume that each MS is located inside a scatterer-free sphere and that scatterers are only present outside the spheres. Using this model, the authors derive a 3D temporal correlation expression.

7

Although an adequate knowledge of the AoA statistics is important for robust design and operation of multi-antenna techniques such as beamforming, yet a handful knowledge of the ToA statistics is also essential for an efficient deployment of wideband communication systems. Statistical parameters such as the average delay and the delay spread have a direct impact on the error-rate performance of wideband communication links [42]. Hence, in order to assess the performance of real-world M2M communication systems, it is imperative to develop a physical understanding of the M2M propagation environment in terms of the AoA as well as ToA information of the multipath components of the wireless propagation channel. This purpose has been typically and adequately served by geometry-based spatial channel models for conventional cellular communications in which a fixed BS communicates with a mobile station (MS), see for example [17, 18, 43–45].

While 2D models are helpful in gaining insights into M2M communications, it is well-known that the low antenna heights of M2M communicating nodes cause signal reflections from nearby buildings and other scatterers, which are elevated above the communicating antennas. This physical phenomenon necessitates the inclusion of the elevation plane for an accurate description of M2M communication channels. Therefore, various 3D channel models have been proposed in the literature for a more precise spatial and temporal description of the M2M communication links relative to that provided by 2D channel models.

3D physical models are more realistic than 2D models in M2M communication environment because of low antenna elevations of the both ends of the communication link, compared to the high rise structures around them. Some notable 3D models in the literature are discussed here. A geometrical concentric-cylinders model for time-varying wideband MIMO M2M channel is introduced in [37]. The authors while considering a 3D scattering propagation environment, have showed that many correlation functions are the special cases of the their model. A 3D spherical SISO model for M2M is introduced in [39]. The authors assumed that mobile stations are located inside scatterer-free spheres and scatterers are only

present outside the spheres. Using the spherical model, the authors derived a 3D temporal correlation expression. A 3D spheroid model is presented in [26] for fixed-to-mobile communication environment. The authors provided closed-form expressions for PDFs of AoA for azimuth and elevation planes. In [27], a generalized 3D scattering model is proposed for macrocellular communication systems, where the authors derived closed-form expressions for joint and marginal PDFs of the AoA and ToA in the azimuth and elevation planes for a 3D spheroid model with a low Mobile Station (MS) antenna and an elevated Base Station (BS) antenna.

1.3   Research Aims and Problem Statement

The main aim of this research study is to develop a geometrically based 3D spatial scattering channel model for M2M communication environment. Although 3D spatial channel modeling is the most realistic way to model a low antenna-height M2M communication environment; however, it is more realizable if a flexible geometrical shape is considered in such a way that it can model this low-antenna height M2M link more practically and appropriately with respect to its surrounding high-rise scattering objects. The previous approaches to model the M2M channels in 3D scattering environment are not much realistic in their modeling of generalized scenarios because some models are better in one situation while the others in another. Out of the above-mentioned approaches, 3D cylindrical model [37] and 3D spherical model [39] are better techniques than existing 2D M2M models as far as the realistic M2M scattering environment is concerned; however, still these models are short of their appropriateness with realistic scatterer distribution around mobile stations in M2M communication environment. Since the scattering regions around the highways, streets and canyons in urban areas, where most of the times, communication between mobiles occurs, have their close resemblance with elliptical rather than cylindrical and spherical shapes. Hence besides the existing 3D cylindrical and spherical models used for modeling M2M scenarios, hemispheroid

approach used in [27] motivates us to utilize its further modified version the semi-ellipsoid approach in our research work to model the scattering regions in M2M environment, more realistically. Moreover, the 3D semi-ellipsoid channel model can be extended to a more generalized scatter-free semi-ellipsoid based 3D spatial channel model. Another objective of the proposed research work is to develop a comprehensive characterization of the M2M channel in form of spatio-temporal characteristics and Doppler spectrum that is helpful to grab its accurate and realistic knowledge for onward designing of more reliable and resource-efficient vehicular networks.

1.4 Methodology for the Targeted Research Aims

The proposed methodology for the targeted research study in the form of a flowchart is shown in Fig. 1.5. To achieve the targeted aims and solution to the prob-
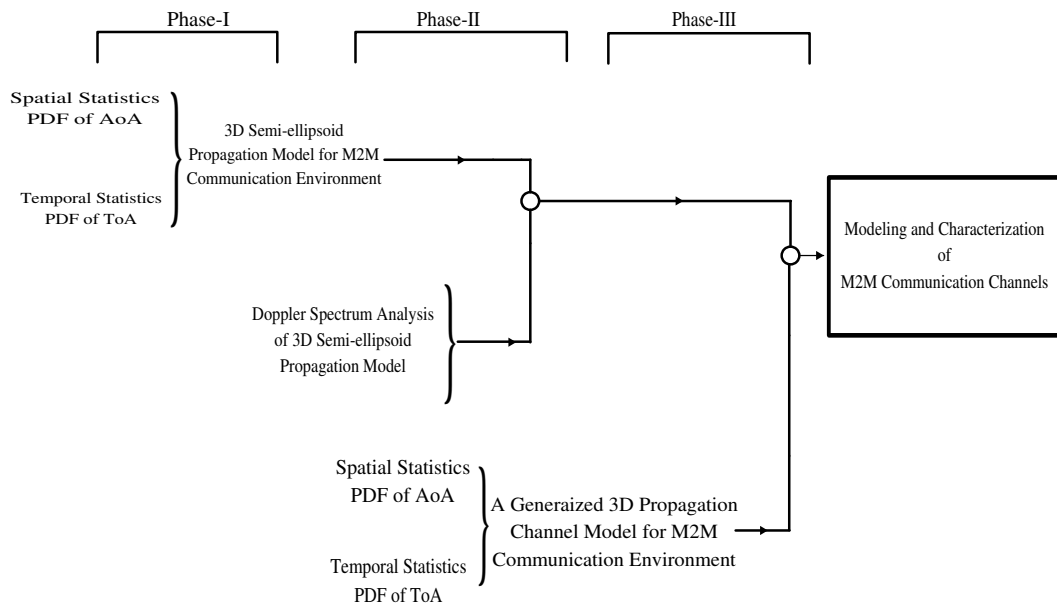
FIGURE 1.5: Methodology for the proposed targeted research work

lems mentioned in the previous section, we start with geometrically-based channel modeling. In phase-I of the research study, we develop a 3D semi-ellipsoid channel model for M2M communication environment. Using the developed model, we

derive analytical expressions for the joint and marginal PDFs of AoA and ToA .
These PDFs are then utilized for further characterization of the model for Doppler
spectrum analysis which is carried out in phase-II of the research study. Finally
in phase-III, we develop a generalized 3D spatial channel model for M2M com-
munication environment and derive analytical expressions for the PDFs of AoA
and ToA in azimuth and elevation planes. Combining the research work carried
in all the three phases, we reach our proposed research topic, the "Modeling and
characterization of mobile-to-mobile communication channels".

1.5   Research Contributions

The research contributions presented in this dissertation consists of the following
three major Phases:

1.5.1   Phase-1: 3D Semi-ellipsoidal Channel Model for Mobile-to-Mobile Radio Propagation Environment

The main contributions of this phase of the research study are as follows:

1. A 3D semi-ellipsoid propagation channel model for M2M communication en-
   vironment is developed by assuming uniform scatterer distribution around
   the mobile stations within the semi-ellipsoids. Using the 3D semi-ellipsoid
   channel model, expressions for the joint and marginal PDFs of AoA in az-
   imuth and elevation planes are derived.

2. The 3D semi-ellipsoid channel model is also analyzed for the temporal char-
   acteristics. Analytical expressions for the joint and marginal PDFs of ToA
   in azimuth and elevation planes are derived.

3. A comprehensive comparison is carried out with the existing geometrical
   propagation channel models in the literature.

1.5.2 Phase-II: Characterization of the 3D Propagation Channel for Doppler Spectrum

In this phase of the research study, the main contributions are:

1. A 3D semi-ellipsoid propagation channel model (developed in the first phase of research) is analyzed for Doppler spectrum

2. Analytical relationship between spatio-temporal characteristics of the model and Doppler spectrum is derived.

3. The impacts of mobile speeds and direction of arrival statistics on the Doppler power spectrum in M2M communication environment are analyzed.

1.5.3 A Generalized 3D Spatial Channel Model for Mobile-to-Mobile Communication Environment

In this last phase of the research study, the contributions are:

1. A geometrically based generalized 3D propagation channel model for M2M communication environment is developed.

2. Using the generalized propagation channel model, analytical expressions for the PDFs of AoA and ToA are derived by assuming uniform scatterer distribution within hollow semi-ellipsoids.

3. For validation, a comparison of the proposed model is carried with simulation results. The model is also validated by comparing it with the measurement data reported in the literature.

4. From the comparative analysis, it is concluded that some notable existing 2D and 3D spatial channel models for F2M and M2M communication environment in the literature can be deduced from our generalized model with an appropriate choice of a few parameters..

1.6 Research Publications

The research work contained in this dissertation consists of the following publications.

1.6.1 Journal Publications

[**J01**] **M. Riaz**, S. J. Nawaz, and Noor M. Khan, "3D Ellipsoidal model for M2M radio propagation environments," *Wireless Pers. Commun.*, vol. 72, no. 4, pp. 2465-2479, Oct. 2013. [ISI impact factor: 0.979]

[**J02**] **M. Riaz**, S. J. Nawaz, and Noor M. Khan, "A generalized 3D scattering channel model for spatio-temporal statistics in mobile-to-mobile communication environment," *IEEE Trans. Veh. Technol.*, vol. 64. no. 10, Oct. 2015, DOI=10.1109/TVT.2014.2371531. [ISI impact factor: 2.64]

[**J03**] S. J. Nawaz, **Muhammad Riaz**, and Noor M. Khan, "Temporal Analysis of a 3D Ellipsoid Channel Model for the Vehicle-to-Vehicle Communication Environments," *Wireless Pers. Commun.*, vol. 82, no. 3, pp. 1337-1350, June 2015. [ISI impact factor: 0.979]

[**J04**] **M. Riaz**, S. J. Nawaz, and Noor M. Khan, "Doppler Spectrum Analysis of a 3D Ellipsoid Channel Model for the Mobile-to-Mobile Communication Environment," Submitted in *"Frequenz - Journal of RF engineering and telecommunications"*. [ISI impact factor: 0.393]

1.6.2 Additional Contributions

During my PhD studies, I have also contributed to the following publications. However, these publications are not included in the thesis:

[**J05**] Muhammd Riaz, M. Saud Khan, and Noor M. Khan, "LoMoB: A New Scheme for Node Localization, Critical Node Detection and Redeployment in Sparsely Populated Wireless Sensor Networks," Submitted in PLOS-ONE 2014.

[**J06**] Kashif Nasr, Muhammd Riaz, Noor M. Khan, and Tanveer Afzal "Partition identification and redeployment algorithm for three dimensional environment (PIRATE) in wireless sensor networks," ready to be submitted in Feb. 2015.

[**J06**] Yaqoob Wani, Muhammd Riaz, and Noor M. Khan "Characterization of Elliptical Spatial Channel Model for MIMO Mobile-to-Mobile Communication Environment," to be submitted in IEEE Trans. Veh. Technol. in Feb. 2015.

[**C01**] Muhammad Riaz, and Noor M. Khan, "Closed-form expressions for correlation function and power density spectrum in MIMO mobile-to-mobile channels using two-erose-ring model", in Proc. of IEEE, Int. Conf. on Information and Commun. Technol., 2011, pp. 1-5.

1.7 Organization of Thesis

The rest of the dissertation is structured as follows:

In Chapter 2, geometrically based spatial channel models for M2M communication environment, along with description of their system models, are presented. Chapter 3 presents a 3D semi-ellipsoid scattering model for M2M communication environment, where it is assumed that mobile stations are located at the center of the semi-ellipsoids and scatterers are uniformly distributed around the mobile stations within the semi-ellipsoids. Derivation of closed-form expressions for the joint and marginal PDFs of ToA and AoA in azimuth and elevation planes are provided. In Chapter 5, a generalized 3D spatial channel model for M2M communication environment is presented, where, we have assumed that mobile stations are located within scatterer-free semi-ellipsoids. The generalized model is characterized for spatial and temporal statistics. In Chapter 4, we analyzed the 3D semi-ellipsoid channel for Doppler spectrum by taking motion of the mobile stations. Finally, conclusions of the dissertation is provided in Chapter 6.

Chapter 2

GEOMETRIC CHANNEL MODELS FOR M2M COMMUNICATION ENVIRONMENT

In this chapter, we describe a detailed overview of the spatial channel models published in the literature for M2M communication environment. Section 2.1 and 2.2 describe the 2D circular and elliptical spatial channel models, respectively. 3D cylindrical and spherical channel models for M2M communication environment are discussed in Section 2.3 and 2.4.

2.1   Circular Models

In this section, we describe some geometrically-based two-circular spatial scattering models for M2M communication environment.

2.1.1   2D Circular Disc Scattering Model

A 2D circular disc scattering model, developed in [1], is presented here, where the authors assumed that scatterers are uniformly distributed in circular regions around the MSs located at the centers of the circles as shown in Fig. 2.1.
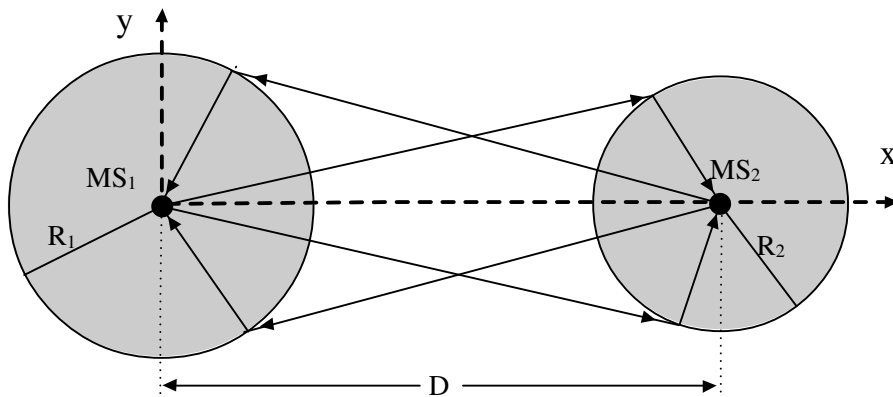
FIGURE 2.1: Circular disc scattering model for M2M communication environment.

15
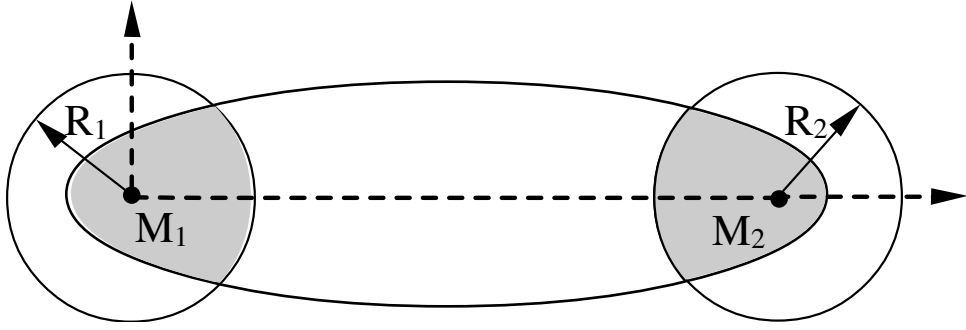
FIGURE 2.2: Scatterers contributing towards PDF of ToA in circular disc scattering model.

The model description is as follows: Mobile stations MS_1 and MS_2 are surrounded by uniformly distributed scatterers in circular regions of radii R_1 and R_2, respectively. By exploiting the developed model by the authors, expressions for the PDF of AoA and ToA are derived.

For the formulation of ToA statistics, the authors consider that for a particular delay of arriving a certain signal, an imaginary ellipse is drawn around the contributing scatterers as shown in Fig. 2.2, such that the mobile stations reside at the foci of the imaginary ellipse.

Probability distributions of the scatterers for ToA at the particular time of arrival of the signal is formulated, the derived expression for the PDF of ToA is given by,

$$f_\tau(\tau) = \frac{c}{\pi R^2} \left[\frac{\pi \tau^2 c^2 k_2 - \tau c k_2^2 + \pi k_2 k_1^2 + \tau c k_1^2 - 2R k_1^2}{4 k_1 k_2} + \frac{\tau^2 c^2 k_o k_4 + \tau c k_o k_1^2}{2 k_4^2 + 2 k_o^2 k_1^2} \right.$$
$$+ \frac{\tau^2 c^2 + k_1^2}{2 k_1} . \arctan\left(\frac{k_o k_1}{k_4} \right) - \frac{R - \tau c}{(4R^2 D^2 - k_3)^{(1/2)}}$$
$$\left. \times \left(2R^2 + \frac{\tau c k_1^2 k_4 (1 + k_o^2)}{(2 k_4^2 + 2 k_o^2 k_1^2)^{(1/2)}} \right) \right]$$

Eq (2.1)

where c is the speed of light, R is the radius of circle around the MS and D is the distance between MSs, the remaining parameters are defined as follows:

16
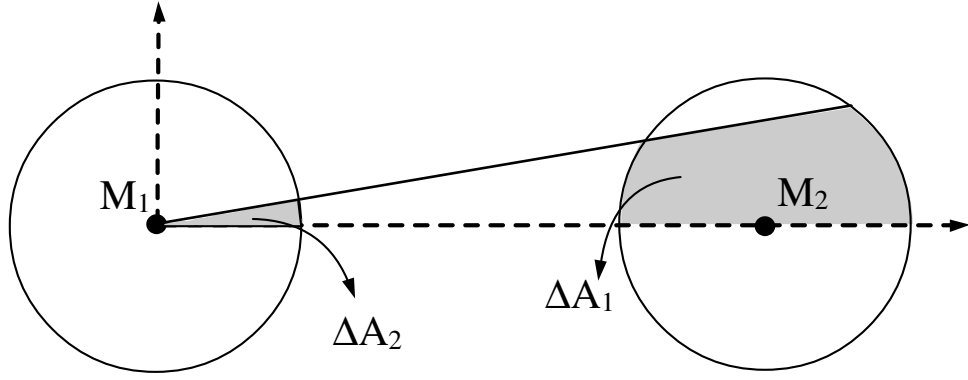
FIGURE 2.3: Scatterers contributing towards PDF of AoA in circular disc scattering model.

$$k_o = \tan\left(\frac{1}{2}\arccos\left(\frac{-\tau^2 c^2 + D^2 + 2R\tau c}{2RD}\right)\right)$$

$$k_1 = \sqrt{\tau^2 c^2 - D^2}$$

$$k_2 = \sqrt{D^2 - 4R^2 - \tau^2 c^2 + 4R\tau c}$$

$$k_3 = -\tau^2 c^2 + D^2 + 2R\tau c$$

$$k_4 = D - \tau c$$

The PDF of AoA derivation is based on the scatterers distribution as shown in Fig. 2.3. and an expression for the PDF of AoA is given as,

$$f_\theta(\theta) = \begin{cases} \dfrac{\rho}{2\pi(1+\rho)} & \\[2mm] \quad + \dfrac{2D\cos\theta\sqrt{D^2\cos^2(\theta) - D^2 + R_2^2}}{\pi R_2^2(1+\rho)} & \\[2mm] \qquad ; -\arcsin(R_2/D) \le \theta \le \arcsin(R_2/D) & \\[2mm] 0 \quad ; \text{elsewhere} & \end{cases} \qquad Eq\ (2.2)$$

2.1.2 Circular Model Employing Annular Strip

In this section, an overview of the 2D circular model employing dual annular strip [38] is presented. The authors assumed that scatterers are uniformly distributed
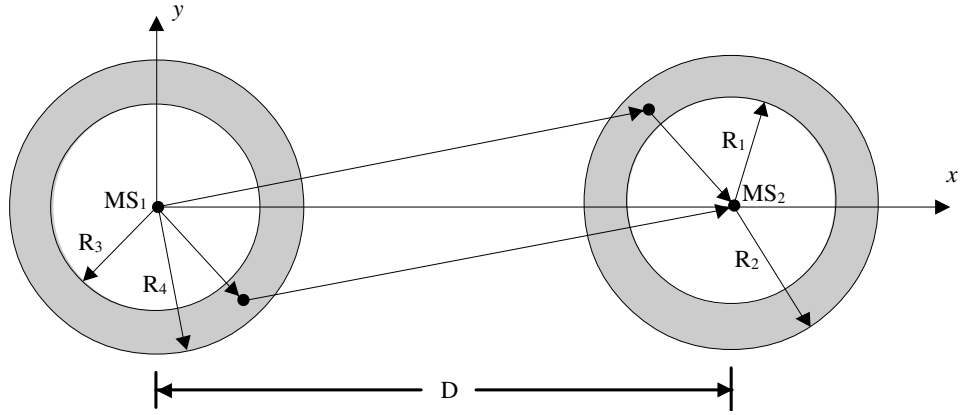
FIGURE 2.4: Circular Model employing dual annular strip for M2M communi-
cation environment.
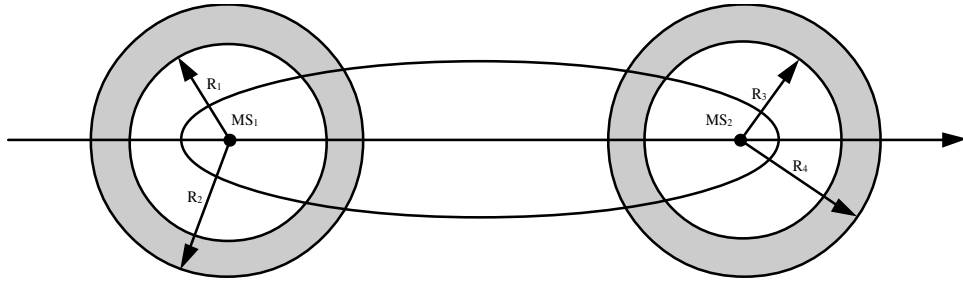
FIGURE 2.5: Scattering objects contributing towards the PDF of ToA in circular
model employing dual annular strip for M2M communication environment.

around the MSs in the annular strips (i.e., shaded regions) as shown in Fig. 2.4.

The outer and inner circles have common center and distance between their center
is represented by D, which is much larger than the radii of the circles. The radius
of any of the circle is represented by $R_{m,q}$, where, the index m is used to represent
MS_1 and MS_2 and the index q is used to represent inner and outer circles. The
number of scatterers around the transmitting and receiving MSs are denoted by
N_1 and N_2, respectively. The authors obtained the PDF of ToA by differentiating
the derived CDF of ToA for a constant delay using the proposed model as shown
in Fig. 2.5.

The PDF of ToA is given as,
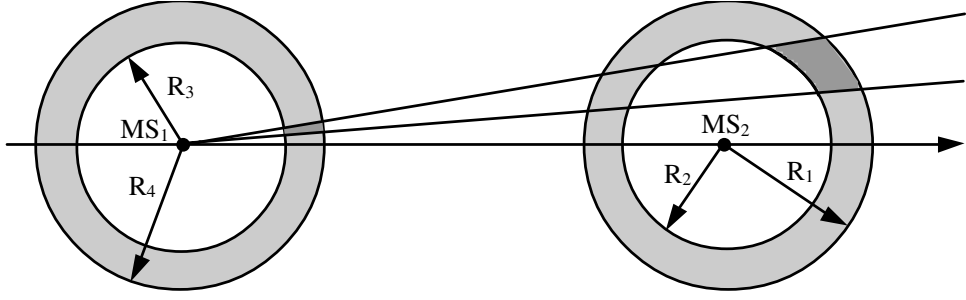
FIGURE 2.6: Scattering objects contributing towards the PDF of AoA in circular model employing dual annular strip for M2M communication environment.

$$f_\tau(\tau) = \frac{c}{\pi R^2} \left[\frac{\pi\tau^2c^2k_2 - \tau ck_2^2 + \pi k_2 k_1^2 + \tau ck_1^2 - 2Rk_1^2}{4k_1 k_2} + \frac{\tau^2 c^2 k_o k_4 + \tau c k_o k_1^2}{2k_4^2 + 2k_o^2 k_1^2} \right.$$

$$+ \frac{\tau^2 c^2 + k_1^2}{2k_1} . arctan(\frac{k_o k_1}{k_4}) - \frac{R - \tau c}{(4R^2 D^2 - k_3)^{(1/2)}}$$

$$\left. \times \left(2R^2 + \frac{\tau c k_1^2 k_4 (1 + k_o^2)}{(2k_4^2 + 2k_o^2 k_1^2)^{(1/2)}} \right) \right]$$

$$Eq\ (2.3)$$

where c is the speed of light, R is the radius of circle around the MS and D is the distance between MSs, the remaining parameters are defined as follows:

$k_o = \tan\left(\frac{1}{2} arccos\left(\frac{-\tau^2 c^2 + D^2 + 2R\tau c}{2RD} \right) \right)$

$k_1 = \sqrt{\tau^2 c^2 - D^2}$

$k_2 = \sqrt{D^2 - 4R^2 - \tau^2 c^2 + 4R\tau c}$

$k_3 = -\tau^2 c^2 + D^2 + 2R\tau c$

$k_4 = D - \tau c$

For the determination of an analytical expression for the PDF of AoA, the contributing scatterers are assumed to be confined in the shaded region as shown in Fig. 2.6. The derived expression for the PDF of AoA is given as follows

$$f_\theta(\theta) = \begin{cases} \dfrac{0.5(R_4^2 - R_3^2)}{\pi(R_4^2 + R_2^2 - R_3^2 - R_1^2)} & ; \alpha_2 \leq \theta \leq \pi \\[3mm] \dfrac{2D\cos\theta\sqrt{R_2^2 - D^2\sin^2\theta} + 0.5(R_4^2 - R_3^2)}{\pi(R_4^2 + R_2^2 - R_3^2 - R_1^2)} & ; \alpha_1 \leq \theta \leq \alpha_2 \\[3mm] \dfrac{2D\cos\theta\left(\sqrt{R_2^2 - D^2\sin^2\theta} - \sqrt{R_1^2 - D^2\sin^2\theta}\right)}{\pi(R_4^2 + R_2^2 - R_3^2 - R_1^2)} \\ \quad + \frac{0.5(R_4^2 - R_3^2)}{\pi(R_4^2 + R_2^2 - R_3^2 - R_1^2)} & ; -\alpha_1 \leq \theta \leq \alpha_1 \\[3mm] \dfrac{2D\cos\theta\sqrt{R_2^2 - D^2\sin^2\theta} + 0.5(R_4^2 - R_3^2)}{\pi(R_4^2 + R_2^2 - R_3^2 - R_1^2)} & ; -\alpha_2 \leq \theta \leq \alpha_1 \\[3mm] \dfrac{0.5(R_4^2 - R_3^2)}{\pi(R_4^2 + R_2^2 - R_3^2 - R_1^2)} & ; -\alpha_2 \leq \theta \leq \alpha_1 \end{cases}$$

$$Eq\ (2.4)$$

2.2 Elliptical Shape Based Models

In this section, some elliptical shape based channel models are described. Since elliptical geometry can model streets and canyons more accurately than the circular shapes, elliptical spatial channel models are considered more suitable for modeling M2M communication channels than the circular ones.

2.2.1 Simplified Elliptical Model

The simplified 2D elliptical channel model is proposed in [2] for M2M communication environment. The authors assumed that uniform scatterers are distributed in the elliptical regions around both mobile stations as shown in Fig. 2.7. According to the authors, ellipses of arbitrary sizes and orientations can model these scattering regions. Each MS is equipped with low elevated antennas and separated by a distance D from the other MS as shown in Fig. 2.7. The mobile stations M_1 and M_2 are located in the cartesian coordinate system at points (0,0) and (D,0). The major and minor axes of the ellipses are a_i (for $i = 1$ or 2) and b_i. The major axes of the ellipses around both the mobile stations making angles ϕ_{t1} and ϕ_{t2}
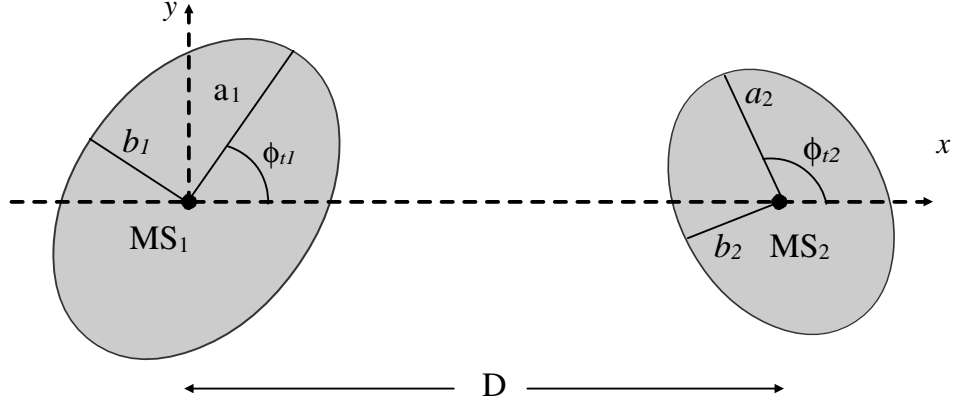
FIGURE 2.7: Simplified elliptical model for M2M communication environment.

with x-axis while ϕ is a running angle of multipath signal with any scatter with respect to the positive x-axis. Using their proposed model, the authors derived expressions for the PDF of AoA and ToA of the multipath signals.

$$f_\phi(\phi) = \frac{\rho_1^2(\phi) + \sigma[(\rho_2^+(\phi))^2 - (\rho_2^-(\phi))^2]}{2\pi(a_1 b_1 + \sigma a_2 b_2)} \qquad Eq~(2.5)$$

$$F_\phi(\phi) = \frac{\int\limits_{-\pi}^{\phi_1^-} R_1(\phi)\mathrm{d}\phi + \int\limits_{\phi_1^+}^{\pi} R_1(\phi)\mathrm{d}\phi + \sigma \int\limits_{\phi_2^-}^{\phi_2^+} R_2(\phi)\mathrm{d}\phi}{2\pi(a_1 b_1 + \sigma a_2 b_2)} \qquad Eq~(2.6)$$

where,

$$R_{1(2)} = \left([\min(\rho_{0,\tau}(\phi), \rho_{1(2),\tau}^+(\phi))]^2 - [\rho_{1(2),\tau}^-(\phi)]^2\right) \times u(\rho_{0,\tau}(\phi) - \rho_{1(2),\tau}^-(\phi)) \quad Eq~(2.7)$$

The above discussed simplified elliptical spatial channel model for M2M communication environment is somewhat better than 2D circular spatial channel models because of the elliptical geometrical shapes that can model the M2M channels more realistically than the circular shapes used traditionally in the previous literature. The model provides flexibility in the sense that the model is rotatable and has adjustable major and minor axes.
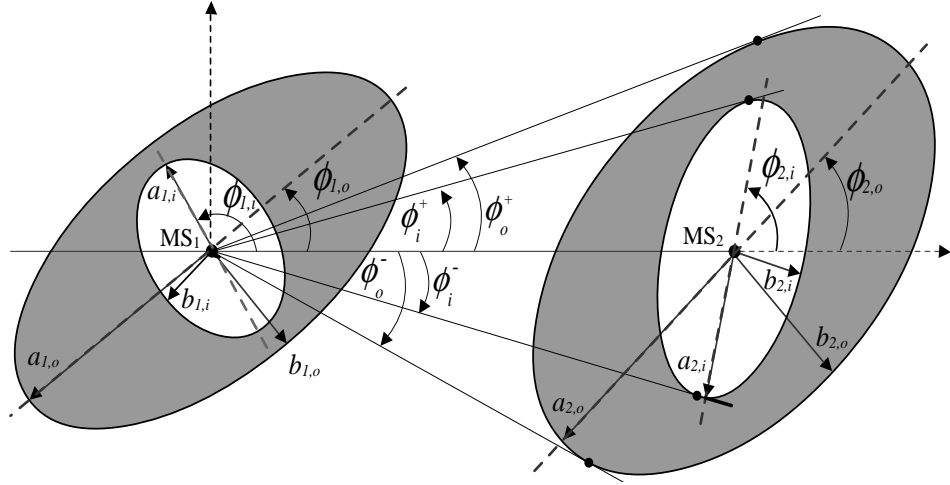
FIGURE 2.8: Generalized elliptical model for M2M communication environment.

2.2.2 A 2D Generalized Elliptical Model

A more appropriate and generalized geometrical channel model in comparison to circular and elliptical models for M2M communication environment is proposed in [41]. The authors consider scatterer-free rotatable elliptical region around each MS within another elliptical geometrical shape and fill the space between these two regions with uniformly distributed scatterers as shown in Fig. 2.8.

The authors have derived closed-form expression for the PDF of AoA of the multipaths at the receiving MS for their proposed generalized model assuming single-bounce propagation. The expression for the PDF of AoA derived by the authors at each receiving MS is given as,

$$
f(\phi) = \begin{cases}
\frac{\rho_{o,1}^2 - \rho_{i,1}^2 + \sigma(\rho_{o,2}^{+}{}^2 + \rho_{i,2}^{-}{}^2 - \rho_{o,2}^{-}{}^2 - \rho_{i,2}^{+}{}^2)}{2\pi[a_{o,1}b_{o,1} - a_{i,1}b_{i,1} + \sigma(a_{o,2}b_{o,2} - a_{i,2}b_{i,2})]} & ; \phi\epsilon[\phi_i^-, \phi_i^+] \\[3mm]
\frac{\rho_{o,1}^2 - \rho_{i,1}^2 + \sigma(\rho_{o,2}^{+}{}^2 - \rho_{o,2}^{-}{}^2)}{2\pi[a_{o,1}b_{o,1} - a_{i,1}b_{i,1} + \sigma(a_{o,2}b_{o,2} - a_{i,2}b_{i,2})]} & ; \phi\epsilon[\phi_o^-, \phi_i^-] \cup [\phi_i^+, \phi_o^+] \qquad Eq\ (2.8) \\[3mm]
\frac{\rho_{o,1}^2 - \rho_{i,1}^2}{2\pi[a_{o,1}b_{o,1} - a_{i,1}b_{i,1} + \sigma(a_{o,2}b_{o,2} - a_{i,2}b_{i,2})]} & ; \phi\epsilon[-\pi, \phi_o^-] \cup [\phi_o^+, \pi]
\end{cases}
$$

The generalized elliptical spatial channel model adds another degree of flexibility to the previous simplified elliptical spatial channel model with the introduction of scatterer-free elliptical region. The authors considered their model as a generalized one because some previous 2D geometrical spatial channel models like circular and elliptical channel models for M2M communication environment can be deduced from their generalized geometrical channel model.

This generalized spatial channel model is much better than some of the previous channel models; however, there are some limitations, i.e., the authors ignore the arrival of the signals from the surrounding elevated scatterers like high-rise buildings, trees etc.

It is a fact that due to the low antenna heights of the communicating mobiles a 2D channel model that ignores the height of the scatterers can not model their propagation rather a 3D model that takes the elevation plane into account fulfills the task.

2.3   Cylindrical Model

Addressing the issues of elevated scatterers in M2M communication environment, a double bounce 3D cylindrical scattering model for MIMO-M2M communication links is proposed in [37] as shown in Fig. 2.9. Here the authors took multipath signals in elevation plane into account by rejecting the signals traveling only in azimuth plane which is a rare case. According to the authors, MSs in M2M communication environment are usually surrounded by local high-rise structures in the urban area; therefore, 2D spatial channel models are not suitable to model the urban environment appropriately. To accommodate these high-rise scatterers, authors use a 3D cylindrical shape filled with uniform scatterers. Mobile stations are placed at the centers of the cylinders and are equipped with multiple antennas of height h_t and h_r at the transmitter and receiver, respectively. Using their
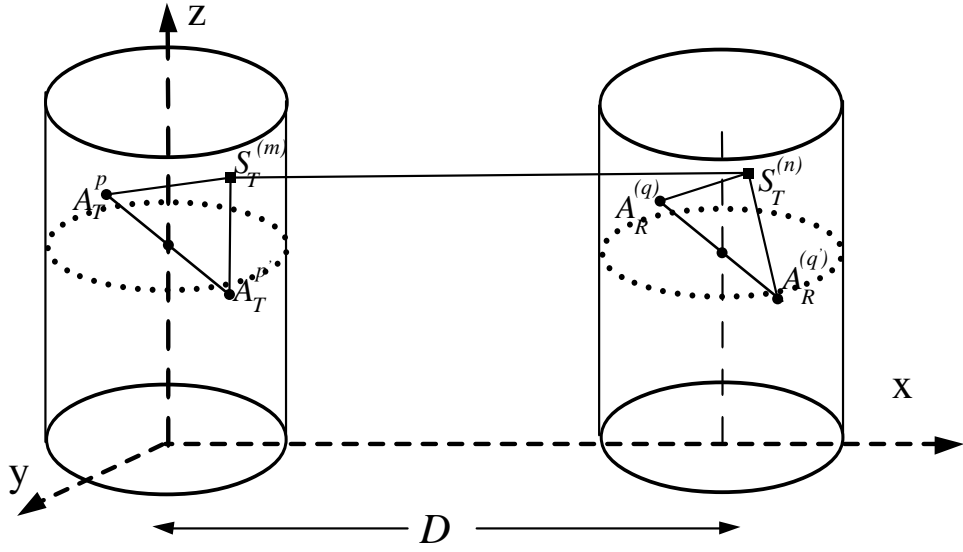
FIGURE 2.9: Cylindrical scattering model for M2M communication environment.

proposed model, the authors derived closed-form expressions for the joint space-time correlation function of the multipath signals in 3D propagation environment. Moreover, outage capacity of the MIMO system is analyzed for various antenna spacings.

The cylindrical geometrical shape provides a better approach to model the multipath signals in elevation plane for M2M communication scenario. However, observing the physical geometry of the scattering objects i.e., vehicles and pedestrians in addition to the high-rise buildings in the streets and canyons in urban areas, cylindrical shape is not appropriate.

2.4 Spherical Model

A 3D spherical spatial channel model for M2M communication environment is proposed in [39], where, the authors assumed that MSs are located inside scatter-free spheres and scatterers are uniformly distributed on the surface of the spheres.

Using the spherical model, expression for the temporal correlation function of a 3D M2M communication channels is derived.

The 3D spatial channel models for M2M communication environment as discussed in the previous sections (i.e., Section 2.3, 2.4) are better than 2D circular and elliptical spatial channel models (Section 2.1, 2.2). However, these 3D spatial channel models have also shortcomings i.e., these spatial channel models can not model the scatterers in elevation plane as the scatterer distribution in the streets and canyons. To model the scatterers in M2M communication environment in regions like streets and canyons, some more realistic spatial channel models are proposed in this dissertation and explained in detail in the forthcoming chapters.

Chapter 3

A 3D SEMI-ELLIPSOID CHANNEL MODEL FOR M2M COMMUNICATION ENVIRONMENT

In this chapter, a geometrically based 3D semi-ellipsoid channel model for M2M communication environment is presented. In section 3.1, a system model of the proposed spatial channel model is presented. A detailed mathematical derivation of the PDF of AoA and ToA, based on the proposed geometrical channel model, is provided in Section 3.2 and 3.5. Results and their discussion about the spatial and temporal statistics of the proposed M2M spatial channel model are presented in Section 3.3.

3.1 System Model of 3D Ellipsoidal Channel Model

The geometry of the proposed 3D semi-ellipsoid scattering model for M2M communication channels is depicted in Fig. 3.1. The scatterers around both the MSs are assumed to be confined within semi-ellipsoids centered at MSs. Both mobile stations are equipped with omnidirectional antennas residing at an equal height (low height antennas). The distance between both MS_i (i=1, 2 for MS_1 and MS_2 respectively) is d. The semi-ellipsoids surrounding the MSs can independently be rotated around their z-axes with a certain angle θ_{m_i} with respect to the LoS component. Some common assumptions [26, 27, 41, 46] that are used to design the proposed model are listed as follows,

1. Each mobile station is surrounded by uniformly distributed scatterers confined within a semi-ellipsoid.

2. The power incident on a certain scattering object is reflected with an equal distribution of power in all directions.

26
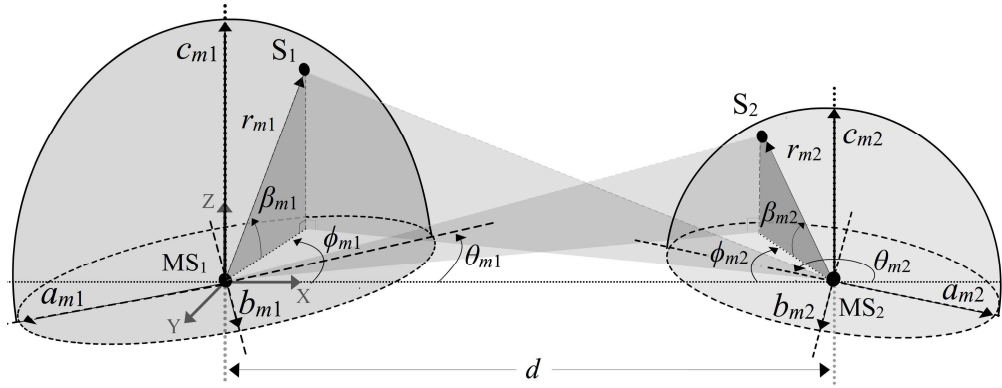
FIGURE 3.1: Proposed 3D semi-ellipsoidal channel model for mobile-to-mobile communication environment

3. The signals received at a MS are assumed to arrive with an equal strength from all directions in horizontal and vertical planes.

4. The communication between the MSs is assumed to take place via single isotropic scattering object.

5. All the scatterers have uniform random phases and equal scattering coefficients.

Consider that the mobile stations MS_1 and MS_2 are located at points $(0, 0, 0)$ and $(d, 0, 0)$ respectively, in the Cartesian coordinates system. Semi-major and semi-minor axes of any of the semi-ellipsoids are denoted by a_{mi} and b_{mi} while its maximum height is represented by c_{mi}. These dimensions of both the semi-ellipsoids can independently be set in all the directions. The dimensions of semi-ellipsoid around $MS_i (i = 1, 2)$ along with its x, y, and z-axes are denoted by a_{mi}, b_{mi}, and c_{mi}, respectively. The angles of the arriving multipath waves in azimuth and elevation planes are shown by ϕ_{mi} and β_{mi}, respectively. The distance of a certain scatterer from MS_i is denoted by r_{mi}.

The semi-ellipsoid centered at a certain point (X_{oi}, Y_{oi}, Z_{oi}) in cartesian coordinates system, can be expressed as [47],

$$\frac{\left((x_{mi} - X_{oi}) \cos \theta_{mi} + (y_{mi} - Y_{oi}) \sin \theta_{mi}\right)^2}{a_{mi}^2}$$

$$+ \frac{\left(-(x_{mi} - X_{oi}) \sin \theta_{mi} + (y_{mi} - Y_{oi}) \cos \theta_{mi}\right)^2}{b_{mi}^2}$$

$$+ \frac{\left(z_{mi} - Z_{oi}\right)^2}{c_{mi}^2} = 1$$

$$Eq\ (3.1)$$

Relations for the transformations between cartesian and spherical coordinates systems are [47],

$$x_{m1} = r_{m1} \cos \phi_{m_1} \cos \beta_{m_1},\ y_{m1} = r_{m1} \cos \beta_{m_1} \sin \phi_{m_1},\ \text{and}\ z_{m1} = r_{m1} \sin \beta_{m_1}$$

$$x_{m2} = x_{m1} + d,\ y_{m2} = y_{m1},\ \text{and}\ z_{m2} = z_{m1}$$

Volume V of all the scattering regions can be obtained by adding the volumes of both the semi-ellipsoids, which can be written in simplified form as,

$$V = \frac{2}{3}\pi \left(a_{m1}b_{m1}c_{m1} + a_{m2}b_{m2}c_{m2}\right) \qquad Eq\ (3.2)$$

The scattering region contributing towards the arrival of signals at MS_2 is divided into two partitions, viz: P_1 and P_2, as shown in Fig. 3.2. The partition P_1 consists of those directions in which the scatterers of only one semi-ellipsoid (around MS_1) contribute towards the arrival of signals; whereas, the P_2 consists of those directions in which both the semi-ellipsoids contribute in the arrival of signals at receiver. The azimuth threshold angles, $\phi_{t1,m1}$ and $\phi_{t2,m1}$, shown in Fig. 3.2, are defined to separate different partitions of the scattering region. These azimuth threshold angles can be obtained in the simplified form as,
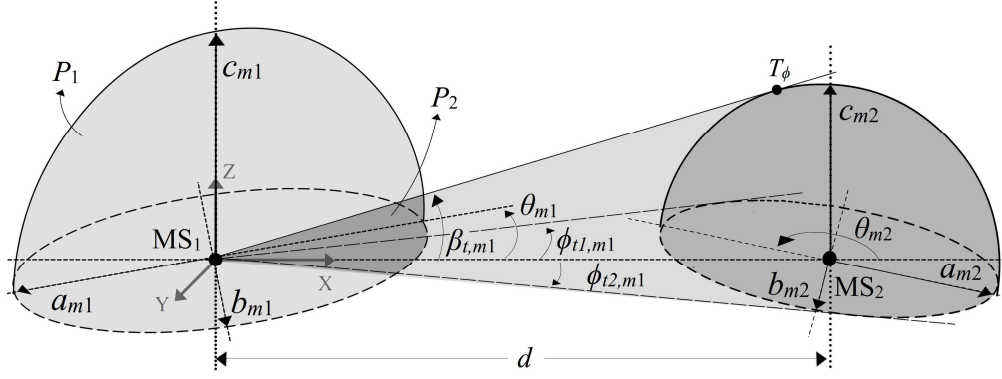
FIGURE 3.2: Scattering regions in the proposed model when observing angle-of-arrival at MS_1

$$
\left.\begin{array}{c} \phi_{t1,m1}^{+} \\[2ex] \phi_{t2,m1}^{-} \end{array}\right\} = \begin{cases} \arctan\left\{ \dfrac{1}{c_{m2}^2 d^2 - \Omega\left(a_{m2}^2 \cos^2\theta_{m2} + b_{m2}^2 \sin^2\theta_{m2}\right)} \right. \\[3ex] \qquad \times \Big\{ \Omega(a_{m2}^2 - b_{m2}^2)\cos\theta_{m2}\sin\theta_{m2} \pm \Big(b_{m2}^2 c_{m2}^2 d^2 \Omega \cos^2\theta_{m2} \\[3ex] \qquad\qquad \left. + a_{m2}^2 d^2 c_{m2}^2 \Omega \sin^2\theta_{m2} - a_{m2}^2 b_{m2}^2 \Omega^2 \Big)^{1/2} \Big\} \right\} \\[3ex] \qquad\qquad ;\ \beta_{m1} < \arctan\left(\dfrac{c_{m2}}{d}\right) \\[3ex] 0 \qquad\qquad ;\ \text{otherwise} \end{cases}
$$

$$Eq\ (3.3)$$

where $\Omega = c_{m2}^2 - d^2 \tan^2\beta_{m1}$. Similarly, the elevation threshold angle, $\beta_{t,m1}$, shown in Fig. 3.2, is computed to separate among the above mentioned two partitions in elevation plane. This threshold angle is computed as a function of azimuth AoA. $\beta_{t,m1}$ is the angle between the ground azimuth plane and the the line joining the MS_1 and the tangent point (i.e., T_ϕ) at the semi-ellipsoid around MS_2. After some algebraic manipulations, the simplified solution for elevation threshold angle $\beta_{t,m1}$

29
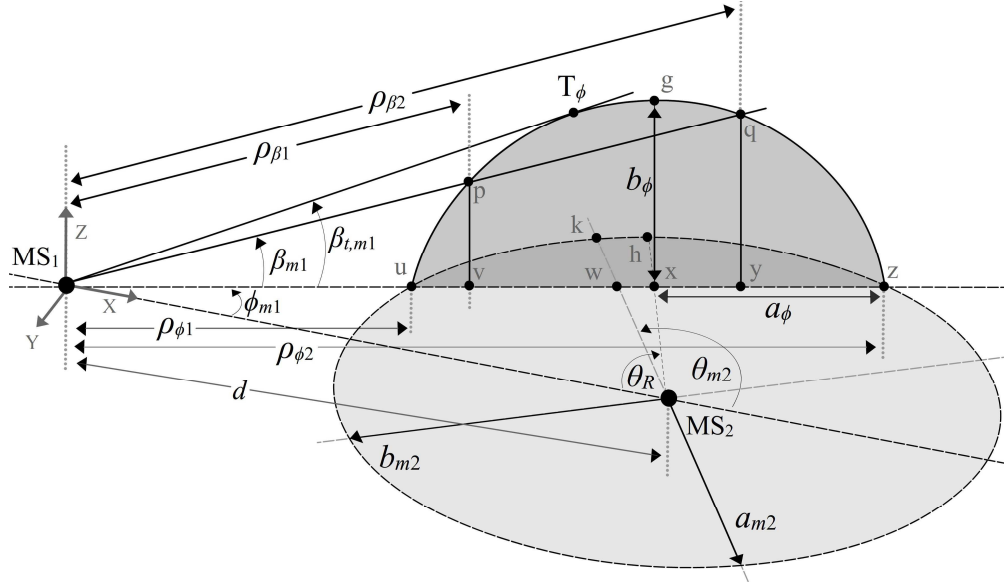
FIGURE 3.3: Cross-sectional view of the semi-ellipsoid scattering region around MS_2.

can be expressed as follows,

$$
\beta_{t,m1} = \begin{cases} \arctan\left(\dfrac{2b_\phi}{\sqrt{(\rho_{\phi1} + \rho_{\phi2})^2 - 4a_\phi^2}}\right) \\ \qquad ; \quad \phi_{t2,m1}\big|_{\beta_{m1}=0^o} \leq \phi_{m1} \leq \phi_{t1,m1}\big|_{\beta_{m1}=0^o} \\[2mm] 0 \qquad ; \quad \text{otherwise} \end{cases} \qquad Eq\ (3.4)
$$

where, a_ϕ and b_ϕ are the major and minor axes of the ellipse seen in vertical plane formed within the semi-ellipsoid around MS_2 for a certain azimuth angle ϕ_{m1} (see Fig. 3.3), which can be derived as,

$$
a_\phi = \frac{a_{m2}b_{m2}\sqrt{b_{m2}^2 \cos^2(\theta_{m2} - \phi_{m1}) + a_{m2}^2 \sin^2(\phi_{m1} - \theta_{m2}) - d^2 \sin^2 \phi_{m1}}}{b_{m2}^2 \cos^2(\theta_{m2} - \phi_{m1}) + a_{m2}^2 \sin^2(\theta_{m2} - \phi_{m1})}
$$

$$Eq\ (3.5)$$

$$b_\phi = \frac{1}{a_{m2}b_{m2}}\sqrt{a_{m2}^2 b_{m2}^2 c_{m2}^2 - b_{m2}^2 c_{m2}^2 \Gamma^2 \cos^2(\theta_{m2} + \theta_R) - a_{m2}^2 c_{m2}^2 \Gamma^2 \sin^2(\theta_{m2} + \theta_R)}$$

Eq (3.6)

where

$$\Gamma = \sqrt{d^2 + \frac{1}{4}\left(\rho_{\phi 1} + \rho_{\phi 2}\right)^2 - d\left(\rho_{\phi 1} + \rho_{\phi 2}\right)\cos\phi_{m1}}$$

and

$$\theta_R = \arcsin\left(\frac{(\rho_{\phi_1} + \rho_{\phi_2})\sin\phi_{m1}}{2\,\Gamma}\right)$$

A horizontal line from MS_1 intersects the elliptical base of the semi-ellipsoid around MS_2 at points u and z. The distances from MS_1 to points u and z are represented by $\rho_{\phi 1}$ and $\rho_{\phi 2}$, respectively. After doing tedious mathematical simplifications, these distances can thus be obtained as,

$$
\left.\begin{array}{c} \rho_{\phi 1}^+ \\[4pt] \rho_{\phi 2}^- \end{array}\right\} =
\begin{cases}
\dfrac{-1}{a_{m2}^2 \sin^2(\phi_{m1} - \theta_{m2}) + b_{m2}^2 \cos^2(\phi_{m1} - \theta_{m2})} \\[8pt]
\qquad \times \Bigg\{ d\Big(a_{m2}^2 \sin(\phi_{m1} - \theta_{m2})\sin\theta_{m2} - b_{m2}^2 \cos(\phi_{m1} - \theta_{m2})\cos\theta_{m2}\Big) \\[8pt]
\qquad\qquad \pm\, a_{m2}b_{m2}\Big(a_{m2}^2 \sin^2(\phi_{m1} - \theta_{m2}) \\[6pt]
\qquad\qquad\qquad + b_{m2}^2 \cos^2(\phi_{m1} - \theta_{m2}) - d^2 \sin^2\phi_{m1}\Big)^{1/2}\Bigg\} \\[8pt]
\qquad ; \quad \phi_{t2,m1}\big|_{\beta_{m1}=0^o} \leq \phi_{m1} \leq \phi_{t1,m1}\big|_{\beta_{m1}=0^o} \\[8pt]
0 \qquad ; \quad \text{otherwise}
\end{cases}
$$

Eq (3.7)

The azimuth threshold angles $\phi_{t1,m1}$ and $\phi_{t2,m1}$ at MS_1, which are functions of β_{m1} are plotted in Fig. 3.4(a). The elevation threshold angle $\beta_{t,m1}$ is a function of ϕ_{m1} and plotted in Fig. 3.4(b) These threshold angles are used to define the angular limits for the partitions P_1 and P_2 (see Fig. 3.2), which are as follows,
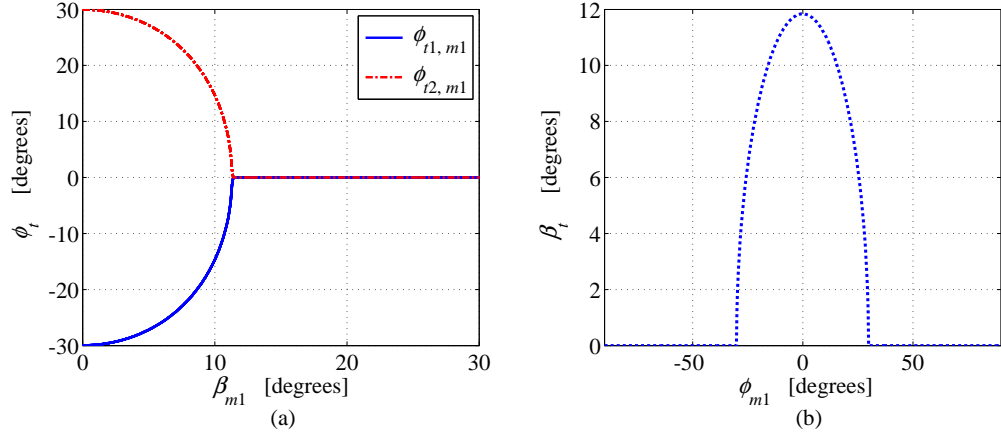
FIGURE 3.4: Threshold Angles, (a) Azimuth threshold angles, $\phi_{t,m1}$, w.r.t. elevation angle, β_{m1}, (b) Elevation threshold angle, β_t, w.r.t. azimuth angle, ϕ_{m1}, ($a_{m1} = 30$m, $b_{m1} = 20$m, $c_{m1} = 15$m, $a_{m2} = 55$m, $b_{m2} = 30$m, $c_{m2} = 20$m, $\theta_{m2} = 90^o$, and $d = 100$m).

$$\left.\begin{array}{c} \phi_{t1,m1} \leq \phi_{m1} \leq \phi_{t2,m1} \\ \\ \text{or} \\ \\ \beta_{t1,m1} \leq \beta_{m1} \end{array}\right\} \rightarrow P_1 \qquad Eq~(3.8)$$

$$\left.\begin{array}{c} \phi_{t2,m1} < \phi_{m1} < \phi_{t1,m1} \\ \\ \text{or} \\ \\ \beta_{m1} < \beta_{t1,m1} \end{array}\right\} \rightarrow P_2 \qquad Eq~(3.9)$$

where, the symbol " $\rightarrow$ " implies to a name for a partition based on certain conditions. The upper limit on the distance of scatterers from MS_1 in a particular direction can thus be obtained as follows,

$$r_{m1,\max} = \begin{cases} r_1 & ; \quad P_1 \\ \\ r_1 + \rho_{\beta 2} - \rho_{\beta 1} & ; \quad P_2 \end{cases} \qquad Eq~(3.10)$$

The distance of MS_1 from a certain scatterer at the boundary of scattering semi-spheroid around MS_1, can be expressed as

$$r_1 = a_{m1}b_{m1}c_{m1}\left(\frac{1}{2}c_{m1}^2\cos^2\beta_{m1}\left(a_{m1}^2 + b_{m1}^2 + (b_{m1}^2\right.\right.$$
$$\left.\left. -a_{m1}^2)\cos(2\theta_{m1} - 2\phi_{m1})\right) + 2a_{m1}^2 b_{m1}^2\sin^2\beta_{m1}\right)^{-1/2}$$

Eq (3.11)

The distances ρ_{β_1} and ρ_{β_2} are the distances of MS_1 from the points p and q (Fig. 3.3), respectively. These distances can be obtained as,

$$\left.\begin{matrix}\rho_{\beta_1}^+ \\ \\ \rho_{\beta_2}^-\end{matrix}\right\} = \begin{cases}\left(\dfrac{\rho_{\phi 1} + \rho_{\phi 2}}{2}\right)\sec\beta_{m1} - \dfrac{\sec\beta_{m1}}{2(b_\phi^2 + a_\phi^2\tan^2\beta_{m1})} \\ \\ \times\Bigg\{a_\phi^2(\rho_{\phi 1} + \rho_{\phi 2})\tan^2\beta_{m1} \\ \\ \qquad \pm\sqrt{a_\phi^2 b_\phi^2\left(4b_\phi^2 + \left(4a_\phi^2 - (\rho_{\phi 1} + \rho_{\phi 2})^2\right)\tan^2\beta_{m1}\right)}\Bigg\} \\ \\ \qquad ; \; \text{P}_2 \\ 0 \qquad\qquad ; \; \text{P}_1\end{cases}$$

Eq (3.12)

3.2   Derivation of AoA Statistics

In this section, we derive a mathematical expression for the joint probability density function of AoA seen at MS_1 through a radial distance r_m. The joint PDF of AoA, which is a function of radial distance r_m, azimuth angle ϕ_{m1}, and elevation angle β_{m1}, can be found as,

$$p(r_{m1}, \phi_{m1}, \beta_{m1}) = \frac{f(x_{m1}, y_{m1}, z_{m1})}{|J(x_{m1}, y_{m1}, z_{m1})|}\bigg|_{\substack{x_{m_1} = r_{m_1}\cos\beta_{m_1}\cos\phi_{m_1} \\ y_{m_1} = r_{m_1}\cos\beta_{m_1}\sin\phi_{m_1} \\ z_{m_1} = r_{m_1}\sin\beta_{m_1}}} \qquad Eq\ (3.13)$$

33

The Jacobean transformation in (3.13) can be written as,

$$
J(x_{m1}, y_{m1}, z_{m1}) = \begin{vmatrix} \dfrac{\partial x_{m1}}{\partial r_{m1}} & \dfrac{\partial x_{m1}}{\partial \phi_{m1}} & \dfrac{\partial x_{m1}}{\partial \beta_{m1}} \\[2mm] \dfrac{\partial y_{m1}}{\partial r_{m1}} & \dfrac{\partial y_{m1}}{\partial \phi_{m1}} & \dfrac{\partial y_{m1}}{\partial \beta_{m1}} \\[2mm] \dfrac{\partial z_{m1}}{\partial r_{m1}} & \dfrac{\partial z_{m1}}{\partial \phi_{m1}} & \dfrac{\partial z_{m1}}{\partial \beta_{m1}} \end{vmatrix}^{-1} = \dfrac{1}{r_{m1}^2 \cos \beta_{m1}} \qquad Eq\ (3.14)
$$

It is assumed that scatterers are uniformly distributed within the semi-ellipsoids, and hence scatterer density function for partitions P_1 or P_2 can be expressed as,

$$
f(x_{m1}, y_{m1}, z_{m1}) = \begin{cases} \dfrac{1}{V} & ; \quad (x_{m1}, y_{m1}, z_{m1}) \in (P_1 \ \ or \ \ P_2) \\[4mm] 0 & ; \quad \text{otherwise} \end{cases} \qquad Eq\ (3.15)
$$

Substituting $J(x_{m1}, y_{m1}, z_{m1})$ from (3.14) and $f(x_{m1}, y_{m1}, z_{m1})$ from (3.15) in (3.13), the joint probability density function is obtained as,

$$
p(r_{m1}, \phi_{m1}, \beta_{m1}) = \dfrac{r_{m1}^2 \cos \beta_{m1}}{V} \qquad Eq\ (3.16)
$$

Integrating (3.42) over r_{m1} for partitions P_1 and P_2, we get the joint PDF as,

$$
p(\phi_{m1}, \beta_{m1}) = \begin{cases} \dfrac{r_1^3 \cos \beta_{m1}}{3V} & ; \ P_1 \\[5mm] \dfrac{(r_1 + \rho_{\beta_2} - \rho_{\beta_1})^3 \cos \beta_{m1}}{3V} & ; \ P_2 \end{cases} \qquad Eq\ (3.17)
$$

Integrating (3.17) over β_{m1}, we obtain the marginal PDF of AoA with respect to azimuth plane i.e. $p(\phi_{m1})$ as,

$$
p(\phi_{m1}) = \int\limits_0^{\beta_{t,m1}} p(\phi_{m1}, \beta_{m1})\Big|_{P_2} d\beta_{m1} + \int\limits_{\beta_{t,m1}}^{\frac{\pi}{2}} p(\phi_{m1}, \beta_{m1})\Big|_{P_1} d\beta_{m1} \qquad Eq\ (3.18)
$$

34
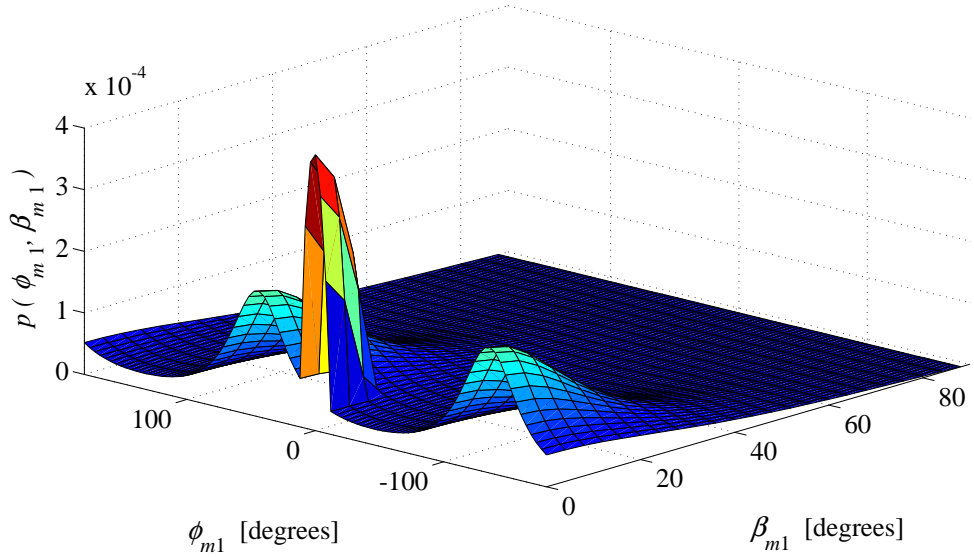
FIGURE 3.5: Joint probability density function of AoA seen at MS$_1$, (a_{m1} = 40m, b_{m1} = 30m, c_{m1} = 20m, θ_{m1} = 70°, a_{m2} = 35m, b_{m2} = 30m, c_{m2} = 25m, θ_{m2} = 60°, and d = 80m).

To get the marginal PDF of AoA with respect to elevation plane i.e. $p(\beta_{m1})$, integrating (3.17) over ϕ_{m1}, we have,

$$p(\beta_{m1}) = \int\limits_{0}^{\phi_{t1,m1}} p(\phi_{m1}, \beta_{m1})\Big|_{\mathrm{P_2}} d\phi_{m1} + \int\limits_{\phi_{t1,m1}}^{2\pi - \phi_{t2,m1}} p(\phi_{m1}, \beta_{m1})\Big|_{\mathrm{P_1}} d\phi_{m1}$$

$$+ \int\limits_{2\pi - \phi_{t2,m1}}^{2\pi} p(\phi_{m1}, \beta_{m1})\Big|_{\mathrm{P_2}} d\phi_{m1}$$

Eq (3.19)

Expressions for the angular statistics observed at the other end of communication link (i.e., MS$_2$) can also be obtained by following the similar procedure. The derived expressions for the angular statistics observed at MS$_1$ can be used for obtaining the statistics observed at MS$_2$, by exchanging all the parameters of MS$_1$ with MS$_2$ (e.g., exchanging c_{m1} with c_{m2} etc).
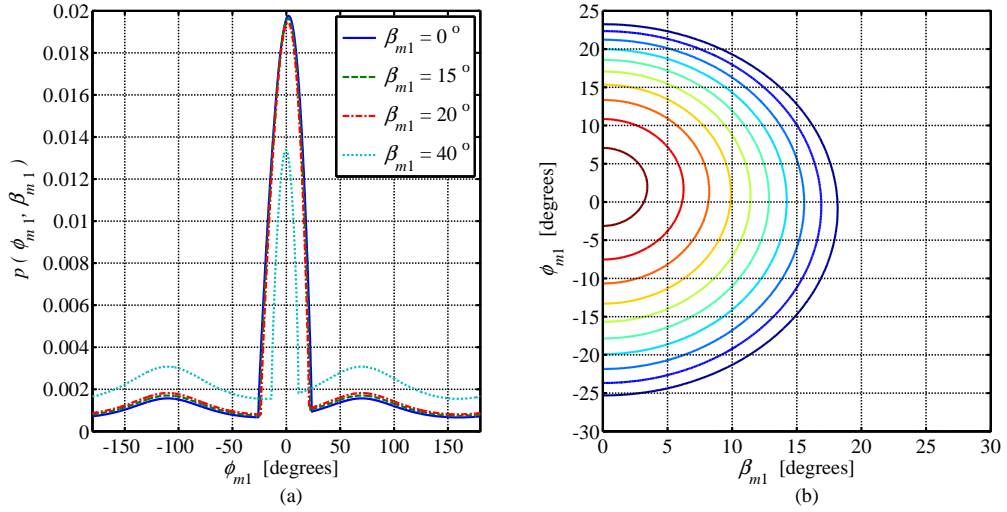
FIGURE 3.6: Joint PDF of AoA at MS_1 in (a) Azimuth plane for different elevation angles (b) , ($a_{m1} = 40$m, $b_{m1} = 30$m, $c_{m1} = 20$m, $\theta_{m1} = 70^o$, $a_{m2} = 35$m, $b_{m2} = 30$m, $c_{m2} = 25$m, $\theta_{m2} = 60^o$, and $d = 80$m).

3.3 Results and Discussion on AoA Statistics

In this section, we discuss the obtained theoretical results along with the observations. The results are obtained for the channel parameters shown in the caption of each plot. The joint PDF of AoA with respect to azimuth and elevation planes given in (3.17) is plotted in 3D as shown in Fig. 3.5. To elaborate the effects, a 2D plot of the joint PDF of AoA is also taken along with contour lines for different channel parameters is shown in Fig. 3.6. It is clear that joint PDF of AoA is higher at $\beta_{m1} = 0^o$ and $\phi_{m1} = 0^o$ because in this case the scattering radius is the largest in the LoS direction and a large number of scattering objects get chance to direct the radio signals over LoS or closer to it.

The AoA PDF decreases as the semi-ellipsoid is rotated through some angle in azimuth plane. Similarly, AoA PDF decreases with the increase in elevation angle and becomes minimum at maximum elevation angle which is an obvious result that lesser number of signals arrive from large elevation. The signals received at the receiver from the elevation plane are usually observed to be spread over an
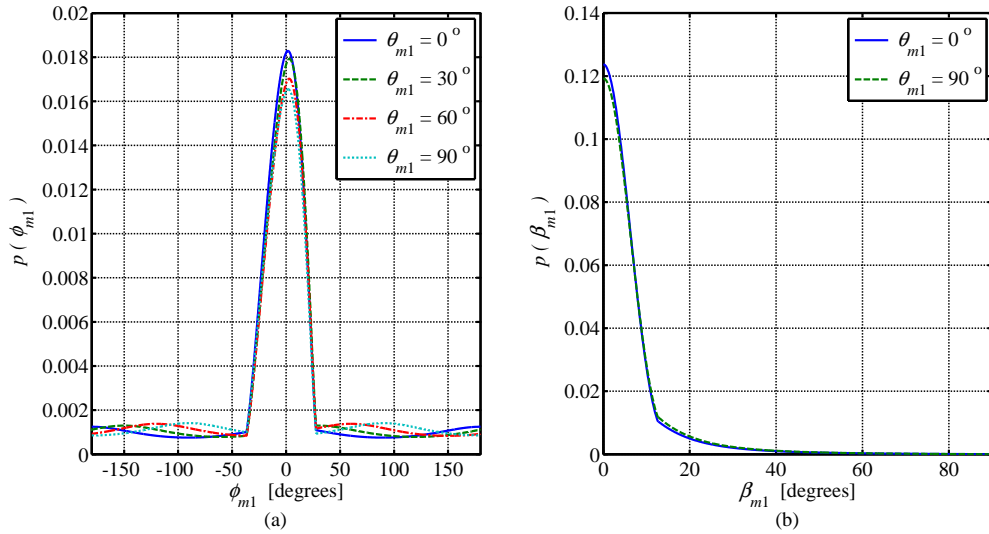
FIGURE 3.7: Marginal PDFs of AoA at MS_1 for different values of θ_{m1} in, (a) Azimuth plane (b) Elevation plane,($a_{m1} = 45$m, $b_{m1} = 35$m, $c_{m1} = 10$m, $a_{m2} = 60$m, $b_{m2} = 40$m, $c_{m2} = 20$m, $\theta_{m2} = 60^o$, and $d = 100$m).

angle of 20° [26], with more than 50% of energy in the signals arriving from the elevation angles below 16° [48].

Marginal PDFs of AoA in azimuth for different values of θ_{m1} is shown in 3.7(a). It exhibits higher values in the direction of LoS and lower values for NLoS azimuth angles. However, as θ_{m1} is increased from its value equal to zero, a slight decrease in the value of PDF in LoS direction is observed. This increases the rate of occurrence of the NLoS azimuth angles proportionally. Behavior of the marginal PDF of AoA curve in the azimuth for the azimuth angle other than those in the LoS or closer to it depends on the changes in the volume of the scattering region with the rotation of semi-ellipsoid1. It can be observed with the bumps or depressions in the curve on the way from 0° to 180°.

Marginal PDF of AoA in elevation is shown in 3.7(b). It shows same behavior as that of the PDF of AoA in azimuth for different values of θ_{m1}. However, the curve shows a gradual decrease in its value at 0° elevation angle to its minimum value at 90° elevation angle. The curve shows no bumps or depressions because
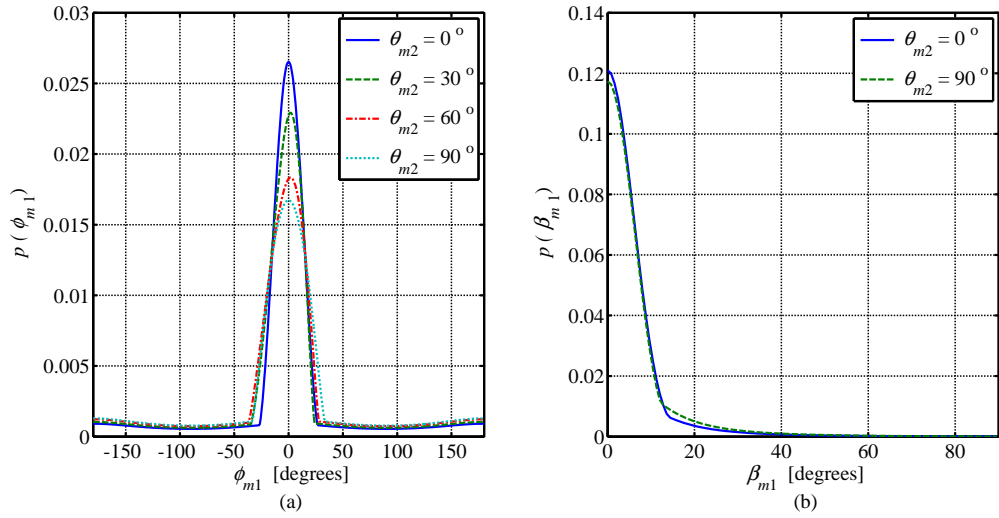
FIGURE 3.8: Marginal PDFs of AoA at MS_1 for different values of θ_{m2} in, (a) Azimuth plane (b) Elevation plane,($a_{m1} = 45$m, $b_{m1} = 35$m, $c_{m1} = 10$m, $\theta_{m1} = 0^o$, $a_{m2} = 60$m, $b_{m2} = 40$m, $c_{m2} = 20$m, and $d = 100$m).

of its corresponding change with the change in the volume due to rotation of semi-ellipsoid1.

Marginal PDFs of AoA in azimuth for different values of θ_{m2} is shown in 3.8(a). It can be observed from the figure that PDF of AoA is higher in the direction of LoS and lower for NLoS azimuth angles. As θ_{m2} is increased from its lower value to higher, a significant decrease in the value of PDF of AoA in LoS direction is observed. The PDF of AoA curve shows a slight decrease for the azimuth angles other than those in the LoS has lower values for higher azimuth angles and vice versa.

Marginal PDF of AoA w.r.t. the elevation AoA is plotted in 3.8(b). It shows similar behavior as that of the PDF of AoA in azimuth for different values of rotational angle θ_{m2}. However, the graph shows a gradual decrease in its value for 0° elevation angle to its minimum value at 90° elevation angle.

Marginal PDF of AoA at MS$_1$ in azimuth and elevation planes for different values of c_{m1} are plotted in Fig. 3.9(a) and Fig. 3.9(b) respectively. The PDF of AoA in azimuth plane in LoS direction is higher for low elevations of semi-ellipsoid

38
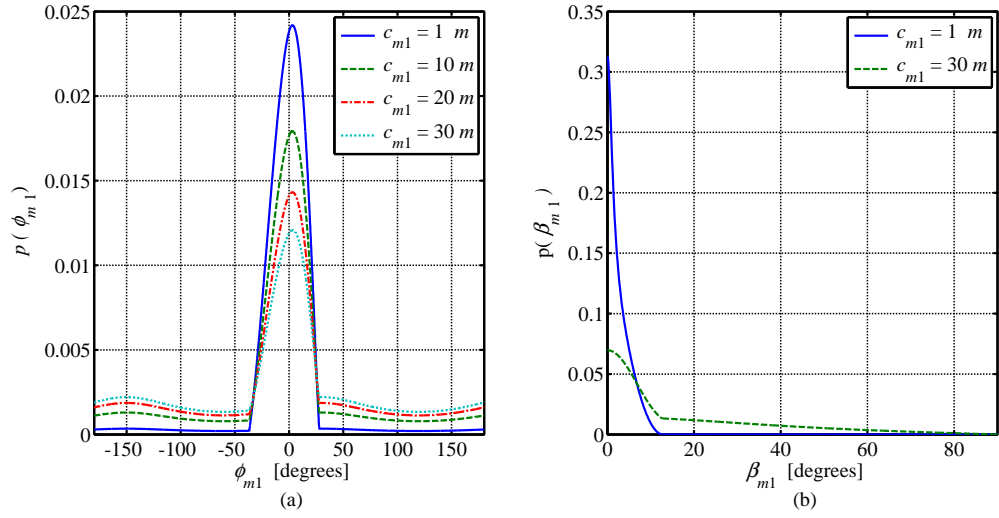
FIGURE 3.9: Marginal AoA PDF at MS_1 for different values of c_{m1} in (a) Azimuth plane (b) Elevation plane, ($a_{m1} = 45$m, $b_{m1} = 35$m, , $\theta_{m1} = 30^o$, $a_{m2} = 60$m, $b_{m2} = 40$m, $c_{m2} = 20$m, $\theta_{m2} = 20^o$, and $d = 100$m).
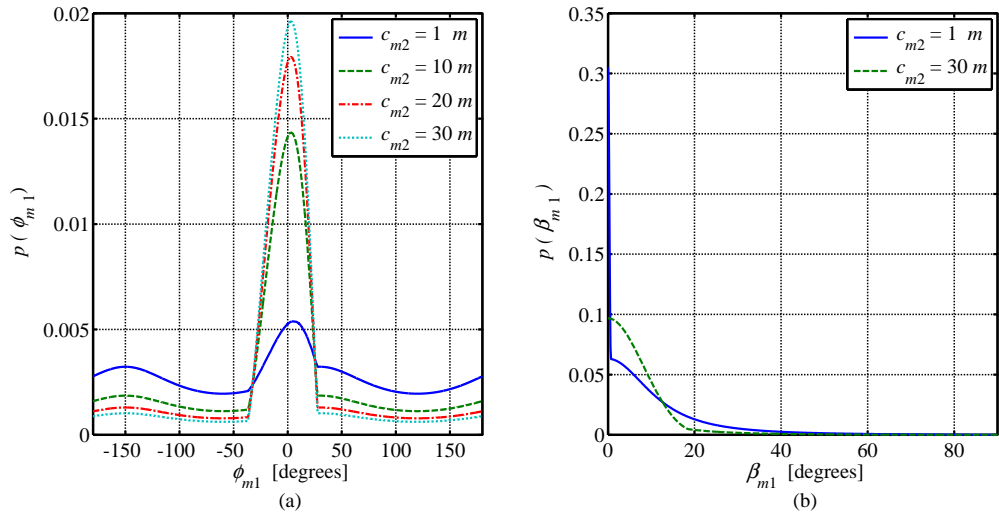
FIGURE 3.10: Marginal AoA PDF at MS_1 for different values of c_{m2} in (a) Azimuth plane (b) Elevation plane, ($a_{m1} = 45$m, $b_{m1} = 35$m, $c_{m1} = 30$m, $\theta_{m1} = 30^o$, $a_{m2} = 60$m, $b_{m2} = 40$m, $\theta_{m2} = 0^o$, and $d = 100$m).

around MS_1, while it has lower value in the NLoS directions and vice versa. It is because, the scattering objects in the region P_1 around MS_1 become lesser and lesser in number in the LoS direction with increasing elevations of semi-ellipsoid1 as compared to those present in the whole volume around MS_1. AoA PDF in elevation plane is considerably high for higher values of c_{m1} because scattering volume P_2 in the LoS direction increases with an increase in the whole volume around both the mobile stations.

Marginal PDF of AoA at MS_1 in azimuth and elevation planes for different values of c_{m2} are plotted in Fig. 3.10(a) and Fig. 3.10(b), respectively. It is shown that AoA PDF in azimuth plane increases in the LoS direction and decreases in the NLoS directions with an increase in c_{m2}, but the effect of increasing c_{m2} on the PDF of AoA in elevation is more significant, as shown in Fig. 3.10(b).
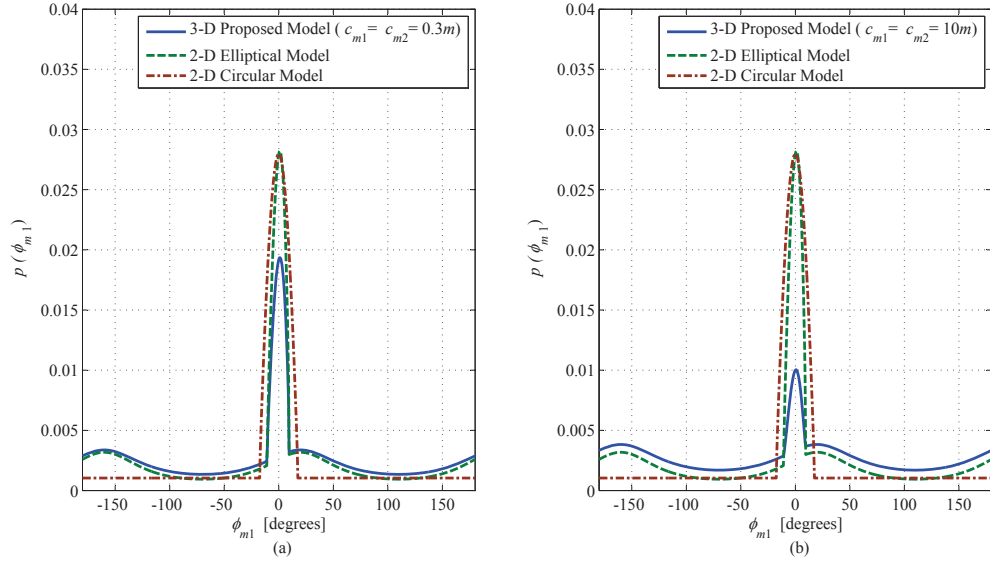
FIGURE 3.11: Comparison of Marginal PDFs of azimuth AoA observed at MS_1 for the Proposed 3D Model with 2D Circular Model [1] and 2D Elliptical Model [2], (a) for $c_{m1} = c_{m2} = 0.3$m, (b) for $c_{m1} = c_{m2} = 10$m, (For 3D Ellipsoidal and 2D Elliptical Models, $a_{m1} = 30$m, $b_{m1} = 20$m, $\theta_{m1} = 20^o$, $a_{m2} = 20$m, $b_{m2} = 15$m, $\theta_{m2} = 45$ and $d = 100$m), (For 2D Circular Model, Radii of scattering circular regions around MS_1 and MS_2 are taken as $R_1 = 30$m and $R_2 = 30$m, respectively).

In Fig. 3.11 (a and b), a comparison of the proposed 3D model with a 2D elliptical model [2] is presented, where the effect of increasing the number of scatterers in

elevation plane can be observed. As we reduce the the radius of the scattering ellipsoidal in elevation axis (i.e., reducing c_{m1} and c_{m2}), the results for the PDF of azimuth AoA for the proposed 3D model approaches to those obtained in [2]. Moreover, a comparison of the proposed 3D model with a 2D circular model [1] is also presented in Fig. 3.11 (a and b). If we substitute equal values for major and minor axes of the scattering semi-ellipsoids along horizontal plane (i.e., $a = b$) and a very small value for the vertical axis c (i.e., c approaches to zero), the proposed ellipsoidal model deduces to the 2D circular model [1]. In view of the results shown in Fig. 3.9, Fig. 3.10, and Fig. 3.11, it is concluded that the elevation plane has a prominent role in modeling the spatial characteristics of M2M channels. It is, therefore, necessary to take elevation plane into account in modeling AoA PDF for the performance evaluation of M2M communication links in multipath fading environments.

3.4   Overview of the proposed model

In this section, a overview of the 3D semi-ellipsoidal geometrical channel model for mobile-to-mobile (M2M) communication environments is presented. The 3D model developed in Section 3.1 is extended for the derivation of temporal statistics. The mobile stations, MS_1 and MS_2, are located at points $(0, 0, 0)$ and $(d, 0, 0)$, respectively, in the cartesian coordinate system. The horizontal distance between MS_1 and MS_2 is d. Uniform distribution of scatterers is considered to model the scatterers in the vicinity of both the mobile stations. Scattering objects are kept confined within semi-ellipsoidal shaped regions of different dimensions around both the mobile stations. Both the scattering semi-ellipsoids around MS_1 and MS_2 are made rotatable around their vertical axes to adapt various M2M communication environments, like, to account orientation of a certain street or canyon. The angles of their rotation w.r.t. the LoS direction are shown by θ_1 and θ_2 for the scattering ellipsoids around MS_1 and MS_2, respectively. The geometrical and other relevant parameters of the proposed model shown in Fig. 3.12 are defined in Table 3.1.
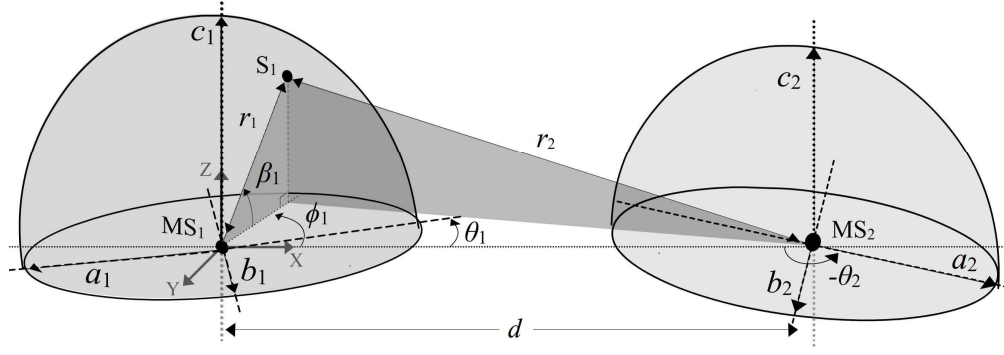
FIGURE 3.12: Proposed M-to-M Scattering Model

TABLE 3.1: Definition of parameters in Fig. 3.12

Parameter	Definition
a_1, b_1, c_1	Dimensions of scattering semi-ellipsoid around MS_1
a_2, b_2, c_2	Dimensions of scattering semi-ellipsoid around MS_2
S_1	A scattering object corresponding to the arrival of signal at the receiver
r_1, r_2	Distance of a certain scatterer from MS_1 and MS_2, respectively.
ϕ_1, ϕ_2	Azimuth angles of signal's arrival w.r.t LoS direction observed at MS_1 and MS_2, respectively.
β_1, β_2	Elevation angle of signal's arrival w.r.t. ground plane observed at MS_1 and MS_2, respectively.
ϕ_{t1}, ϕ_{t2}	Azimuth threshold angles to separate among various partitions of scattering regions.
β_t	Elevation threshold angle to separate among various partitions of scattering regions.
θ_1, θ_2	Angles of rotation of the semi-ellipsoids around M_1 and M_2, respectively
ξ_a, ξ_b	Semi-major and -minor axes of the vertical ellipse, ξ_ϕ, formed for a certain azimuth angle of observation.

The rotatable semi-ellipsoids in cartesian coordinates system can be expressed as,

$$\frac{\big((x - x_m)\cos\theta_m + (y - y_m)\sin\theta_m\big)^2}{a_m^2}$$

$$+\frac{\big(-(x - x_m)\sin\theta_m + (y - y_m)\cos\theta_m\big)^2}{b_m^2}$$

$$+\frac{(z - z_m)^2}{c_m^2} = 1$$

$$Eq\ (3.20)$$

where, (x_m, y_m, z_m) is the position of MS$_m$. The subscript m can take values, $m = 1$ and $m = 2$ to represent MS$_1$ and MS$_2$, respectively. Relationship of transformations between cartesian and spherical coordinates systems can be expressed as,

$$x_m = r_m \cos \phi_m \cos \beta_m, \; y_m = r_m \cos \beta_m \sin \phi_m, \text{ and } z_m = r_m \sin \beta_m$$

The volume of all the scattering region around both the mobile stations can be represented by volume V, which can be obtained as

$$V = \frac{2\pi}{3} a_1 b_1 c_1 + \frac{2\pi}{3} a_2 b_2 c_2 \qquad\qquad Eq\ (3.21\,)$$

The scattering objects, which contribute in the signal's arrival, are shown in two partitions viz: P$_1$ and P$_2$. These partitions are defined as sets of azimuth and elevation angles, which separate among various regions of scatterers based upon the geometrical composition. While observing at MS1, P$_2$ corresponds to those angles where only the local scattering semi-ellipsoid are the contributing scatterers. Whereas, P$_1$ corresponds to the range of angles for which the scattering semi-ellipsoid around MS2 are also visible. These azimuth and elevation threshold angles are used to define the angular limits for the partitions P$_1$ and P$_2$ (see Fig. 3.13), which are as follows,

$$\left. \begin{cases} \phi_{t1} \leq \phi_1 \leq \phi_{t2} \\[4pt] \text{or} \\[4pt] \beta_{t1} \leq \beta_1 \end{cases} \right\} \rightarrow \text{P}_1 \qquad\qquad Eq\ (3.22\,)$$

$$\left. \begin{cases} \phi_{t2} < \phi_1 < \phi_{t1} \\[4pt] \text{or} \\[4pt] \beta_1 < \beta_{t1} \end{cases} \right\} \rightarrow \text{P}_2 \qquad\qquad Eq\ (3.23\,)$$

43

FIGURE 3.13: Threshold angles in azimuth and elevation planes to separate among different partitions of the scattering region, (a) Top view of the geometry of scattering regions(b) Side view of the geometry of scattering regions

where, the symbol " $\rightarrow$ " implies to a name for a partition based on certain conditions.

The azimuth threshold angles (i.e. ϕ_{t1} and ϕ_{t2}) are the angles formed with line from the observing MS (i.e. MS_1) to the tangent points (k and l) at the vertical ellipse formed around MS_2 for a certain elevation angle, β_1 w.r.t. the LoS axis. These threshold angles are shown in Fig. 3.13(a) and can be expressed in simplified form as,

$$
\left.\begin{array}{c} \phi_{t1}^{+} \\[4pt] \phi_{t2}^{-} \end{array}\right\} =
\begin{cases}
\begin{aligned}
&\arctan\left\{\frac{1}{c_2^2 d^2 - \gamma\left(a_2^2\cos^2\theta_2 + b_2^2\sin^2\theta_2\right)}\right.\\[6pt]
&\quad\times\left\{\gamma(a_2^2 - b_2^2)\cos\theta_2\sin\theta_2 \pm \left(b_2^2 c_2^2 d^2 \gamma\cos^2\theta_2\right.\right.\\[6pt]
&\qquad\qquad\left.\left.\left. + a_2^2 d^2 c_2^2 \gamma\sin^2\theta_2 - a_2^2 b_2^2 \gamma^2\right)^{1/2}\right\}\right\}\\[6pt]
&\qquad\qquad ;\ \beta_1 < \arctan\left(\tfrac{c_2}{d}\right)\\[6pt]
&0 \qquad\qquad\quad ;\ \text{otherwise}
\end{aligned}
\end{cases},
\qquad Eq\ (3.24)
$$

where, $\gamma = c_2^2 - d^2\tan^2\beta_1$. Similarly, the threshold angle, β_t, separates the said two partitions in the elevation plane. This is the angle formed between LoS axis and the line joining the observing MS (i.e. MS_1) with the tangent point (i.e. h) at the vertical semi-ellipse (i.e. ξ_{ϕ_1}) around the MS_2 for a certain azimuth angle, ϕ_1. The elevation threshold angle can be expressed as,

$$
\beta_t =
\begin{cases}
\arctan\left(\dfrac{\xi_b}{\sqrt{\Psi^2 - \xi_a^2}}\right) & ;\ \left.\phi_{t2}\right|_{\beta_1 = 0^o} \le \phi_1 \le \left.\phi_{t1}\right|_{\beta_1 = 0^o}\\[10pt]
0 & ;\ \text{otherwise}
\end{cases},
\qquad Eq\ (3.25)
$$

where, $\Psi = \frac{\rho_{\phi 1} + \rho_{\phi 2}}{2}$. The parameters ξ_a and ξ_b are the semi-major and semi-minor axes of the vertical semi-ellipse (ξ_{ϕ_1}, standing at points p and q seen at certain azimuth angle, ϕ_1), shown in Fig. 3.13(b), which can be derived as,

$$
\xi_a = \frac{a_2 b_2\sqrt{b_2^2\cos^2(\theta_2 - \phi_1) + a_2^2\sin^2(\phi_1 - \theta_2) - d^2\sin^2\phi_1}}{b_2^2\cos^2(\theta_2 - \phi_1) + a_2^2\sin^2(\theta_2 - \phi_1)},
\qquad Eq\ (3.26)
$$

and

$$
\xi_b = \frac{1}{a_2 b_2}\sqrt{a_2^2 b_2^2 c_2^2 - b_2^2 c_2^2\Lambda^2\cos^2(\theta_2 + \Upsilon) - a_2^2 c_2^2\Lambda^2\sin^2(\theta_2 + \Upsilon)},
\qquad Eq\ (3.27)
$$

where,

$$\Lambda = \sqrt{d^2 + \Psi^2 - 2\Psi d \cos \phi_1},$$

and

$$\Upsilon = \arcsin\left(\frac{\Psi \sin \phi_1}{\Lambda}\right).$$

A line extended in azimuth plane from MS_1 (observing) and intersects the ellipse (i.e. ξ_{β_1}) around MS_2 at points p and q. The distances from MS_1 to these intersection points are represented by $\rho_{\phi 1}^+$ and $\rho_{\phi 2}^-$, which can be expressed as,

$$\left. \begin{matrix} \rho_{\phi 1}^+ \\ \rho_{\phi 2}^- \end{matrix} \right\} = \begin{cases} \dfrac{-1}{a_2^2 \sin^2(\phi_1 - \theta_2) + b_2^2 \cos^2(\phi_1 - \theta_2)} \\[2mm] \times \left\{ d\left(a_2^2 \sin(\phi_1 - \theta_2) \sin \theta_2 - b_2^2 \cos(\phi_1 - \theta_2) \cos \theta_2\right) \right. \\[2mm] \left. \pm a_2 b_2 \sqrt{a_2^2 \sin^2(\phi_1 - \theta_2) + b_2^2 \cos^2(\phi_1 - \theta_2) - d^2 \sin^2 \phi_1} \right\} \\[2mm] \qquad ; \ \phi_{t2}\big|_{\beta_1 = 0^o} \leq \phi_1 \leq \phi_{t1}\big|_{\beta_1 = 0^o} \\[2mm] 0 \qquad ; \ \text{otherwise} \end{cases}.$$

Eq (3.28)

The distance of MS_1 from a certain scatterer at the boundary of scattering semi-ellipsoid around MS_1, can be expressed as

$$r_{1,\max} = \frac{a_1 b_1 c_1}{\sqrt{\frac{1}{2}c_1^2 \cos^2 \beta_1 \left(a_1^2 + b_1^2 + (b_1^2 - a_1^2)\cos(2\theta_1 - 2\phi_1)\right) + 2a_1^2 b_1^2 \sin^2 \beta_1}}$$

Eq (3.29)

The distances ρ_{β_1} and ρ_{β_2} are the distances of MS_1 from the points p and q (Fig. 3.13), respectively. These distances can be obtained as,

In elevation plane, a line extended from MS_1 intersects the vertical semi-ellipse formed around MS_2 at points g and i. The distance of MS_1 from these intersection points can be expressed as, (see Fig. 3.13(b)),

$$
\left.\begin{array}{c} \rho^+_{\beta_1} \\ \rho^-_{\beta_2} \end{array}\right\} = \left\{\begin{array}{ll} \Psi\sec\beta_1 - \dfrac{\sec\beta_1}{2(\xi_b^2 + \xi_a^2\tan^2\beta_1)} \times \left\{ 2\Psi\xi_a^2\tan^2\beta_1 \right. & ; \; P_2 \\[2ex] \left. \pm\sqrt{\xi_a^2\xi_b^2\left(4\xi_b^2 + \left(4\xi_a^2 - 4\Psi^2\right)\tan^2\beta_1\right)}\right\} & ; \; P_1 \end{array}\right.
$$

$$Eq\ (3.30)$$

3.5 Derivation of the PDF of ToA

In this section, we present derivation of the joint and marginal PDFs of ToA for the proposed 3D geometrical model described in Section 3.4. The distance of a certain scatterer from MS_1 and MS_2 is represented by r_1 and r_2, respectively. Thus propagation distance from MS_1 to MS_2 corresponding to a certain scatterer is,

$$l_p = r_1 + r_2 \qquad\qquad Eq\ (3.31)$$

The corresponding propagation delay can thus be expressed as,

$$\tau = \frac{l_p}{c} \qquad\qquad Eq\ (3.32)$$

The smallest and largest propagation delays corresponds from the longest and shortest paths, respectively. It is obvious that minimum propagation delay corresponds from the LoS path (i.e. for angles $\phi_1 = 0^o$ and $\beta_1 = 0^o$), which can be expressed as,

$$\tau_{min} = \frac{d}{c} \qquad\qquad Eq\ (3.33)$$

The maximum propagation delay can also be calculated by exploiting the geometrical composition of 3D scattering region. The longest propagation path correspond from the farthest scatterer among all the scatterers located anywhere in whole scattering region around both the MSs. The location of farthest scatterers will be along the major axis of semi-ellipsoid with longer major dimensions. The direction of major axes of semi-ellipsoid can be rotated with a certain angle θ_m. Therefore, dependant upon the angle of rotation of the scattering semi-ellipsoids, the maximum propagation path's distance can thus be expressed as,

$$d_{\max} = \begin{cases} a_1 + \sqrt{a_1^2 + d^2 - 2a_1 d \cos \alpha_1} & ; \ a_1 > a_2 \\ \\ a_2 + \sqrt{a_2^2 + d^2 - 2a_2 d \cos \alpha_2} & ; \ a_1 < a_2 \end{cases} \qquad Eq \ (3.34)$$

where, the angle α_m takes the value as,

$$\alpha_m = \begin{cases} \pi - \theta_m & ; \ 0 \le \theta_m < \pi/2 \\ \\ \theta_m & ; \ \pi/2 \le \theta_m < \pi \end{cases} \qquad Eq \ (3.35)$$

Thus, the maximum propagation delay arise from the longest path, which can be expressed as,

$$\tau_{max} = \frac{d_{max}}{c} \qquad Eq \ (3.36)$$

When observing in a particular direction (for given ϕ_m and β_m), the longest and shortest paths result in the longest and smallest propagation delay are given by,
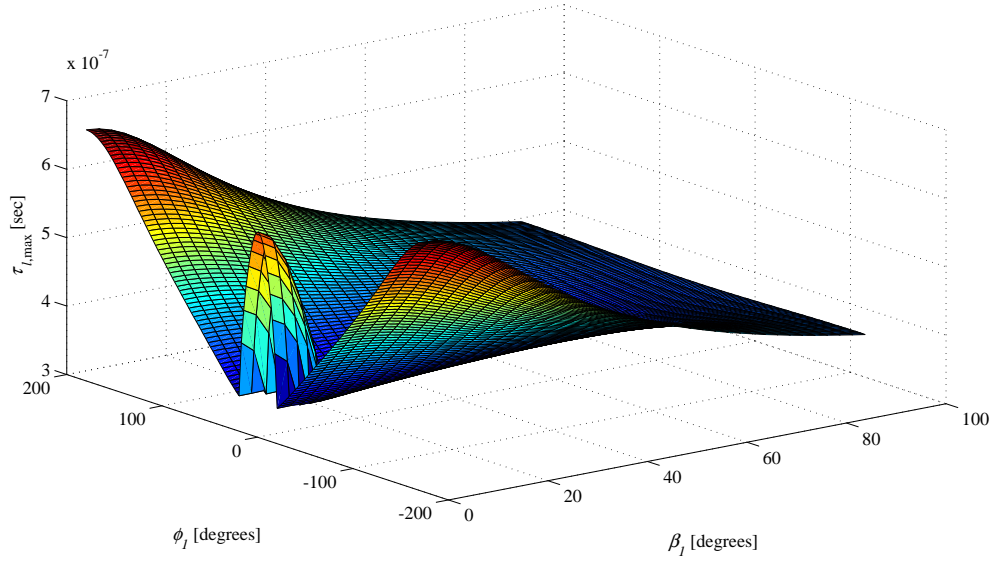
FIGURE 3.14: Delay limits for propagation paths w.r.t. to azimuth and elevation AoA, ($a_1 = 50$m, $b_1 = 40$m, $c_{1,o} = 20$m, $a_2 = 40$m, $b_2 = 30$m, $c_2 = 20$m, $\theta_1 = 0^o$, $\theta_2 = 0^o$, $d = 100$m).

$$\tau_{l,max}(\phi_1, \beta_1) =$$
$$\begin{cases} \dfrac{\rho_\beta^- + \sqrt{\rho_\beta^2 + d - 2\ d\ \rho_\beta^-\ \cos\phi_1 \cos\beta_1}}{c} & ; P_1 \\ \dfrac{r_1(\phi_1, \beta_1) + \sqrt{r_1^2(\phi_1, \beta_1) + d^2 - 2\ d\ r_1(\phi_1, \beta_1)\cos\phi_1\ \cos\beta_1}}{c} & ; P_2 \end{cases}$$

$$Eq\ (3.37)$$

and

$$\tau_{l,min}(\phi_1, \beta_1) = \tau_{min} = \frac{d}{c} \qquad Eq\ (3.38)$$

In order to demonstrate the trend of upper limit on propagation delay, the maximum directional propagation delay, $\tau_{l,max}$ w.r.t. azimuth and elevation angles is plotted in Fig. 3.14

49

For a particular direction, r_2 can be expressed as,

$$r_2 = \sqrt{r_1^2 + d^2 - 2dr_1 \cos\beta_1 \cos\phi_1} \qquad Eq\ (3.39)$$

by substituting (3.39) in (3.32), an expression for r_1 can be obtained as,

$$r_1 = \frac{c^2\tau^2 - d^2}{2(c\tau - d\cos\beta_1 \cos\phi_1)} \qquad Eq\ (3.40)$$

The joint trivariate function for PDF of ToA and AoA can be obtained as in [27],

$$p(\tau, \phi_1, \beta_1) = \frac{p(r_1, \phi_1, \beta_1)}{|J(r_1, \phi_1, \beta_1)|} \qquad Eq\ (3.41)$$

The joint density, $p(r_1, \phi_1, \beta_1)$, for 3D semi-ellipsoidal model is derived in [49], which can be expressed as,

$$p(r_1, \phi_1, \beta_1) = \frac{r_1^2 \cos\beta_1}{V} \qquad Eq\ (3.42)$$

Substituting the value of r_1 from (3.40) in (3.42), we get

$$p(r_1, \phi_1, \beta_1) = \frac{(c^2\tau^2 - d^2)^2 \cos\beta_1}{2V(c\tau - d\cos\beta_1 \cos\phi_1)} \qquad Eq\ (3.43)$$

The Jacobean Transformation, $J(r_1, \phi_1, \beta_1)$, in (3.41) can be found as,

$$J(r_1, \phi_1, \beta_1) = \left|\frac{\partial r_1}{\partial\tau}\right|^{-1} = \frac{2(d\cos\beta_1 \cos\phi_1 - c\tau)^2}{c(d^2 + c^2\tau^2 - 2c\tau d\cos\beta_1 \cos\phi_1)} \qquad Eq\ (3.44)$$

Substituting (3.43) and (3.44) in (3.41), we get the joint trivariate density function of the temporal and spatial characteristics of multipath signals for the proposed M2M model as,

$$p(\tau, \phi_1, \beta_1) = \begin{cases} \dfrac{c(d^2 - c^2\tau^2)^2(c^2\tau^2 + d^2 - 2c\tau\cos\phi_1\cos\beta_1)\cos\beta_1}{8V(d\cos\beta_1\cos\phi_1 - c\tau)^4} \\ \qquad\qquad ; \tau_{min} \leq \tau \leq \tau_{max} \\ 0 \qquad\qquad ; \text{otherwise} \end{cases} \qquad Eq\ (3.45)$$

The joint PDF of ToA and azimuth AoA can thus be obtained as,

$$p(\tau, \phi_1) = \int\limits_0^{\pi/2} p(\tau, \phi_1, \beta_1) d\beta_1 \qquad\qquad Eq\ (3.46)$$

The joint PDF of ToA and elevation AoA can be obtained by integration the obtained tri-variate function over azimuth AoA for its appropriate limits, as

$$p(\tau, \beta_1) = \int\limits_{-\pi}^{\pi} p(\tau, \phi_1, \beta_1) d\phi_1 \qquad\qquad Eq\ (3.47)$$

The marginal PDF of ToA can thus be derived as,

$$p(\tau) = \int\limits_{-\pi}^{\pi} \int\limits_0^{\pi/2} p(\tau, \phi_1, \beta_1) d\beta_1 d\phi_1 \qquad\qquad Eq\ (3.48)$$

3.6 Results and Description on Temporal Statistics

In this section, we discuss the obtained theoretical results of the geometrically based 3D ellipsoid channel model based for M2M communication environment. Joint PDF of ToA and AoA in azimuth plane is plotted in 3D as shown in Fig. 3.15(a), whereas its 2D plot with the same parameters is shown in Fig. 3.15(b). It can be observed that, for all the propagation delays, the probability of the
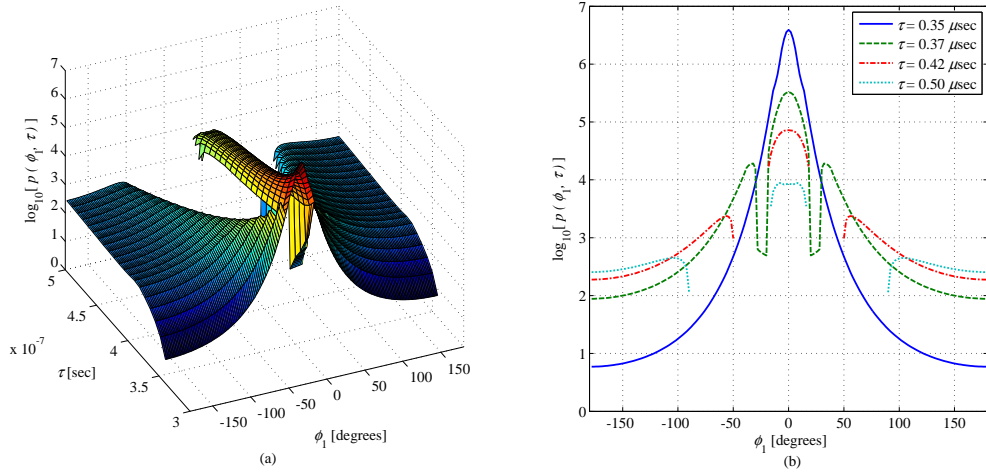
FIGURE 3.15: Joint probability density function of angle-of-arrival seen at MS_1, ($a_1 = 65$m, $b_1 = 40$m, $c_1 = 30$m, $a_2 = 55$m, $b_2 = 35$m, $c_2 = 30$m, $\theta_1 = 0^o$, $\theta_2 = 0^o$, $d = 100$m).

arrival of signal is higher for the physical angles around LoS direction. In the LoS direction (i.e., $\phi_1 = 0^o$), the number of contributing multipath signals are in higher number with shorter propagation length; therefore, the PDF has higher value for less propagation delay and increases as the delay increases. However, the PDF exhibits converse behavior for the physical angles away from LoS direction. For instance, when observing the direction opposite to the LoS direction (i.e., $\phi_1 = 180^o$), the value of PDF increases with an increase in the propagation delay. This is because, for these angles, most of the multipaths have longer propagation paths. These results for azimuth plane are applicable for the scenarios of downtown city areas where both the MSs are surrounded by high rise buildings and a large number of contributing scatterers are present in the vicinity of MSs.

The probability of arrival of signals from elevation plane has significant importance for the scenarios when the communicating nodes are surrounded by high-rise structures in their vicinity. In order to gauge and demonstrate the importance of the scatterers in elevation plane, the joint PDF of ToA and AoA in elevation plane is also shown in Fig. 3.16(a and b), where, it can be observed that the probability of arrival of the signals from scatterers with large elevation angles is very high, specially for the elevation angular span of 0° to 12°. It can also be observed that

52
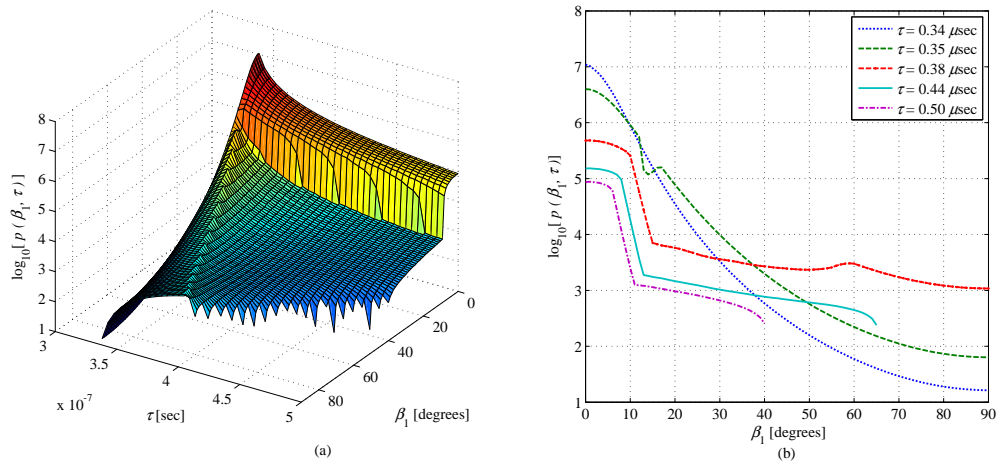
FIGURE 3.16: Joint probability density function of angle-of-arrival seen at MS_1, ($a_1 = 65$m, $b_1 = 40$m, $c_1 = 30$m, $a_2 = 55$m, $b_2 = 35$m, $c_2 = 30$m, $\theta_1 = 0^o$, $\theta_2 = 0^o$, $d = 100$).

the time span of propagation delay (i.e., $\tau_{l,\min}$ to $\tau_{l,\max}$) reduces with an increase in the elevation angle.

In order to validate the temporal characteristics of the 3D ellipsoid channel model for M2M environment, a comparison of the obtained results with those of the existing notable channel models found in the literature, for the scenarios of F2M and M2M communications is presented. The comparative analysis of our results with the existing 2D channel models [1, 2, 17] and 3D [26, 27] channel models for the marginal PDF of ToA is shown in Fig. 3.17. Hence it can be said that the geometrically based 3D ellipsoid channel model is more helpful than the existing conventional M2M channel models in designing more realistic M2M communication links in downtown city areas with high-rise buildings. Such modeling approach may prevent any practical degradation in the performance which might be ignored by using existing M2M models.

Effect of the number of scatterers in the elevation plane on the marginal PDF of ToA is shown in Fig. 3.18. It can observed that for the higher values of propagation delay, when the number of scatterers in elevation plane increases, the value of PDF increases in order to accommodate the signals with more delays.
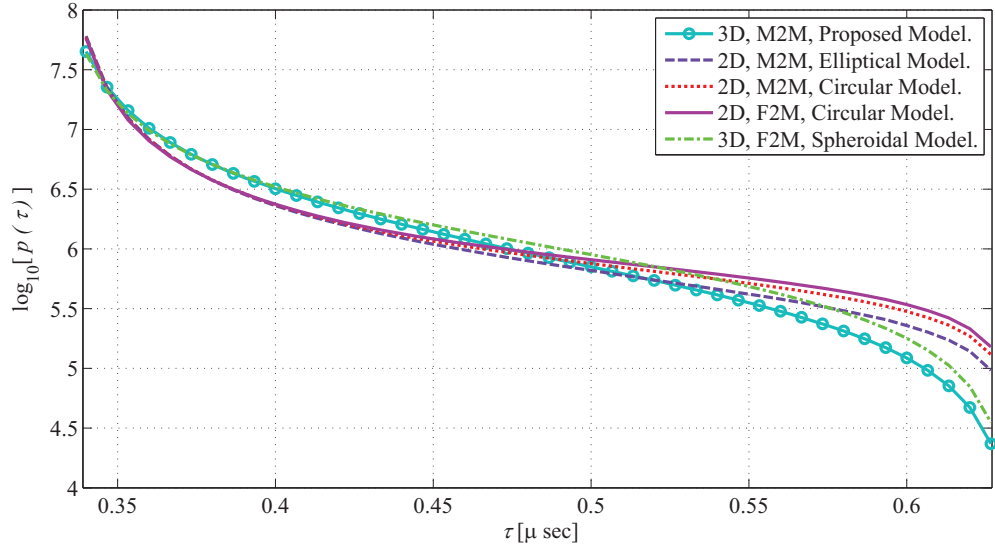
FIGURE 3.17: Comparison of the marginal probability density function of ToA of the proposed model with the existing models in the literature in F2M and M2M communication environment, ($a_1 = 65$m, $b_1 = 40$m, $c_1 = 30$m, $a_2 = 55$m, $b_2 = 35$m, $c_2 = 30$m, $\theta_1 = 0^o$, $\theta_1 = 0^o$, $\theta_2 = 0^o$, $\theta_2 = 0^o$, $d = 100$m).
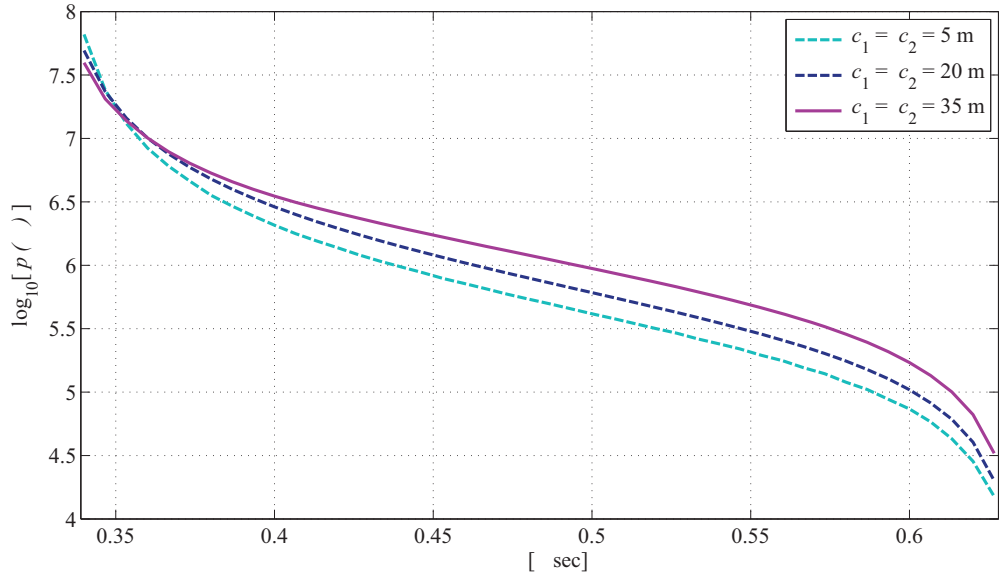
FIGURE 3.18: Marginal PDF of ToA seen at MS_1 w.r.t. elevation dimension of the semi-ellipsoids, ($a_1 = 50$m, $b_1 = 40$m, $a_2 = 35$m, $b_2 = 25$m, $\theta_1 = 0^o$, $\theta_2 = 90^o$, $d = 100$m).

3.7   Conclusion

In this section, we have analyzed the 3D semi-ellipsoid geometrical model of M2M communication channels for the temporal characteristics by assuming uniform

scatterer distribution around the mobile stations which are centered at the semi-ellipsoids. The semi-ellipsoids are rotatable around their vertical axes and their parameters can be adjusted according to the propagation environment with specific street orientation. For the 3D semi-ellipsoid channel model, we have derived closed-form expressions for the joint PDF of ToA and AoA in azimuth and elevation planes. We have also presented a simple integral formula for the marginal PDF of ToA of the received signals. For the validity of our derived results, we have compared them with those of some existing geometric channel models in the literature and showed that some popular 2D and 3D channel models are the special cases of the geometrically based 3D ellipsoid channel model. It was thus observed that a more realistic M2M channel model can predict any practical performance degradation before hand which might be overlooked by using existing M2M models

Chapter 4

DOPPLER SPECTRUM IN M2M COMMUNICATION CHANNELS

In this chapter, characterization of a 3D semi-ellipsoidal scattering model for M2M communication environment is presented. A brief literature survey related to the proposed work is discussed in Section 4.1. A detailed derivation of the expression for the PDF of power Doppler spectrum is given in Section 4.3. Results and discussion on the obtained PDF of power Doppler spectrum are presented in Section 4.4.

4.1 Literature survey

In mobile-to-mobile (M2M) communication environment, transmitting and receiving mobile stations (MSs) move with different speeds in arbitrary directions causing huge Doppler shifts. Due to the increased relative mobility of the both MSs and enormous angular spreads of the arriving signals, the resulting Doppler shifts in M2M communication environment are usually more than those of the fixed-to-vehicle (F2M) communication environment. The increased DS will in turn cause the signal power to vary more rapidly. This results in highly time-varying fading channels. Keeping in view the importance of the Doppler spectrum (DS), several researchers worked on the various statistical parameters of the channel in F2M and M2M environments using two-dimensional (2-D) and three-dimensional (3-D) geometrical channel models. Assuming 2-D propagation scenario and proposing circular and modified circular geometrical channel models, expression for the probability density function (pdf) of the DS is provided in [11, 30, 33, 34, 37, 50] for M2M communication environment. In such channel models, propagation of waves is assumed only in azimuth plane which is not the case in most of M2M communication environments because of low elevations of the antennas on the MSs. Due to the presence of high-rise buildings and surrounding objects in streets

and canyons in M2M communication scenario, 3-D channel models are introduced in [37,51] by taking elevation of the scattering objects into account. These models are also analyzed for DS using correlations in the multiple-input multiple-output (MIMO) links. In [25,28], 3-D scattering models for F2M and M2M communication environments are proposed and expressions for DS are derived assuming uniform distribution of scattering objects around the MSs. It was thought that geometrical channel models which consider elevation of the scattering objects are more realistic than those which consider propagation of signals only in azimuth plane. Semi-spheroid models presented in [46,52] are such geometrical channel models that consider elevated scattering objects for F2M communication environment. These models are analyzed for the DS and expressions for the pdf of AoA and DS are derived. Similar observations are made using geometrical channel models for vehicle-to-vehicle (V-to-V) and air-to-air (A-to-A) communication environments [53,54]. Recently, a 3-D semi-ellipsoid geometrical channel model is proposed in [49] for M2M communication environment which can be considered more appropriate realistic channel model than the previous existing models in the literature. The authors in [49], derived expressions for the joint and marginal pdfs of AoA in azimuth and elevation planes. In this section, we propose a 3-D hemi-spheroidal channel model for analysis of DS in M2M propagation environments. Mathematical expressions for the joint and marginal pdfs of DS in correspondence with received signal power and elevation AoA are derived.

We have developed a 3D semi-ellipsoid geometrical channel model for M2M communication and is presented in Chapter 3, where we have assumed that scatterers are uniformly distributed around the mobile stations within the semi-ellipsoidal regions. The proposed model is analyzed for the probability density function (PDF) of AoA in azimuth and elevation planes. Closed-form expressions for the joint PDF of AoA in azimuth and elevation planes are derived. Furthermore, this model can be used by exploring other statistics like time-of-arrival (ToA), Doppler spectrum, average fade duration (AFD), and level crossing rate (LCR) etc.
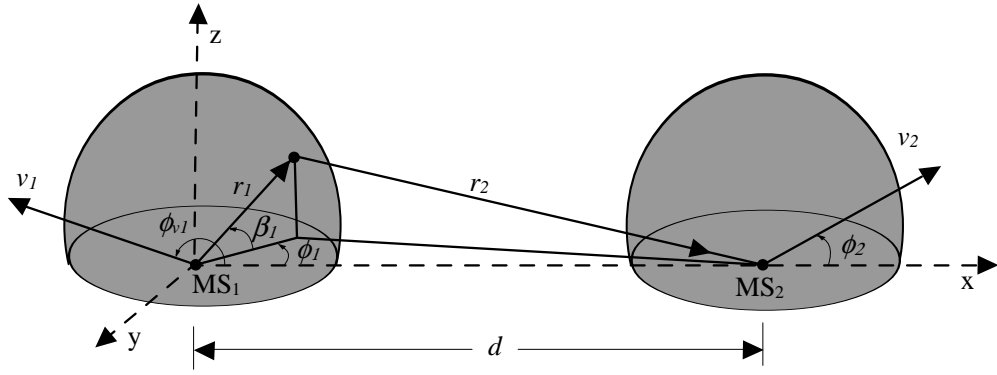
FIGURE 4.1: Scattering environment in M2M communication system

In this chapter, we analyze the the 3D semi-ellipsoid model for Doppler spectrum by deriving closed-form expressions for the joint PDF of AoA and Doppler spectrum.

4.2   Derivation of Doppler Spectrum

In this section, we present a detailed derivation of Doppler spectrum using the 3D semi-ellipsoid channel model which we have developed in Chapter 3 for M2M communication environment. The MS_1 and MS_2 are surrounded by scattering objects in semi-ellipsoid regions and moving with velocities v_1 and v_2 making angles ϕ_{v1} and ϕ_{v2} with the LoS direction, respectively as shown in Fig. 4.1.

To simplify further derivation, we use the concept of relative motion. We assume that MS_2 is fixed while MS_1 is in motion such that it moves with relative velocity, v_r, w.r.t MS_2 by making an angle, ϕ_{vr} with the LoS direction as shown in Fig. 4.3. The relative velocity of MS_1, in terms of v_1 and v_2, can be written as (see Fig. 4.2),

$$v_r = \sqrt{v_1^2 + v_2^2 - 2v_1v_2\cos\theta_{12}} \qquad\qquad Eq~(4.1)$$
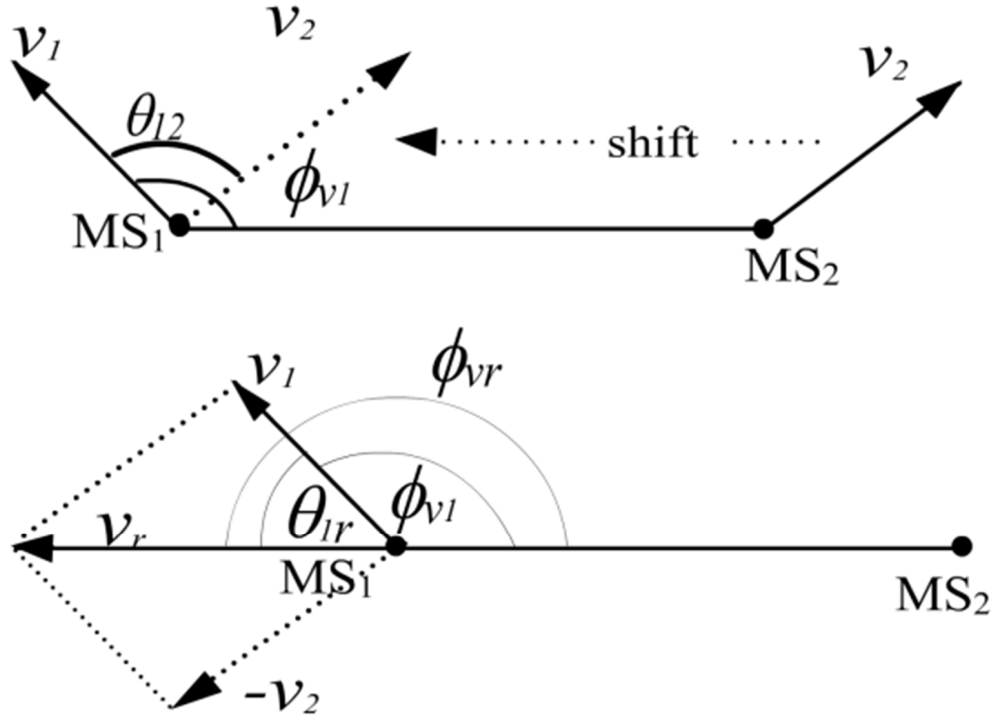
FIGURE 4.2: Relative velocity between the mobile stations

where θ_{12} is an angle between velocities v_1 and v_2. The angle of relative motion, ϕ_{vr}, can be written as,

$$\phi_{vr} = \phi_{v1} + \theta_{1r} \qquad\qquad Eq\ (4.2)$$

where θ_{1r} is the angle between velocities v_1 and v_{1r} and can be expressed as,

$$\theta_{1r} = \arccos\left(\frac{v_1^2 + v_r^2 - v_2^2}{2v_1 v_r}\right) \qquad\qquad Eq\ (4.3)$$

The angle of motion of MS_1 relative to MS_2 w.r.t. the arrival of the multipath signal can be expressed as,

$$\theta_{m1} = \phi_{vr} - \phi_{m1}, \qquad\qquad Eq\ (4.4)$$

A relation between the Doppler shift and arrival of the multipath signal from a scattering object located at certain elevation angle, β_{m1} can be expressed as,
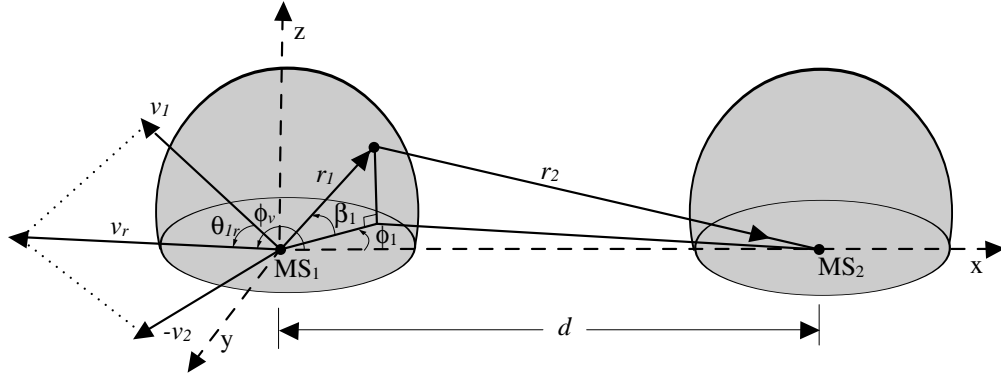
FIGURE 4.3: Equivalent diagram showing relative velocity keeping one end
fixed

$$f_{DS} = f_m \cos \theta_{m1} \cos \beta_{m1}, \qquad\qquad Eq \ (4.5)$$

where, $f_m = \frac{v_r f_c}{c}$ is the maximum Doppler shift due to the relative motion of MS_1 w.r.t. MS_2. Normalized doppler shift due to MS_1 can be obtained by dividing (4.5) by f_m as,

$$\gamma = \frac{f_{DS}}{f_m} = \cos \theta_{m1} \cos \beta_{m1}, \qquad\qquad Eq \ (4.6)$$

from the above equation,

$$\theta_{m1} = \arccos \left(\frac{\gamma}{\cos \beta_{m1}} \right), \qquad\qquad Eq \ (4.7)$$

rearranging (4.4) for ϕ_{m1} and putting value of θ_{m1} from (4.7) and ϕ_{vr} from 4.2 in (4.4), we get,

$$\phi_{m1} = \phi_{v1} + \arccos \left(\frac{v_1^2 + v_r^2 - v_2^2}{2v_1 v_r} \right) - \arccos \left(\frac{\gamma}{\cos \beta_{m1}} \right) \qquad Eq \ (4.8)$$

The propagation path length that a radio signal travels from MS_1 to a local scatterer or a scatterer around MS_2 to a final destination i.e., MS_2, can be written as,

$$l = r_1 + r_2 \qquad\qquad Eq \ (4.9)$$

where r_1 and r_2 are the distances of a particular scattering object from MS_1 and MS_2, respectively, as shown in Fig. 4.1. For a particular direction in azimuth and elevation planes, r_2, can be derived as,

$$r_2 = \sqrt{r_1^2 + d^2 - 2dr_1 \cos \beta_{m1} \cos \phi_{m1}}, \qquad\qquad Eq\ (4.10)$$

and

$$r_1 = \frac{l^2 - d^2}{2(l - d \cos \beta_{m1} \cos \phi_{m1})}. \qquad\qquad Eq\ (4.11)$$

The upper bound for propagation path distance,

$$l_{lim} = d_{m1,s} + \sqrt{d_{m1,s}^2 + d^2 - 2dd_{m1,s} \cos \beta_{m1} \cos \phi_{m1}} \qquad\qquad Eq\ (4.12)$$

where,

$$d_{m1,s} = \begin{cases} \rho_{\beta_2}^- & ;\ P_1 \\ r_1 & ;\ P_2 \end{cases} \qquad\qquad Eq\ (4.13)$$

$$l_{l,min}(\phi_1, \beta_1) = c \times \tau_{min} \qquad\qquad Eq\ (4.14)$$

4.3   Derivation of PDF Expressions

The joint trivariate function for PDF of ToA and AoA can be obtained as in [27],

$$p(l, \phi_{m1}, \beta_{m1}) = \frac{p(r_{m1}, \phi_{m1}, \beta_{m1})}{|J(l, \phi_{m1}, \beta_{m1})|} \qquad\qquad Eq\ (4.15)$$

The joint density function can be written as,

$$p(r_{m1}, \phi_{m1}, \beta_{m1}) = f(x_m, y_m, z_m)r_{m1}^2 \cos \beta_{m1} \qquad\qquad Eq\ (4.16)$$

where $f(x_m, y_m, z_m)$ is the scatterer density function. The Jacobean in (4.15) can be derived as,

$$J(r_{m1}, \phi_{m1}, \beta_{m1}) = \left| \frac{\partial r_1}{\partial \tau} \right|^{-1} = \frac{2(d \cos \beta_{m1} \cos \phi_{m1} - l)^2}{d^2 + l^2 - 2ld \cos \beta_{m1} \cos \phi_{m1}} \qquad Eq~(4.17)$$

substituting (4.16) and (4.17) in (4.15), we get

$$p(l_p, \phi_{m1}, \beta_{m1}) = \frac{f(x_m, y_m, z_m)(d^2 - l^2)^2(d^2 + l^2 - 2ld \cos \beta_{m1} \cos \phi_{m1})}{8 \sec \beta_{m1}(d \cos \beta_{m1} \cos \phi_{m1} - l)^4}$$

$$Eq~(4.18)$$

The received power p_r at any point on the propagation path can be expressed as,

$$p_r = p_o \left(\frac{l_p}{d} \right)^{-n} \qquad Eq~(4.19)$$

where p_o is power received in the LoS direction, l_p is the propagation path length in NLoS direction from MS_1 to MS_2 or vice versa. By making l_p the subject in (4.19), we get

$$l_p = d \left(\frac{p_r}{p_o} \right)^{-1/n} \qquad Eq~(4.20)$$

The joint power density function is,

$$p(p_r, \phi_{m1}, \beta_{m1}) = \frac{p(l_p, \phi_{m1}, \beta_{m1})}{|J(l_p, \phi_{m1}, \beta_{m1})|} \qquad Eq~(4.21)$$

The Jacobean Transformation $J(l_p, \phi_{m1}, \beta_{m1})$, can be derived as,

$$J(l_p, \phi_{m1}, \beta_{m1}) = \left| \frac{\partial l_p}{\partial p_r} \right|^{-1} = \frac{np_o}{d} \left(\frac{p_r}{p_o} \right)^{\frac{n+1}{n}} \qquad Eq~(4.22)$$

by substituting (4.22) in (4.21), we get the joint function of power level as,

$$
p(p_r, \phi_{m1}, \beta_{m1}) = \frac{\left(d^6 \left(\left(\frac{p_r}{p_o} \right)^{-2/n} - 1 \right)^2 f(x_m, y_m, z_m) \right)}{\left(8np_o \sec \beta_{m1} \left(\frac{p_r}{p_o} \right)^{\frac{n+1}{n}} \right)}
$$

$$
\times \frac{\left(d + d \left(\frac{p_r}{p_o} \right)^{-2/n} - 2d \left(\frac{p_r}{p_o} \right)^{-1/n} \cos \beta_{m1} \cos \phi_{m1} \right)}{\left(d \cos \beta_{m1} \cos \phi_{m1} - d \left(\frac{p_r}{p_o} \right)^{-1/n} \right)^4}
$$

$$Eq \ (4.23)$$

The joint density function for p_r, γ and β is obtained as,

$$
p(p_r, \gamma, \beta_{m1}) = \frac{p(p_r, \phi_{m1}, \beta_{m1})}{|J(p_r, \phi_{m1}, \beta_{m1})|} \Bigg|_{\phi_{m1} = \phi_{v1} + \arccos \left(\frac{v_1^2 + v_r^2 - v_2^2}{2v_1 v_r} \right) - \arccos \left(\frac{\gamma}{\cos \beta_{m1}} \right)} \qquad Eq \ (4.24)
$$

The Jacobean Transformation in (4.24) can be derived as,

$$
J(p_r, \phi_{m1}, \beta_{m1}) = \left| \frac{\partial \phi_{m1}}{\partial \gamma} \right|^{-1} = \sqrt{\cos^2 \beta_{m1} - \gamma^2} \qquad Eq \ (4.25)
$$

Let $\xi = (p_r/p_o)^{-1/n}$, the joint density function in (4.25) for the power level of the multipath component, elevation AoA, and Doppler spread can be rearranged as,

$$
p(p_r, \gamma, \beta_{m1}) = \sum_{i=1}^{2} \Bigg\{ \left(\frac{d^6 (\xi^2 - 1)^2 \xi^{n+1} f(x_m, y_m, z_m)}{8np_o \sqrt{1 - \gamma^2 \sec^2 \beta_{m1}}} \right) \qquad Eq \ (4.26)
$$
$$
\times \left(\frac{d + d\xi^2 - 2d\xi \cos \beta_{m1} \cos \phi_i}{(d \cos \beta_{m1} \cos \phi_i - d\xi)^4} \right) \Bigg\}
$$

where,

$$
\phi_i = \begin{cases} \phi_v + \arccos \left(\gamma \sec \beta_{m1} \right); & i = 1 \\[2mm] \phi_v - \arccos \left(\gamma \sec \beta_{m1} \right); & i = 2, \end{cases} \qquad Eq \ (4.27)
$$

Since $|\cos\theta_{m1}| \leq 1$, the upper bound for elevation AoA can be obtained from (4.6) as $\beta_{m1} \leq \arccos|\gamma|$. The joint pdf for the power and Doppler spectrum can be derived by integrating (4.26) over β_{m1} for its appropriate range, which is expressed as

$$p(p_r, \gamma) = \int_0^{\arccos|\gamma|} p(p_r, \gamma, \beta_{m1}) \mathrm{d}\beta_{m1}. \qquad\qquad Eq \ (4.28)$$

The integral in (4.28) cannot analytically be derived; however, it can be obtained by using numerical integration. The marginal PDF of the Doppler shift is obtained as,

$$p(\gamma) = \int_{p_l}^{p_u} p(p_r, \gamma) \mathrm{d}p_r. \qquad\qquad Eq \ (4.29)$$

The power spectral density can be obtained as in [17, 46],

$$S(\gamma) = \int_{p_l}^{p_u} p_r p(p_r, \gamma) \mathrm{d}p_r. \qquad\qquad Eq \ (4.30)$$

where p_u is the power received at MS_1 through shortest propagation path (i.e., $p_u = p_o$), and p_l is the power corresponding to the longest propagation path. Moreover, a signal received from longest propagation path would correspond to the lowest power level. The expression for the longest propagation path is given in (4.12) which is a function of azimuth and elevation AoA, can be used for determining the lowest power level. Thus the lower bound on the power level of multipath signals from certain direction can be obtained as,

$$p_l = p_o \left(\frac{l_{lim}}{d} \right) \qquad\qquad Eq \ (4.31)$$
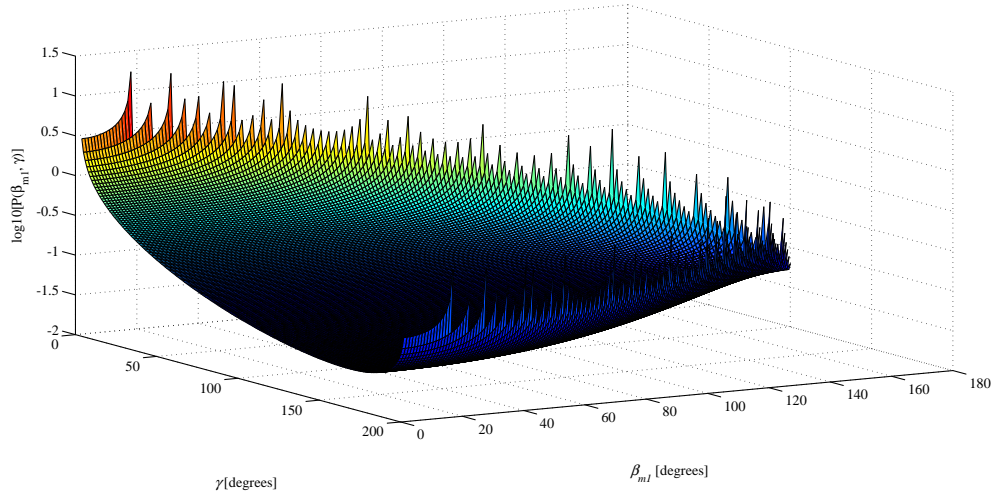
FIGURE 4.4: Joint PDF of Doppler shift and elevation AoA

4.4 Results and Description

In this section, discussions of the obtained theoretical results for the joint and marginal PDFs of the normalized Doppler shift are presented. These results are based on the mathematical derivations using the developed 3D semi-ellipsoid geometrical shape for M2M communication environment. Joint PDF $p(\gamma, \beta_{m1})$ of the normalized Doppler shift γ, and AoA in elevation plane, β_{m1} is shown in Fig. 4.4 for a case when MS_1 is moving towards stationary MS_2 or in direction of MS_1 motion with LoS, i.e., $\phi_{vr} = 0^o$. The 2D slices of Fig. 4.4 at different elevation angles, β_{m1} are shown in Fig. 4.5. Other model parameters and velocities of the MSs are given in the caption of the figures. From Fig. 4.4 and Fig. 4.5, two observations can be made. Larger values of the PDF of the normalized Doppler shift decrease with an increase in the elevation angle. Secondly, ascending or descending behavior of the joint PDF of the normalized Doppler shift depends on the angle of motion of MS_1 with LoS. The plot depicted in Fig. 4.5 shows the descending trend of the joint PDF with $\phi_{vr} = 0^o$, from $\gamma = -1$ to $\gamma = 1$. This is due to a fact that probability of less scattering objects in azimuth plane is higher for the higher elevation angles. The same ascending/descending trend with ϕ_{vr} is shown by the marginal PDF of the normalized Doppler shift.
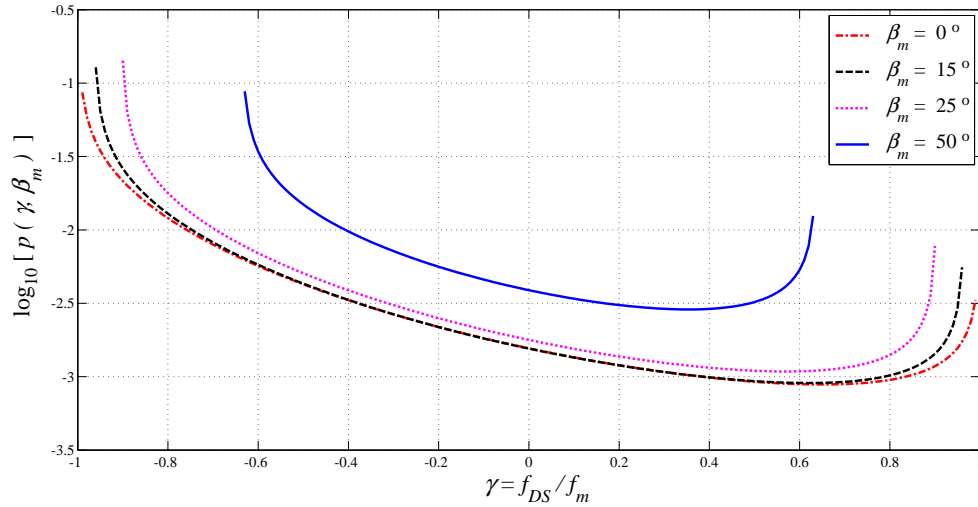
FIGURE 4.5: Joint PDF of Doppler shift and elevation AoA

The same ascending/descending trend with ϕ_{vr} is shown by the marginal PDF of normalized Doppler shift. The Marginal PDF of the normalized Doppler shift for different values of ϕ_{vr} is shown in Fig. 4.6. The purpose of the graph is to show the effect of the direction of the relative motion of the MS_1 on the distribution of the normalized Doppler shift. When the direction of motion of MS_1 is such that it moves away from MS_2 (i.e., when $\phi_{vr} = 180^o$), then the scatterers contributing towards the normalized Doppler shift in negative Doppler frequencies are more than positive Doppler frequencies, therefore, the PDF of the normalized Doppler shift is skewed towards negative frequencies. In a case, when MS_1 moves towards MS_2 (i.e., when $\phi_{vr} = 0^o$), then the scattering objects contributing to the normalized Doppler shift in positive Doppler frequencies are more than those contributing to it in the negative Doppler frequencies. That is why the PDF of the normalized Doppler shift is skewed towards positive frequencies. The PDF of the normalized Doppler shift is seen U-shaped and symmetrical at an angle, $\phi_{vr} = 90^o$. This is because multipath signals corresponding to scattering regions in positive and negative Doppler frequencies are nearly equal. Similar observations were made in [54] with a different modeling approach for air-to-air communication channels.
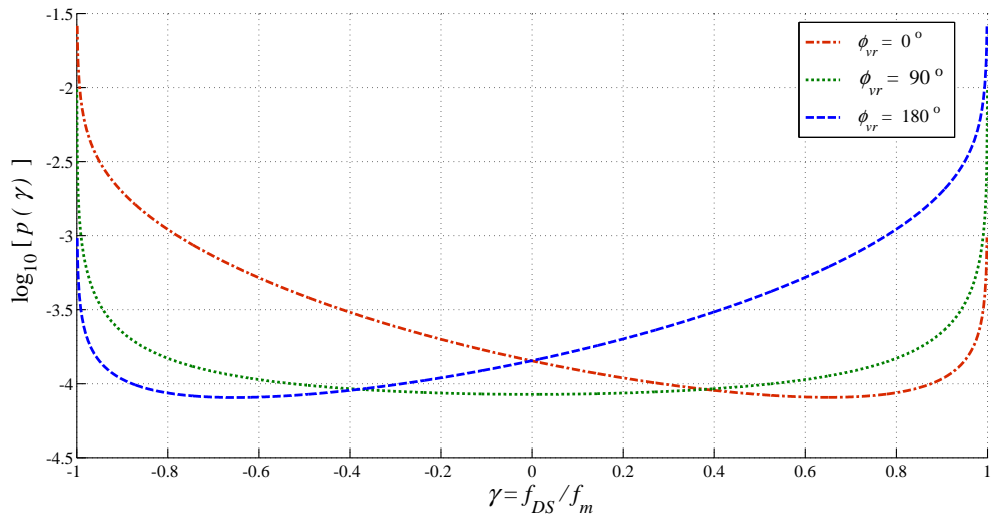
FIGURE 4.6: Distribution of normalized Doppler spread w.r.t. direction of relative motion of MS_1

Chapter 5

GENERALIZED CHANNEL MODEL FOR MOBILE-TO-MOBILE COMMUNICATION ENVIRONMENT

In this Chapter, a generalized 3D spatial channel model for M2M communication environment is presented. It is assumed that MSs are located inside scatterer-free semi-ellipsoids and scatterers are uniformly distributed outside the inner and inside the outer semi-ellipsoids. Using the proposed generalized channel model, expressions for the joint and marginal PDFs of AoA and ToA are derived in azimuth and elevation planes. System model of the proposed geometrical channel model is presented in Section 5.1. Derivation of expressions for the PDFs of AoA in azimuth and elevation planes along with their results and description are provided in Section 5.2. Analysis of the proposed model for the temporal characteristics is given in Section 5.3. Model validation and generalization is presented in Section 5.4. Finally, a conclusion of the chapter is presented is Section 5.5.

5.1 System Model

In this section, we present a geometrically-based generalized 3D channel model for M2M communication environments as shown in Fig.5.1. The proposed model is based on the following assumptions,

- Both the MSs are equipped with omnidirectional antennas.

- Both the MSs are at the same height assumed at ground level.

- The scattering region is defined by the non-overlapping portion of two concentric semi-ellipsoids of different dimensions centered at each MS.

- The scattering objects are assumed to be uniformly distributed kept confined within the defined scattering region.
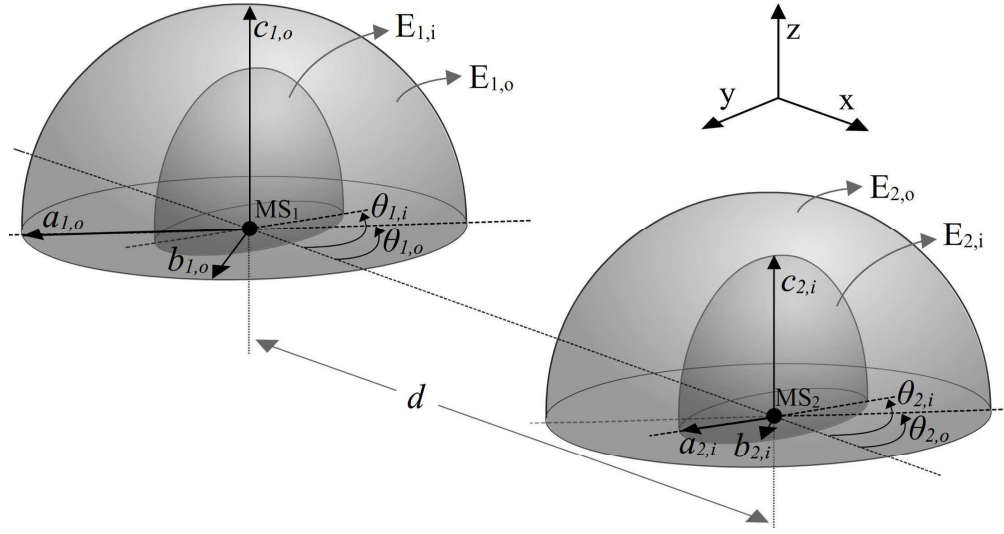
FIGURE 5.1: Proposed mobile-to-mobile scattering model.

- A scatterer (an isotropic obstacle) reflects the incident wave towards all the directions in the space with an equal power (omnidirectional lossless re-radiation).

- A single-bounce scattering environment is considered for the communication between the MSs. However, contributions of single-bounce reflections from both hollow semi-ellipsoids (local clusters) are considered simultaneously.

- Each multipath wave received at a certain MS contains equal power.

- All the scattering objects have uniform random phases and same scattering coefficients.

- The location of any scatterer is represented in the Cartesian coordinate system by (x_s, y_s, z_s) or in spherical coordinate system by (r_s, ϕ_s, β_s).

The semi-ellipsoids are represented by $E_{m,q}$, where the subscripts m and q are the indices to represent a certain MS and a certain ellipsoid (i.e., $m = 1$ for MS$_1$ and $m = 2$ for MS$_2$, $q = i$ for inner semi-ellipsoids and $q = o$ for outer semi-ellipsoids). The effective scattering region is defined by the volume $V_{m,o}$-$V_{m,i}$, is shown in Fig. 5.1. The dimensions of semi-ellipsoids along x, y and z axes are denoted by $a_{m,q}$,

$b_{m,q}$ and $c_{m,q}$. The inner semi-ellipsoid should not exceed the outer semi-ellipsoid in any dimension. This means that the length of the major axis of the inner semi-ellipsoid should be kept smaller or equal to the length of the minor axis of the outer semi-ellipsoid ($a_{m,i} \leq b_{m,o}$). The dimension of the semi-ellipsoid along vertical axis (i.e., $z-$axis) for the inner should be kept lesser than or equal to the outer ($c_{m,i} \leq c_{m,o}$). Moreover, it is also assumed that $\max(a_{m,q}, b_{m,q}, c_{m,q})$ is $a_{m,q}$. The semi-ellipsoids are rotatable around the vertical axes (i.e., $z-$axis) in the azimuth plane by an angle $\theta_{m,q}$. The AoA of the multipath waves received at an MS from different directions in azimuth and elevation planes are represented by ϕ_m and β_m, respectively. The MSs are located at certain points in the Cartesian coordinates system represented by (x_m, y_m, z_m). The generalized equation for any of these ellipsoids can be expressed as,

$$\frac{\left((x_{m,q} - x_m)\cos\theta_{m,q} + (y_{m,q} - y_m)\sin\theta_{m,q}\right)^2}{a_{m,q}^2}$$
$$+\frac{\left(-(x_{m,q} - x_m)\sin\theta_{m,q} + (y_{m,q} - y_m)\cos\theta_{m,q}\right)^2}{b_{m,q}^2}$$
$$+\frac{\left(z_{m,q} - z_m\right)^2}{c_{m,q}^2} = 1.$$

Eq (5.1)

The mobile stations MS_1 and MS_2 are separated by a distance d and are placed in the Cartesian coordinates system at the points (0, 0, 0) and (d, 0, 0), respectively. Transformations between spherical and cartesian coordinates systems can be expressed as,

$$x_1 = r_1\cos\phi_1\cos\beta_1, \ y_1 = r_1\cos\beta_1\sin\phi_1, \text{ and } z_1 = r_1\sin\beta_1$$
$$x_2 = x_1 + d, \ y_2 = y_1, \text{ and } z_2 = z_1.$$

The effective volume, V_{eff}, of the scattering region shown in Fig. 5.1, can be obtained by subtracting the volume of the inner semi-ellipsoid from the outer
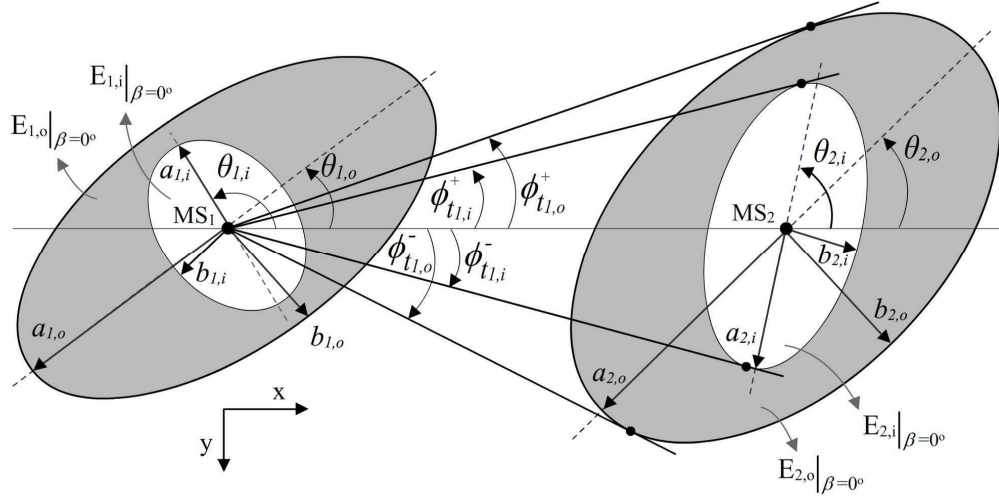
FIGURE 5.2: Top view of the proposed M2M scattering model.

semi-ellipsoid around both the mobile stations. Mathematically, this volume can be represented as,

$$V_{eff} = \frac{2\pi}{3}\Big[(a_{1,o}b_{1,o}c_{1,o} - a_{1,i}b_{1,i}c_{1,i}) + (a_{2,o}b_{2,o}c_{2,o} - a_{2,i}b_{2,i}c_{2,i})\Big]. \qquad Eq\ (5.2)$$

By observing arrival of the signals at the receiving mobile station say MS_1, the scattering region around the mobile stations is divided into three angular partitions, i.e., P_1, P_2 and P_3, as shown in Fig. 5.2. Angular limits for these partitions can be defined as,

$$\left.\begin{cases} \phi_{t,i}^- \leq \phi_1 \leq \phi_{t,i}^+ \\ \\ \qquad\text{or} \\ \\ 0 \leq \beta_1 \leq \beta_{t,i} \end{cases}\right\} \rightarrow P_1, \qquad Eq\ (5.3)$$

where, the symbol " $\rightarrow$ " shows the implication of a certain angular range to a name of partition based on certain conditions. Similarly,

71

$$\left.\begin{cases} \phi_{t,i}^+ < \phi_1 \le \phi_{t,o}^+ \\ \\ \text{or} \\ \\ \phi_{t,o}^- \le \phi_1 < \phi_{t,i}^- \\ \\ \text{or} \\ \\ \beta_{t,i} < \beta_1 \le \beta_{t,o} \end{cases}\right\} \to \mathrm{P}_2, \qquad\qquad Eq~(5.4)$$

and

$$\left.\begin{cases} \phi_{t,o}^+ < \phi_1 < \phi_{t,o}^- \\ \\ \text{or} \\ \\ \beta_{t,o} < \beta_1 \le \dfrac{\pi}{2} \end{cases}\right\} \to \mathrm{P}_3. \qquad\qquad Eq~(5.5)$$

The azimuth threshold angles, which separate these three partitions in azimuth plane, can be obtained as,

$$\phi_{t,q}^{\pm} = \begin{cases} \begin{aligned} &\arctan\left\{ \frac{1}{c_{2,q}^2 d^2 - \Psi\left(a_{2,q}^2 \cos^2\theta_{2,q} + b_{2,q}^2 \sin^2\theta_{2,q}\right)} \right.\\ &\qquad \times\left\{ \Psi(a_{2,q}^2 - b_{2,q}^2)\cos\theta_{2,q}\sin\theta_{2,q} \pm \left(b_{2,q}^2 c_{2,q}^2 d^2 \Psi \cos^2\theta_{2,q} \right.\right.\\ &\qquad\qquad\qquad \left.\left.\left. +a_{2,q}^2 d^2 c_{2,q}^2 \Psi \sin^2\theta_{2,q} - a_{2,q}^2 b_{2,q}^2 \Psi^2 \right)^{1/2} \right\} \right\}\\ &\qquad\qquad\qquad\qquad ;\quad \beta_1 < \arctan\left(\frac{c_{2,q}}{d}\right) \end{aligned}\\ \\ 0 \qquad\qquad\qquad\qquad\quad ;\quad \text{otherwise,} \end{cases}$$

$$Eq~(5.6)$$

where $\Psi = c_{2,q}^2 - d^2 \tan^2\beta_1$.

Similarly, the elevation threshold angle, $\beta_{t,q}$, shown in Fig. 5.3, is computed to separate the above-mentioned three partitions in elevation plane. The threshold
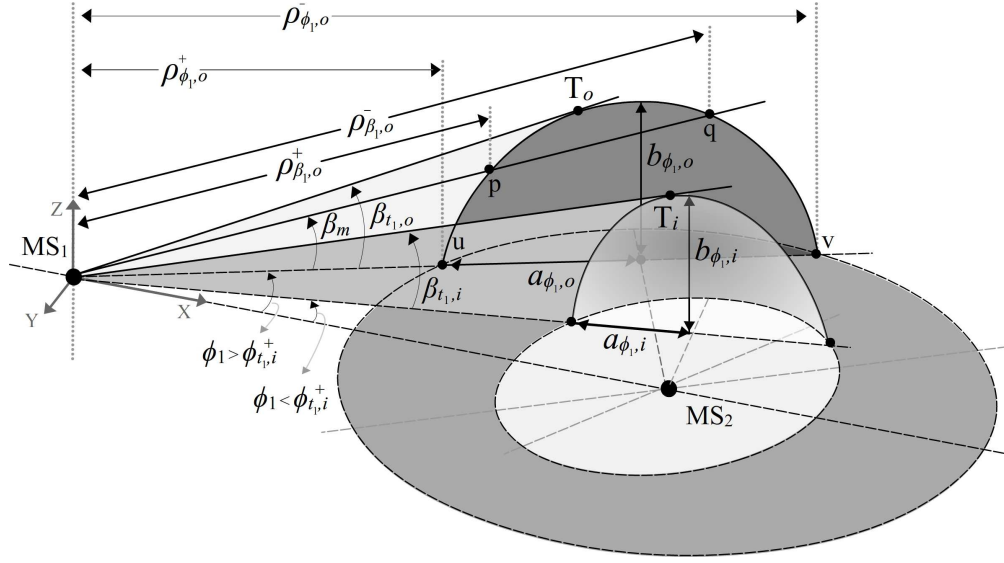
FIGURE 5.3: Cross-section of the hollow semi-ellipsoid around MS_2.

angle, $\beta_{t,i}$ and $\beta_{t,o}$, are the angles formed with the lines from MS_1 to the points tangent at the surface of inner and outer semi-ellipsoids at the points T_i and T_o, respectively. After tedious algebraic and trigonometric manipulation, the simplified form of derived expression for $\beta_{t,q}$ can be expressed as follows,

$$
\beta_{t,q} = \begin{cases} \arctan\left(\dfrac{2b_{\phi_q}}{\sqrt{(\rho_{\phi,q}^+ + \rho_{\phi,q}^-)^2 - 4a_{\phi,q}^2}}\right) & ; \ \phi_{t,q}^+\big|_{\beta_1=0^o} \leq \phi_1 \leq \phi_{t,q}^-\big|_{\beta_1=0^o} \\[4mm] 0 & ; \ \text{otherwise,} \end{cases}
$$

$$Eq\ (5.7)$$

where, the parameters $a_{\phi,q}$ and $b_{\phi,q}$ are the major and minor dimensions of vertical ellipses formed around MS_2 along the angular direction of observation from MS_1, (see Fig. 5.3). These parameters can be derived as,

$$
a_{\phi,q} = \frac{a_{2,q}b_{2,q}\sqrt{b_{2,q}^2\cos^2(\theta_{2,q}-\phi_1) + a_{2,q}^2\sin^2(\phi_1-\theta_{2,q}) - d^2\sin^2\phi_1}}{b_{2,q}^2\cos^2(\theta_{2,q}-\phi_1) + a_{2,q}^2\sin^2(\theta_{2,q}-\phi_1)}, \qquad Eq\ (5.8)
$$

73

and

$$b_{\phi,q} = \frac{1}{a_{2,q}b_{2,q}} \sqrt{a_{2,q}^2 b_{2,q}^2 c_{2,q}^2 - b_{2,q}^2 c_{2,q}^2 \Gamma_q^2 \cos^2(\theta_{2,q} + \Theta_q) - a_{2,q}^2 c_{2,q}^2 \Gamma_q^2 \sin^2(\theta_{2,q} + \Theta_q)},$$

$$Eq\ (5.9)$$

where,

$$\Theta_q = \arcsin\left(\frac{(\rho_{\phi,q}^+ + \rho_{\phi,q}^-) \sin \phi_1}{2\,\Gamma_q}\right),$$

and

$$\Gamma_q = \sqrt{d^2 + \frac{1}{4}\left(\rho_{\phi,q}^+ + \rho_{\phi,q}^-\right)^2 - d\left(\rho_{\phi,q}^+ + \rho_{\phi,q}^-\right) \cos \phi_1}.$$

The azimuthal distance from MS_1 to the intersection points u and v on the outer ellipse at ground plane around MS_2 are represented by $\rho_{\phi,o}^+$ and $\rho_{\phi,o}^-$, respectively (shown in Fig. 5.3). Similarly, the azimuthal distance from MS_1 to the intersection points on the inner ellipse at the ground around MS_2 are represented by $\rho_{\phi,i}^+$ and $\rho_{\phi,i}^-$. These distances can be expressed in generalized form as,

$$\rho_{\phi,q}^\pm = \begin{cases} \begin{aligned} &\frac{-1}{a_{2,q}^2 \sin^2(\phi_1 - \theta_{2,q}) + b_{2,q}^2 \cos^2(\phi_1 - \theta_{2,q})} \\ &\quad \times \Big\{ d\Big(a_{2,q}^2 \sin(\phi_1 - \theta_{2,q}) \sin \theta_{2,q} - b_{2,q}^2 \cos(\phi_1 - \theta_{2,q}) \cos \theta_{2,q}\Big) \\ &\quad\quad \pm a_{2,q}b_{2,q} \times \Big(a_{2,q}^2 \sin^2(\phi_1 - \theta_{2,q}) + b_{2,q}^2 \cos^2(\phi_1 - \theta_{2,q}) \\ &\quad\quad\quad\quad - d^2 \sin^2 \phi_1\Big)^{1/2}\Big\} \\ &\quad ;\ \ \phi_{t,q}^+\big|_{\beta_1=0^o} \leq \phi_1 \leq \phi_{t,q}^-\big|_{\beta_1=0^o} \\ 0 &\quad ;\ \ \text{otherwise.} \end{aligned} \end{cases}$$

$$Eq\ (5.10)$$

The parameter $r_{1,\max}$ represents the quantity of contributing scattering objects when observing in a particular direction. When the scattering objects are uniformly distributed, the amount of scattering objects in a particular direction can directly be obtained from the combined length of different segments, overlapped with the scattering region, of a line extended from an observing point (MS$_1$ or MS$_2$) to the farthest scattering object. The parameter $r_{1,\max}$ can be expressed for all the three angular partitions as shown below,

$$
r_{1,\max} = \begin{cases} (r_{1,o} - r_{1,i}) + (\rho_{\beta,o}^- - \rho_{\beta,o}^+) - (\rho_{\beta,i}^- - \rho_{\beta,i}^+) & ; \;\; \mathrm{P}_1 \\[2mm] (r_{1,o} - r_{1,i}) + (\rho_{\beta,o}^- - \rho_{\beta,o}^+) & ; \;\; \mathrm{P}_2 \\[2mm] r_{1,o} - r_{1,i} & ; \;\; \mathrm{P}_3, \end{cases} \qquad Eq\ (5.11)
$$

where, $r_{1,o}$ and $r_{1,i}$ are the radii of outer and inner semi-ellipsoids around MS$_1$ expressed as a function of azimuth and elevation angles, are given as,

$$
r_{1,q} = \frac{a_{1,q}\, b_{1,q}\, c_{1,q}}{\sqrt{\frac{1}{2} c_{1,q}^2 \cos^2 \beta_1 \left(a_{1,q}^2 + b_{1,q}^2 + (b_{1,q}^2 - a_{1,q}^2) \cos(2\theta_{1,q} - 2\phi_1) \right) + a_{1,q}^2 b_{1,q}^2 \sin^2 \beta_1}}.
$$
$$
Eq\ (5.12)
$$

The line segments from MS$_1$ to intersection points p and q at the surface of outer semi-ellipsoid around MS$_2$ are shown by $\rho_{\beta,o}^+$ and $\rho_{\beta,o}^-$, respectively (see Fig. 5.3). Similarly, the line segment from MS$_1$ to the intersections at the surface of inner semi-ellipsoid around MS$_2$ are represented by $\rho_{\beta,i}^+$ and $\rho_{\beta,i}^-$, respectively. After some mathematical and algebraic manipulation, these distances can be expressed

in generalized form, $\rho_{\beta,q}^{\pm}$, as follows,

$$
\rho_{\beta,q}^{\pm} = \begin{cases} \left(\dfrac{\rho_{\phi,q}^{+} + \rho_{\phi,q}^{-}}{2}\right)\sec\beta_1 - \dfrac{\sec\beta_1}{2(b_{\phi,q}^2 + a_{\phi,q}^2\tan^2\beta_1)} \times \left\{ (\rho_{\phi,q}^{+} + \rho_{\phi,q}^{-}) \right. \\ \qquad \left. a_{\phi,q}^2\tan^2\beta_1 \pm \sqrt{a_{\phi,q}^2 b_{\phi,q}^2\left(4b_{\phi,q}^2 + \left(4a_{\phi,q}^2 - (\rho_{\phi,q}^{+} + \rho_{\phi,q}^{-})^2\right)\tan^2\beta_1\right)} \right\} \\ \qquad\qquad\qquad ;\ \ \mathrm{P}_2 \\ 0 \qquad\qquad\qquad\ \ ;\ \ \mathrm{P}_1. \end{cases}
$$

Eq (5.13)

5.2 Angle-of-Arrival Statistics for the proposed scattering model

In this section, we derive expressions for the joint PDF of AoA in azimuth and elevation planes for the proposed generalized 3D channel model for M2M communication environment observed at both the ends of communication link. In Section 5.2.1, a detailed derivation of the PDF of AoA is presented and in Section 5.2.2, results of the PDF of AoA are discussed.

5.2.1 Derivation of PDF of AoA at MS_1

Consider, multipath signals arrive at MS_1 from MS_2 after striking at certain scattering object in particular azimuth and elevation angle. The amount of scatterers in a particular direction varies with the rotation of the inner and outer semi-ellipsoids. The joint PDF of AoA is a function of ϕ_1, β_1 and r_1, and can be found as,

$$
p(r_1, \phi_1, \beta_1) = \left. \frac{f(x_1, y_1, z_1)}{|J(x_1, y_1, z_1)|} \right|_{\substack{x_1 = r_1\cos\beta_1\cos\phi_1 \\ y_1 = r_1\cos\beta_1\sin\phi_1 \\ z_1 = r_1\sin\beta_1,}} \qquad Eq\ (5.14)
$$

where, the function $J(x_1, y_1, z_1)$ is the Jacobean transformation and given in simplified form as,

$$J(x_1, y_1, z_1) = \begin{vmatrix} \dfrac{\partial x_1}{\partial r_1} & \dfrac{\partial x_1}{\partial \phi_1} & \dfrac{\partial x_1}{\partial \beta_1} \\[2mm] \dfrac{\partial y_1}{\partial r_1} & \dfrac{\partial y_1}{\partial \phi_1} & \dfrac{\partial y_1}{\partial \beta_1} \\[2mm] \dfrac{\partial z_1}{\partial r_1} & \dfrac{\partial z_1}{\partial \phi_1} & \dfrac{\partial z_1}{\partial \beta_1} \end{vmatrix}^{-1} = \dfrac{1}{r_1^2 \cos \beta_1}, \qquad Eq~(5.15)$$

and the function $f(x_1, y_1, z_1)$ is the volume density and can be written as,

$$f(x_1, y_1, z_1) = \begin{cases} \dfrac{1}{V_{eff}} & ; \quad (x_1, y_1, z_1) \in (P_1 ~~ \text{or} ~~ P_2 ~~ \text{or} ~~ P_3) \\[3mm] 0 & ; \quad \text{otherwise.} \end{cases} \qquad Eq~(5.16)$$

The joint PDF of AoA can thus be obtained as,

$$p(r_1, \phi_1, \beta_1) = \dfrac{r_1^2 \cos \beta_1}{V_{eff}}. \qquad Eq~(5.17)$$

Integrating (5.17) over r_1 in the range from 0 to $r_{1,\max}$ in different partitions, we can get the joint PDF of AoA as,

$$p(\phi_1, \beta_1) = \begin{cases} \dfrac{\left(r_{1,o} - r_{1,i} + \rho_{\beta,o}^- - \rho_{\beta,o}^+ - \rho_{\beta,i}^- + \rho_{\beta,i}^+\right)^3 \cos \beta_1}{3V_{eff}} & ; ~ P_1 \\[4mm] \dfrac{\left(r_{1,o} - r_{1,i} + \rho_{\beta,o}^- - \rho_{\beta,o}^+\right)^3 \cos \beta_1}{3V_{eff}} & ; ~ P_2 \qquad Eq~(5.18) \\[4mm] \dfrac{\left(r_{1,o} - r_{1,i}\right)^3 \cos \beta_1}{3V_{eff}} & ; ~ P_3. \end{cases}$$

Marginal PDF of AoA in azimuth plane can be obtained by integrating (5.18) over β_1 as,

$$p(\phi_1) = \int\limits_{0}^{\beta_{t,i}} p(\phi_1, \beta_1)\Big|_{\mathrm{P}_1} \mathrm{d}\beta_1$$
$$+ \int\limits_{\beta_{t,i}}^{\beta_{t,o}} p(\phi_1, \beta_1)\Big|_{\mathrm{P}_2} \mathrm{d}\beta_1 + \int\limits_{\beta_{t,o}}^{\frac{\pi}{2}} p(\phi_1, \beta_1)\Big|_{\mathrm{P}_3} \mathrm{d}\beta_1.$$

Eq (5.19)

Similarly, marginal PDF of AoA in elevation plane can be found by integrating (5.18) over ϕ_1 as,

$$p(\beta_1) = \int\limits_{\phi_{t,i}^{-}}^{\phi_{t,i}^{+}} p(\phi_1, \beta_1)\Big|_{\mathrm{P}_1} \mathrm{d}\phi_1 + \int\limits_{\phi_{t,i}^{+}}^{\phi_{t,o}^{+}} p(\phi_1, \beta_1)\Big|_{\mathrm{P}_2} \mathrm{d}\phi_1$$
$$+ \int\limits_{\phi_{t,o}^{-}}^{\phi_{t,i}^{-}} p(\phi_1, \beta_1)\Big|_{\mathrm{P}_2} \mathrm{d}\phi_1 + \int\limits_{\phi_{t,o}^{+}}^{\phi_{t,o}^{-}} p(\phi_1, \beta_1)\Big|_{\mathrm{P}_3} \mathrm{d}\phi_1.$$

Eq (5.20)

It is important to mention that, by following the similar procedure, expressions for the joint PDF of AoA in azimuth and elevation planes observed at MS_2 can also be obtained by interchanging all the dimensions and parameters of MS_1 with MS_2.

5.2.2   Results and Discussion on Angle-of-Arrival

In this section, we discuss the obtained theoretical results and present plots that show the impact of channel parameters on the PDF of AoA. Trend of the obtained graphs is observed different for the different angular partitions given in (5.3), (5.4) and (5.5); therefore, the obtained results are discussed independently for these partitions in the following passages. The 3D plot of joint PDF of AoA w.r.t. azimuth and elevation angles is shown in Fig. 5.4(a). 2-D slices of the same plot
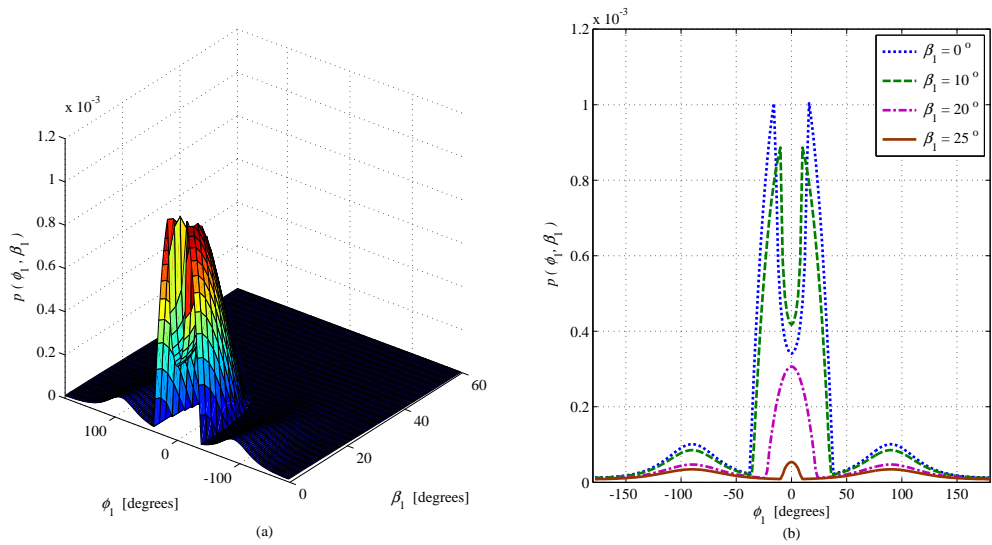
FIGURE 5.4: Joint PDF of AoA seen at MS_1, ($a_{1,o} = 65$m, $b_{1,o} = 40$m, $c_{1,o} = 30$m, $a_{1,i} = 25$m, $b_{1,i} = 20$m, $c_{1,i} = 20$m, $a_{2,o} = 55$m, $b_{2,o} = 35$m, $c_{2,o} = 30$m, $a_{2,i} = 20$m, $b_{2,i} = 15$m, $c_{2,i} = 15$m, $\theta_{1,o} = 0^o$, $\theta_{1,i} = 0^o$, $\theta_{2,o} = 0^o$, $\theta_{2,i} = 0^o$, $d = 100$).

for specific values of elevation angles are shown in Fig. 5.4(b); hence, the front slice of the joint PDF of AoA corresponds to its value at elevation angle of $\beta_1 = 0^o$. It is shown that the joint PDF of AoA decreases with an increase in the elevation angle (β_1) due to the reduction of scattering region's cross-section in the elevation plane.

For the partition P_1, the cavity in Fig. 5.4(a) or the U-shaped region in the plot of Fig. 5.4(b) indicates the hollow scatterer-free region in the semi-ellipsoid around MS_2. However, the hollow portion decreases as the elevation increases. The cavity in Fig. 5.4(a) or the U-shaped portion in Fig. 5.4(b) for the PDF of AoA disappears when β_1 increases from $\beta_{t,i}$, i.e., for the partitions other than the partition P_1.

If the elevation angle, β_1, is further increased beyond $\beta_{t,o}$ (i.e., partition P_3) then only those scatterers contribute in arrival of the signals which are confined within the semi-ellipsoids around MS_1. For the partition P_3, only the scatterers present in the vicinity of MS1 (i.e., receiver) correspond to the arrival of signal, therefore it has less probability of signal's arrival as compared to the partitions P_1 and P_2.
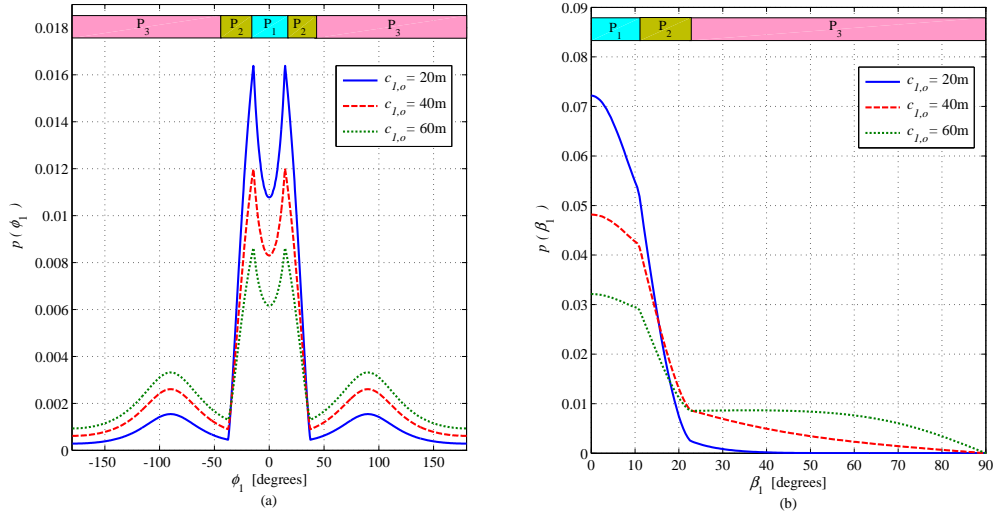
79

FIGURE 5.5: Effect of varying $c_{1,o}$ on the marginal PDF of AoA in (a) Azimuth plane, (b) Elevation Plane, ($a_{1,o} = 65$m, $b_{1,o} = 40$m, $a_{1,i} = 25$m, $b_{1,i} = 20$m, $c_{1,i} = 20$m, $a_{2,o} = 55$m, $b_{2,o} = 35$m, $c_{2,o} = 30$m, $a_{2,i} = 20$m, $b_{2,i} = 15$m, $c_{2,i} = 15$m, $\theta_{1,o} = 0^o$, $\theta_{1,i} = 0^o$, $\theta_{2,o} = 0^o$, $\theta_{2,i} = 0^o$, $d = 100$).

This shows that the scatterers in the elevation plane exert significant impact on the AoA statistics of the communication channel. Moreover, the impact of elevation angle is observed in [26], where the authors verified that signals in the elevation plane usually spread up to an angle 20°. Also, in [48], it is observed that 50% energy of the signal lie up to the elevation angle of 16°. As in streets and canyons, the M2M communication is usually NLoS scenario and the signals arrive at the MSs scattered from high rise buildings [46, 49]; therefore, we have developed a 3D geometrical scattering environment for M2M communication channels.

To elaborate the effect of scatterers in elevation plane in more detail, various plots are taken by varying the dimensions of the scattering region in elevation plane around both the ends of the M2M communication link. These plots are shown in Fig. 5.5, Fig. 5.6, Fig. 5.7 and Fig. 5.8. For convenience of the reader, numerical ranges of partitions P_1, P_2, and P_3 are indicated with colored labels in Fig. 5.5.

In Fig. 5.5, we show the effect of varying dimension of the outer semi-ellipsoid around MS_1 (i.e., receiver) along elevation axis on the marginal PDF of AoA in azimuth and elevation planes while keeping the other dimensions of the scattering
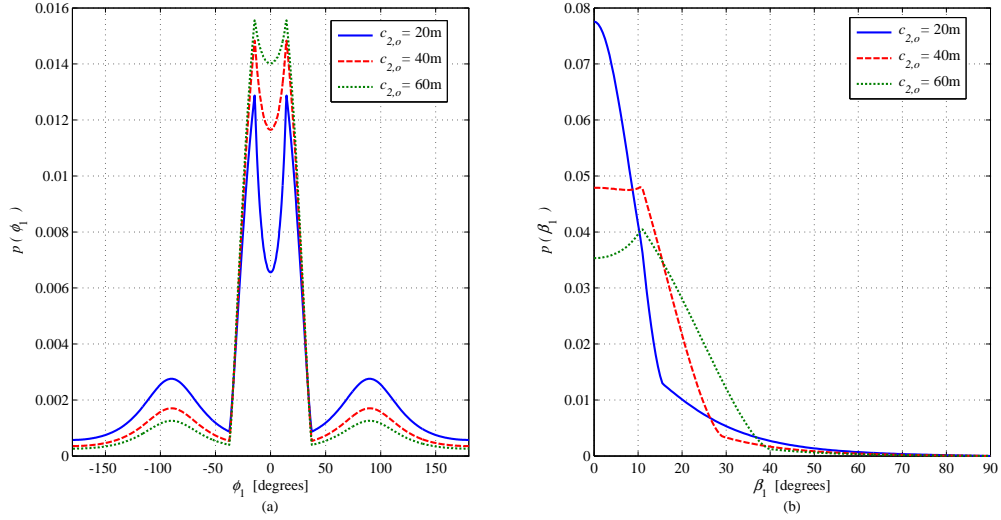
80

FIGURE 5.6: Effect of varying $c_{2,o}$ on the marginal PDF of AoA in (a) Azimuth plane, (b) Elevation plane, ($a_{1,o} = 65$m, $b_{1,o} = 40$m, $c_{1,o} = 30$m, $a_{1,i} = 25$m, $b_{1,i} = 20$m, $c_{1,i} = 20$m, $a_{2,o} = 55$m, $b_{2,o} = 35$m, $a_{2,i} = 20$m, $b_{2,i} = 15$m, $c_{2,i} = 15$m, $\theta_{1,o} = 0^o$, $\theta_{1,i} = 0^o$, $\theta_{2,o} = 0^o$, $\theta_{2,i} = 0^o$, $d = 100$).

region constant. It can be seen in Fig. 5.5(a) that the marginal PDF of AoA in azimuth plane in partition P_1 and P_2 for the angles around LoS direction decreases with an increase in $c_{1,o}$. Fig. 5.5(b) shows a similar trend for the PDF of AoA in elevation plane seen in Fig. 5.5(a) with increasing $c_{1,o}$. However, it exhibits an adverse trend in partition P_3.

In Fig. 5.6, we show the effect of varying the dimension of the outer semi-ellipsoid around MS_2 along the elevation axis on the marginal PDF of AoA observed at MS_1. We see that for higher values of $c_{2,o}$ in Fig. 5.6(a), the marginal PDF of AoA in azimuth plane is higher in partitions P_1 and P_2 and it is lower in partition P_3. The marginal PDF of AoA in elevation plane is shown in Fig. 5.6(b), which shows that the PDF is higher for lower values of $c_{2,o}$ in partitions P_1 and P_2 while opposite trend in P_3. Fig. 5.7(a) shows similar results as seen in Fig. 5.6(a) while in Fig. 5.8(b), it is observed that the marginal PDF of AoA in elevation plane is higher for higher values of $c_{2,i}$ for elevation angles in partitions P_1 and P_2 and converse in partition P_3. Furthermore, the effect of varying $c_{2,i}$ on the PDF of AoA in azimuth and elevation plane can be observed in Fig. 5.8(a and b).

81

FIGURE 5.7: Effect of varying $c_{1,i}$ on marginal the PDF of AoA in (a) Azimuth plane, (b) Elevation plane, ($a_{1,o} = 65$m, $b_{1,o} = 40$m, $c_{1,o} = 30$m, $a_{1,i} = 25$m, $b_{1,i} = 20$m, $a_{2,o} = 55$m, $b_{2,o} = 35$m, $c_{2,o} = 30$m, $a_{2,i} = 20$m, $b_{2,i} = 15$m, $c_{2,i} = 15$m, $\theta_{1,o} = 0^o$, $\theta_{1,i} = 0^o$, $\theta_{2,o} = 0^o$, $\theta_{2,i} = 0^o$, $d = 100$).

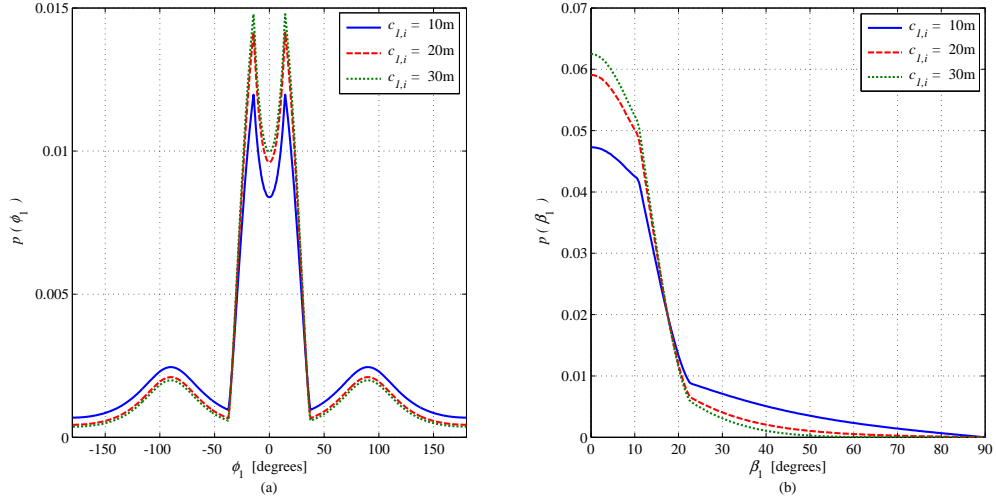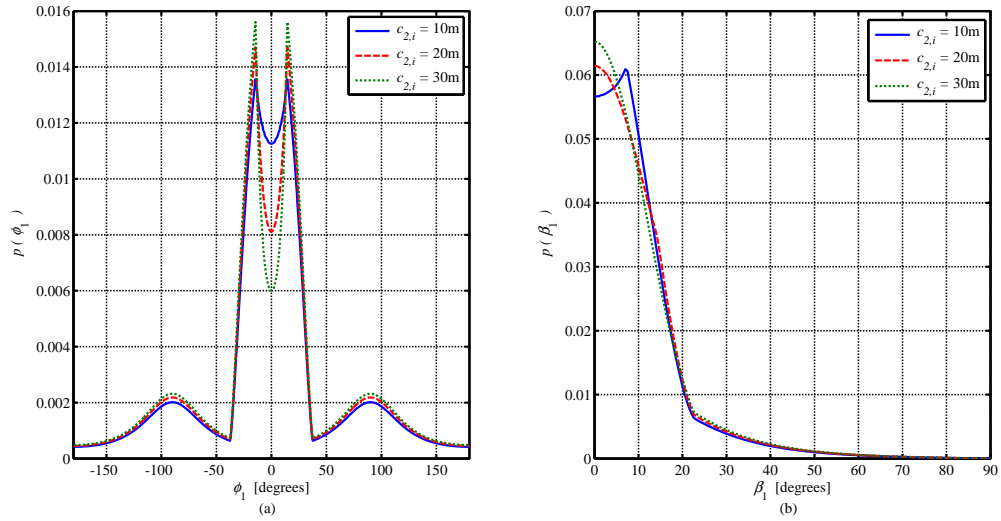FIGURE 5.8: Effect of varying $c_{2,i}$ on the marginal PDF of AoA in (a) Azimuth plane, (b) Elevation plane, ($a_{1,o} = 65$m, $b_{1,o} = 40$m, $c_{1,o} = 30$m, $a_{1,i} = 25$m, $b_{1,i} = 20$m, $c_{1,i} = 20$m, $a_{2,o} = 55$m, $b_{2,o} = 35$m, $c_{2,o} = 30$m, $a_{2,i} = 20$m, $b_{2,i} = 15$m, $\theta_{1,o} = 0^o$, $\theta_{1,i} = 0^o$, $\theta_{2,o} = 0^o$, $\theta_{2,i} = 0^o$, $d = 100$).
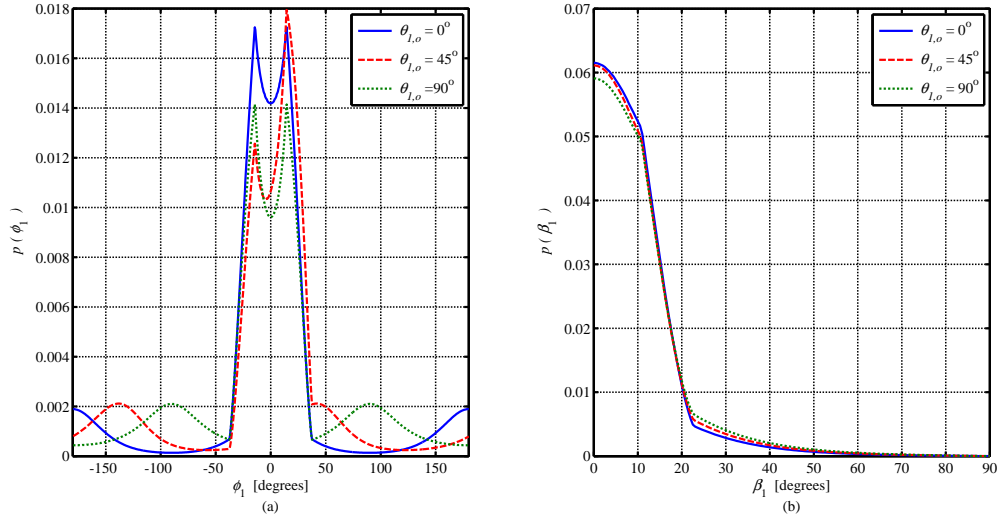
FIGURE 5.9: Effect of rotation w.r.t. $\theta_{1,o}$ on the marginal PDF of AoA in (a) Azimuth plane, (b) Elevation plane, ($a_{1,o} = 65$m, $b_{1,o} = 40$m, $c_{1,o} = 30$m, $a_{1,i} = 25$m, $b_{1,i} = 20$m, $c_{1,i} = 20$m, $a_{2,o} = 55$m, $b_{2,o} = 35$m, $c_{2,o} = 30$m, $a_{2,i} = 20$m, $b_{2,i} = 15$m, $c_{2,i} = 15$m, $\theta_{1,i} = 0^o$, $\theta_{2,o} = 0^o$, $\theta_{2,i} = 0^o$, $d = 100$).

The effect of rotating the inner and outer semi-ellipsoids around MS_1 and MS_2 about their vertical axes are shown Fig. 5.9, 5.10, 5.11, and 5.12. It can be observed that, the rotation of any of the semi-ellipsoids do not have a significant impact on the PDF of AoA in the elevation plane; however, it has considerable impact on the results for azimuthal plane. Next we show the effect of hollowness of the scattering region around MS_2 on the marginal PDF of AoA in azimuth and elevation planes by keeping the outer dimensions of the semi-ellipsoids constant. The PDF of AoA in azimuth and elevation planes is shown in Fig. 5.13, to elaborate the impact of hollowness, the dimensions of the inner and outer ellipsoids are kept symmetrical in all dimensions, i.e., spherical shaped regions.

The high-rise buildings or structures set the orientations and dimensions of the streets, canyons and street crossings. These dimensions and orientations are then modeled by the major and minor axes of the hollow semi-ellipsoids as the physical channel models of both mobile stations. The model parameters would thus be changed if the orientation or dimension of the street or canyon changes.

It is pertinent to mention that the complexity of all 3D scattering models including

FIGURE 5.10: Effect of rotation w.r.t. $\theta_{2,o}$ on the marginal PDF of AoA in (a) Azimuth plane, (b) Elevation plane, ($a_{1,o} = 65$m, $b_{1,o} = 40$m, $c_{1,o} = 30$m, $a_{1,i} = 25$m, $b_{1,i} = 20$m, $c_{1,i} = 20$m, $a_{2,o} = 55$m, $b_{2,o} = 35$m, $c_{2,o} = 30$m, $a_{2,i} = 20$m, $b_{2,i} = 15$m, $c_{2,i} = 15$m, $\theta_{1,o} = 0^o$, $\theta_{1,i} = 0^o$, $\theta_{2,i} = 0^o$, $d = 100$).
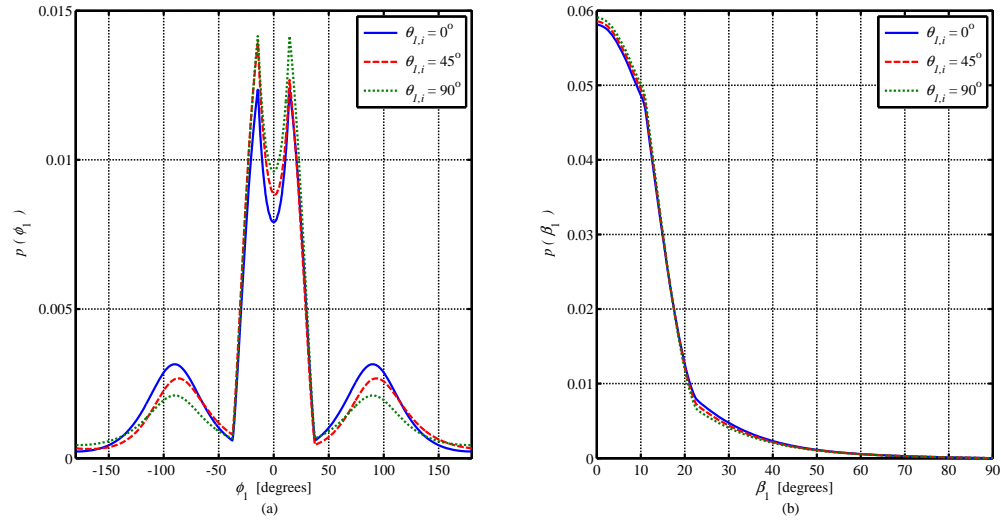
FIGURE 5.11: Effect of rotation w.r.t. $\theta_{1,i}$ on the marginal PDF of AoA in (a) Azimuth plane, (b) Elevation plane, ($a_{1,o} = 65$m, $b_{1,o} = 40$m, $c_{1,o} = 30$m, $a_{1,i} = 25$m, $b_{1,i} = 20$m, $c_{1,i} = 20$m, $a_{2,o} = 55$m, $b_{2,o} = 35$m, $c_{2,o} = 30$m, $a_{2,i} = 20$m, $b_{2,i} = 15$m, $c_{2,i} = 15$m, $\theta_{1,o} = 0^o$, $\theta_{2,o} = 0^o$, $\theta_{2,i} = 0^o$, $d = 100$).
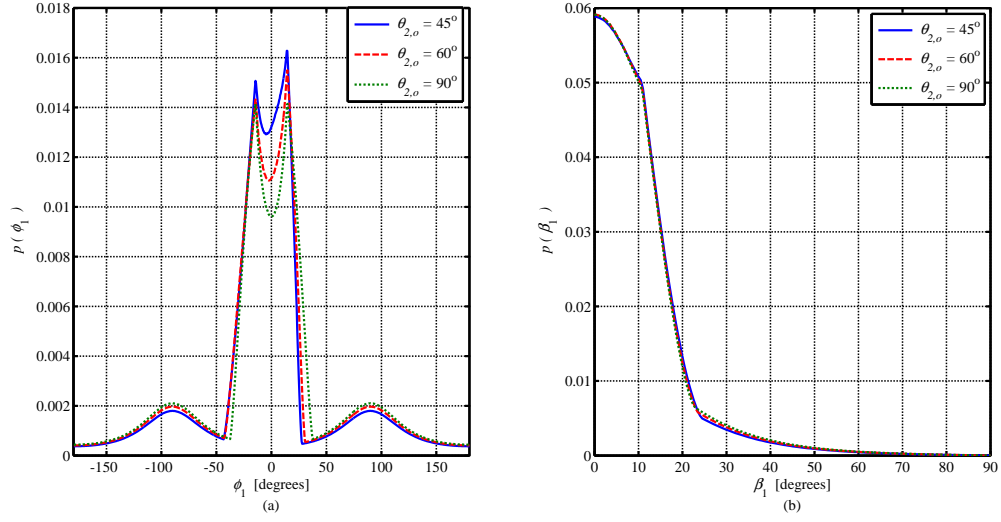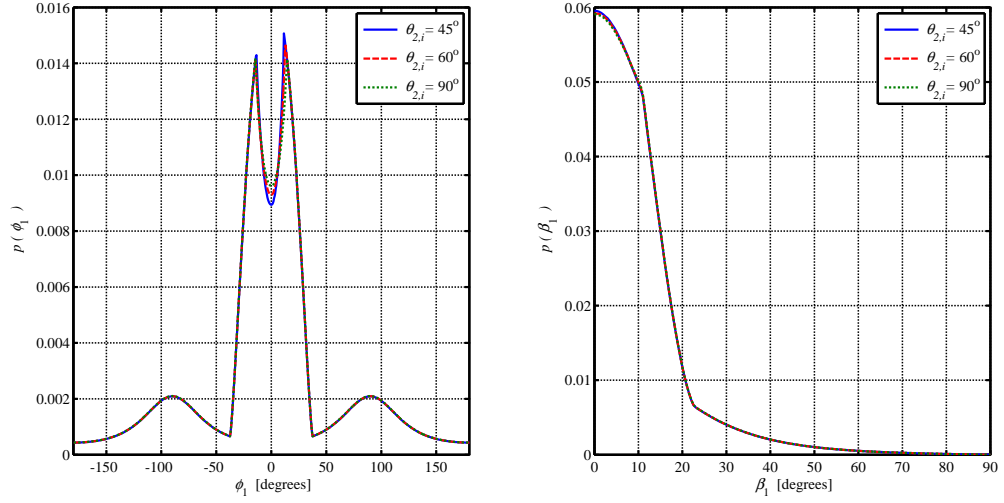
FIGURE 5.12: Effect of rotation w.r.t. $\theta_{2,i}$ on the marginal PDF of AoA in (a) Azimuth plane, (b) Elevation plane, ($a_{1,o} = 65$m, $b_{1,o} = 40$m, $c_{1,o} = 30$m, $a_{1,i} = 25$m, $b_{1,i} = 20$m, $c_{1,i} = 20$m, $a_{2,o} = 55$m, $b_{2,o} = 35$m, $c_{2,o} = 30$m, $a_{2,i} = 20$m, $b_{2,i} = 15$m, $c_{2,i} = 15$m, $\theta_{1,o} = 0^o$, $\theta_{1,i} = 0^o$, $\theta_{2,o} = 0^o$, $d = 100$).
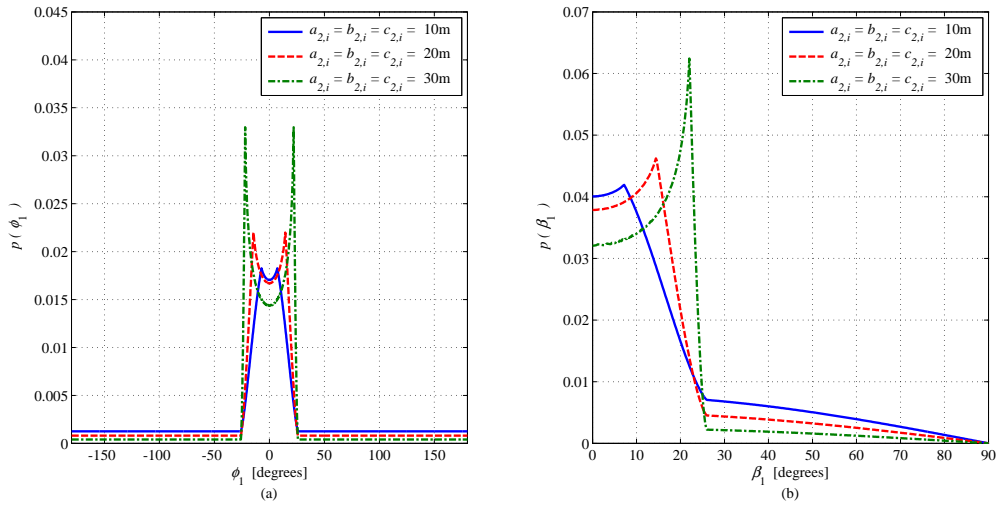

FIGURE 5.13: Effect of hollowness on the marginal PDF of AoA in (a) Azimuth plane, (b) Elevation plane, ($a_{1,o} = 65$m, $b_{1,o} = 40$m, $c_{1,o} = 30$m, $a_{2,o} = 55$m, $b_{2,o} = 35$m, $c_{2,o} = 30$m, $a_{2,i} = 20$m, $b_{2,i} = 15$m, $c_{2,i} = 15$m, $\theta_{1,o} = 0^o$, $\theta_{1,i} = 0^o$, $\theta_{2,o} = 0^o$, $\theta_{2,i} = 0^o$, $d = 100$).

the proposed generalized scattering model is higher than that of the 2D scattering models. This is due to the fact that the 3D scattering models take elevation of the BS or the scatterers into account. With an increased complexity, the proposed model, therefore becomes one such model that has the ability to model a large number of communication scenarios listed in Table 1 with a slight change in some of its parameters. In other words, instead of using many models to simulate or model particular communication scenarios separately, it is more viable to use the proposed generalized model that provides a unified approach applied to all such scenarios.

5.3 Time-of-Arrival Statistics for the proposed model

5.3.1 Derivation of PDF of ToA

In this section, we derive the PDF of ToA for the proposed 3D channel model. As we consider single-bounce scattering model, the propagation time-delay τ of the multipath signal from the transmitting mobile station, after striking with any of the scatterers reaching the receiving mobile station can be found as,

$$\tau = \frac{r_{1,s} + r_{2,s}}{c}, \qquad\qquad Eq\ (5.21)$$

where $r_{1,s}$ and $r_{2,s}$ are the distances of a particular scattering object from MS_1 and MS_2, respectively, as shown in Fig. 5.2 and c is the speed of electromagnetic waves. LoS component (if existed) of the signal is supposed to exhibit the minimum propagation delay, $\tau_{\min}$, and can be found as,

$$\tau_{\min} = \frac{d}{c}. \qquad\qquad Eq\ (5.22)$$

As we have assumed that $\max(a_{m,q}, b_{m,q}, c_{m,q})$ is $a_{m,q}$, which implies that the number of scatterers in the azimuth plane are greater than that in the elevation plane, therefore, maximum propagation path delay can be found as follows,

$$\tau_{\max} = \begin{cases} \dfrac{1}{c}\left(a_{1,o} + \sqrt{a_{1,o}^2 + d^2 + 2\,a_{1,o}\,d\,\cos\theta_{1,o}}\,\right) & ;\ a_{1,o} > a_{2,o} \text{ and } 0 < \theta_{1,o} \le \pi/2 \\[2ex] \dfrac{1}{c}\left(a_{1,o} + \sqrt{a_{1,o}^2 + d^2 - 2\,a_{1,o}\,d\,\cos\theta_{1,o}}\,\right) & ;\ a_{1,o} > a_{2,o} \text{ and } \pi/2 < \theta_{1,o} \le \pi \\[2ex] \dfrac{1}{c}\left(a_{2,o} + \sqrt{a_{2,o}^2 + d^2 + 2\,a_{2,o}\,d\,\cos\theta_{2,o}}\,\right) & ;\ a_{1,o} < a_{2,o} \text{ and } 0 < \theta_{2,o} \le \pi/2 \\[2ex] \dfrac{1}{c}\left(a_{2,o} + \sqrt{a_{2,o}^2 + d^2 - 2\,a_{2,o}\,d\,\cos\theta_{2,o}}\,\right) & ;\ a_{1,o} < a_{2,o} \text{ and } \pi/2 < \theta_{2,o} \le \pi. \end{cases}$$

$$Eq\ (5.23)$$

The scattering region already divided into three partitions as given in (5.3), (5.4) and (5.5), can be further explained on the basis of propagation delay for the smallest and largest propagation paths in a particular direction of arrival. These limits along with their corresponding partitions can be obtained as,

$$\tau_{l,\min}(\phi_1, \beta_1) = \frac{1}{c}\left\{ r_{1,i} + \sqrt{r_{1,i}^2 + d^2 - 2\,d\,r_{1,i}\,\cos\phi_1\cos\beta_1}\,\right\} \qquad Eq\ (5.24)$$

and

$$\tau_{l,\max}(\phi_1, \beta_1) = \begin{cases} \dfrac{\rho_{\beta,o}^- + \sqrt{{\rho_{\beta,o}^-}^2 + d - 2\,d\,\rho_{\beta,o}^-\,\cos\phi_1\cos\beta_1}}{c} & ;\mathrm{P}_1 \ \text{ or } \ \mathrm{P}_2 \\[3ex] \dfrac{r_{1,o} + \sqrt{r_{1,o}^2 + d^2 - 2\,d\,r_{1,o}\cos\phi_1\,\cos\beta_1}}{c} & ;\mathrm{P}_3. \end{cases}$$

$$Eq\ (5.25)$$

Distance of a particular scatterer from MS_2 in terms of azimuth and elevation angles is,

$$r_{2,s} = \sqrt{r_{1,s}^2 + d^2 - 2dr_{1,s}\cos\beta_1\cos\phi_1}, \qquad Eq\ (5.26)$$

by substituting (5.26) in (5.21), an expression for $r_{1,s}$ can be obtained as,

$$r_{1,s} = \frac{c^2\tau^2 - d^2}{2(c\tau - d\cos\beta_1\cos\phi_1)}. \qquad Eq\ (5.27)$$

The joint trivariate function for PDF of ToA and AoA can be obtained as in [27],

$$p(\tau, \phi_1, \beta_1) = \frac{p(r_{1,s}, \phi_1, \beta_1)}{|J(r_{1,s}, \phi_1, \beta_1)|}, \qquad Eq\ (5.28)$$

where, $p(r_{1,s}, \phi_1, \beta_1)$ is the joint probability density function of AoA observed at MS_1 given in (5.17), shown as under,

$$p(r_{1,s}, \phi_1, \beta_1) = \frac{r_{1,s}^2\cos\beta_1}{V_{eff}}. \qquad Eq\ (5.29)$$

The Jacobean Transformation in (5.28) can be found as,

$$J(r_{1,s}, \phi_1, \beta_1) = \left|\frac{\partial r_{m1}}{\partial\tau}\right|^{-1} = \frac{2(d\cos\beta_1\cos\phi_1 - c\tau)^2}{c(d^2 + c^2\tau^2 - 2c\tau d\cos\beta_1\cos\phi_1)}, \qquad Eq\ (5.30)$$

substituting (5.29) and (5.30) in (5.28), we get the joint trivariate density function of the temporal and spatial characteristics of multipath signals in M2M environment as,

$$p(\tau, \phi_1, \beta_1) = \frac{c(d^2 - c^2\tau^2)^2(c^2\tau^2 + d^2 - 2c\tau\cos\phi_1\cos\beta_1)\cos\beta_1}{8\,V_{eff}\,(d\cos\beta_1\cos\phi_1 - c\tau)^4}. \qquad Eq\ (5.31)$$

By integrating (5.31) over β_1, the joint PDF of ToA and AoA in azimuth plane can be obtained,

$$p(\tau, \phi_1) = \int\limits_0^{\pi/2} p(\tau, \phi_1, \beta_1) \, d\beta_1, \qquad\qquad Eq\ (5.32)$$

similarly, the joint PDF of ToA and AoA in elevation can be obtained by integrating (5.31) over ϕ_1

$$p(\tau, \beta_1) = \int\limits_{-\pi}^{\pi} p(\tau, \phi_1, \beta_1) \, d\phi_1. \qquad\qquad Eq\ (5.33)$$

Finally, the marginal PDF of ToA can be obtained by integrating (5.31) over azimuth and elevation angles, as follow,

$$p(\tau) = \int\limits_{-\pi}^{\pi} \int\limits_0^{\pi/2} p(\tau, \phi_1, \beta_1) d\beta_1 \, d\phi_1. \qquad\qquad Eq\ (5.34)$$

5.3.2   Results and Discussion on Time-of-Arrival

In this section, we present the discussion and observations on the obtained theoretical results of the PDF of ToA and AoA. Joint PDF of ToA and azimuth AoA in 3D plots are shown in Fig. 5.14(a) and Fig. 5.15(a). These figures show that for minimum propagation delay τ_{min}, the joint PDF of ToA and AoA in partition P_1 (i.e., the angles around LoS direction) is maximum and goes on decreasing as moving away from the LoS direction till partition P_2. Fig. 5.14 in comparison to Fig. 5.15, are shown to demonstrate the impact of varying the dimension of inner semi-ellipsoid along elevation axis around both the ends of communication link. Moreover, to elaborate the effects on the PDF of AoA in azimuth plane, 2D plots are provided in Fig. 5.14(b) and Fig. 5.15(b). Similarly, joint PDF of ToA and elevation AoA is shown in Fig. 5.16. It is seen that PDF of ToA in the angles around LoS direction (i.e., partition P_1) is higher for the signals with least delay. For any specific value of the τ, as the elevation angle (i.e., β_1) increases from 0°
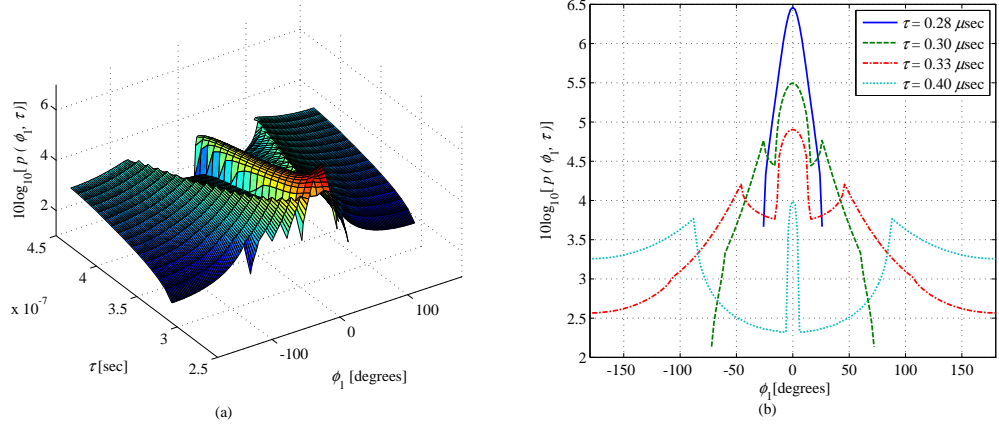
FIGURE 5.14: Joint PDF of ToA and AoA w.r.t. ϕ_1, ($a_{1,o} = 50$m, $b_{1,o} = 40$m, $c_{1,o} = 40$m, $a_{1,i} = 20$m, $b_{1,i} = 16$m, $c_{1,i} = 10$m, $a_{2,o} = 25$m, $b_{2,o} = 20$m, $c_{2,o} = 15$m, $a_{2,i} = 18$m, $b_{2,i} = 15$m, $c_{2,i} = 10$m, $\theta_{1,o} = 0^o, \theta_{1,i} = 0^o, \theta_{2,o} = 0^o, \theta_{2,i} = 0^o$, and $d = 100$m).
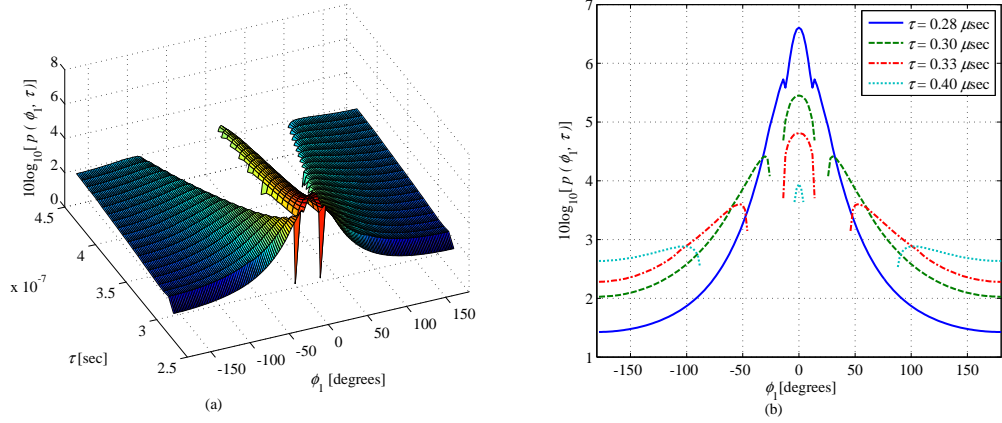
FIGURE 5.15: Joint PDF of ToA and AoA w.r.t. ϕ_1, ($a_{1,o} = 50$m, $b_{1,o} = 40$m, $c_{1,o} = 5$m, $a_{1,i} = 20$m, $b_{1,i} = 16$m, $c_{1,i} = 1$m, $a_{2,o} = 25$m, $b_{2,o} = 20$m, $c_{2,o} = 3$m, $a_{2,i} = 18$m, $b_{2,i} = 15$m, $c_{2,i} = 1$m, $\theta_{1,o} = 0^o, \theta_{1,i} = 0^o, \theta_{2,o} = 0^o, \theta_{2,i} = 0^o$, and $d = 100$m).

to 90°, the number of scatterers decreases as a result the PDF decreases. In Fig. 5.17, the marginal PDF of ToA is shown for different values of the parameters of scattering region in elevation axis. The obtained theoretical results demonstrate the importance of including elevation plane while modeling the scattering region. Therefore, it can be concluded that the scattering region should be modeled in 3D to obtain more realistic results.

As far as the frequency-selective behavior is concerned, multipath delays longer
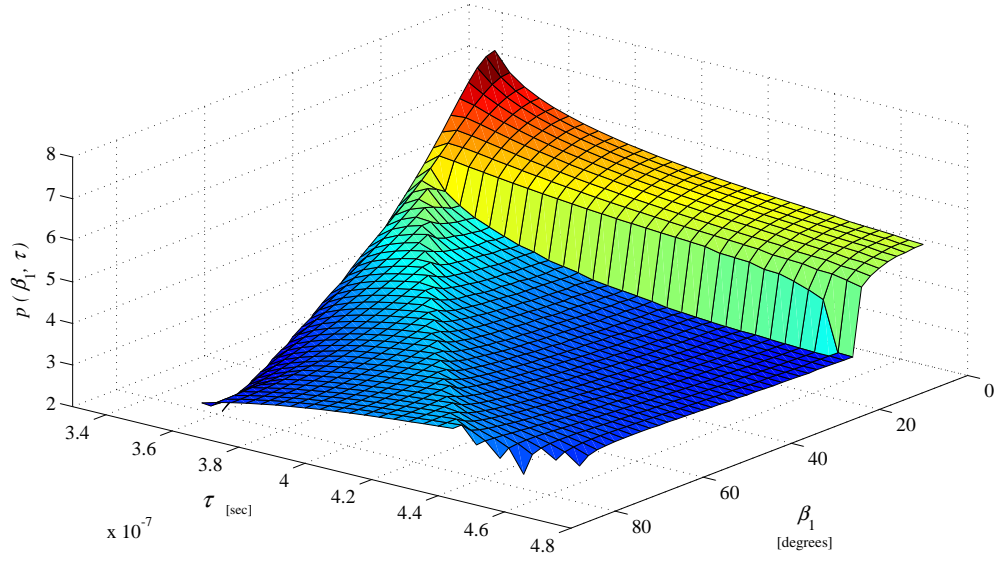
FIGURE 5.16: Joint PDF of ToA and AoA w.r.t. β_1, ($a_{1,o} = 50$m, $b_{1,o} = 40$m, $c_{1,o} = 5$m, $a_{1,i} = 20$m, $b_{1,i} = 16$m, $c_{1,i} = 1$m, $a_{2,o} = 25$m, $b_{2,o} = 20$m, $c_{2,o} = 3$m, $a_{2,i} = 18$m, $b_{2,i} = 15$m, $c_{2,i} = 1$m, $\theta_{1,o} = 0^o, \theta_{1,i} = 0^o, \theta_{2,o} = 0^o, \theta_{2,i} = 0^o$, and $d = 100$m).
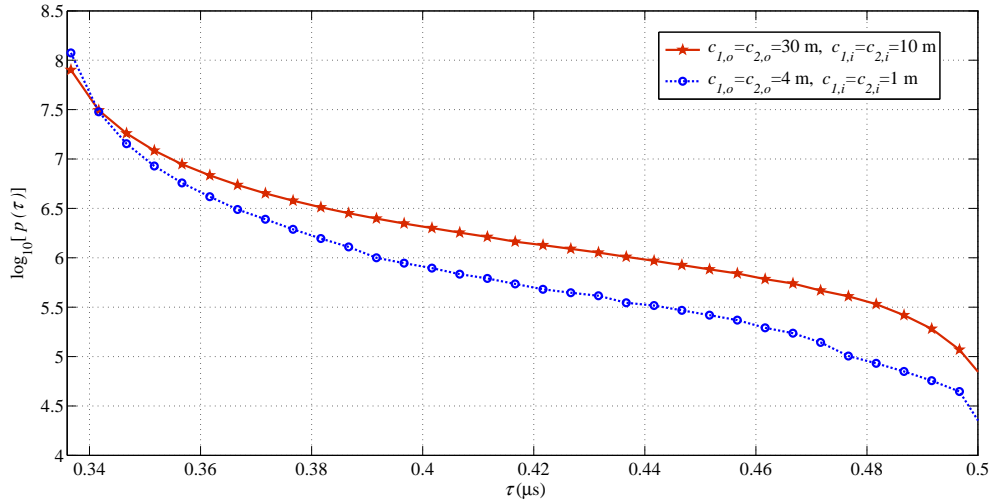
FIGURE 5.17: Effect of elevation on the joint PDF of ToA, ($a_{1,o} = 50$m, $b_{1,o} = 40$m, $a_{1,i} = 20$m, $b_{1,i} = 16$m, $a_{2,o} = 25$m, $b_{2,o} = 20$m, $a_{2,i} = 18$m, $b_{2,i} = 15$m, $\theta_{1,o} = 0^o, \theta_{1,i} = 0^o, \theta_{2,o} = 0^o, \theta_{2,i} = 0^o$, and $d = 100$m).

than the signal duration will cause severe frequency-selective fading at the receiver [55]. In our proposed model, multipaths delays depend on the major and minor axes of the outer and inner semi-ellipsoids. Considering a single-bounce reflection, the scattering objects that are associated with a particular path length are located on a semi-ellipsoid with MS_1 and MS_2 located at its focal points as shown in Fig. 5.18. Frequency-selective channels have scatterers that are located on several semi-ellipsoids around the mobile stations that correspond to different delays and that are significant compared to a symbol duration. In M2M communication environment, these scatterers usually correspond to high-rise buildings or trees. Since it is assumed in the proposed model that the length of the major axis is always greater than both of the minor axis and height of the semi-ellipsoid. Therefore, the longest delay that usually sets the coherence bandwidth of the physical propagation environment will result from the scattering phenomena along the major axis. Hence, the frequency-selective behavior of the proposed scattering model depends on the dimensions of its hollow semi-ellipsoid, adjusted on the basis of the realistic mobile-to-mobile propagation environment.
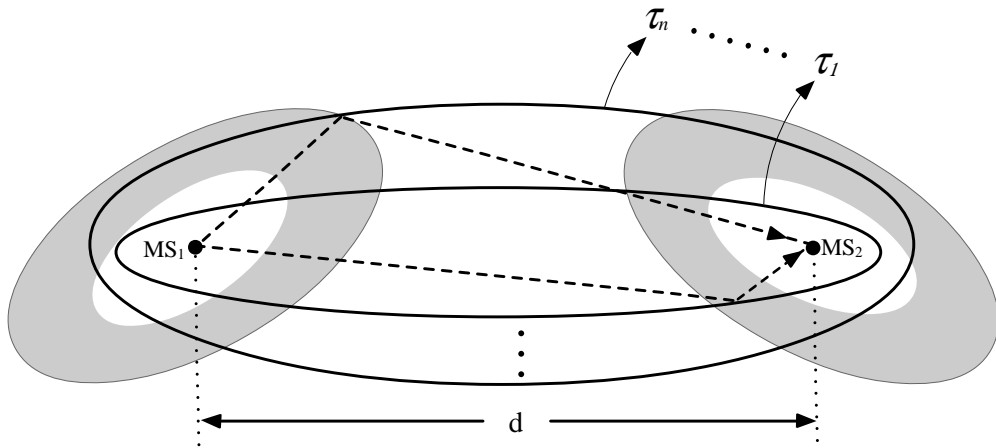

FIGURE 5.18: Top view of the geometrical representation of multipath fading channels for different delays.
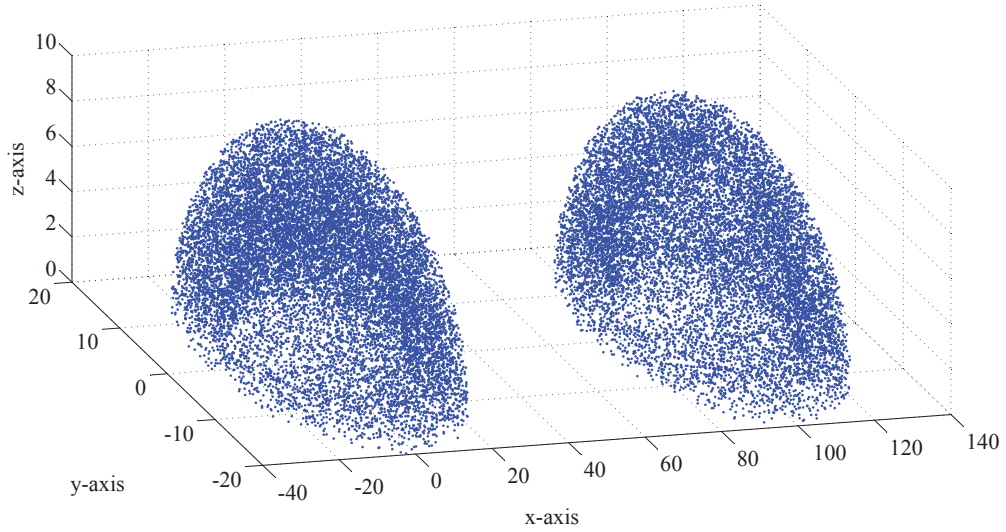
FIGURE 5.19: Spatial distribution of scattering objects, ($a_{1,o} = 50$m, $b_{1,o} = 40$m, $a_{1,i} = 20$m, $b_{1,i} = 16$m, $a_{2,o} = 25$m, $b_{2,o} = 20$m, $a_{2,i} = 18$m, $b_{2,i} = 15$m, $\theta_{1,o} = 0^o, \theta_{1,i} = 0^o, \theta_{2,o} = 0^o, \theta_{2,i} = 0^o$, and $d = 100$m).

5.4 Model Validation and Generalization

In this section, the validation of our proposed geometrical channel model through comparison with simulation results is presented. For this purpose, scatterers are created as point objects in such a way that they are uniformly distributed in the defined regions with specific orientations and sizes specific scenario as given in Fig. 5.19. The model parameters are shown in the caption of the figure.

Using the simulations setup, angles of arrival in azimuth and elevation planes are recorded and their respective PDFs are calculated. These PDFs are plotted and compared with the analytical results in Fig. 5.20. For 10^6 scattering points, an excellent agreement is seen between simulation results and analytical curves.

Similarly, analytical curves for the marginal PDF of ToA in M2M communication environment is also compared with the simulation results as shown in Fig. 5.21. It can be seen that simulation results perfectly match the analytical results for 10^6 scattering points for the model parameters given in the caption of the figure;
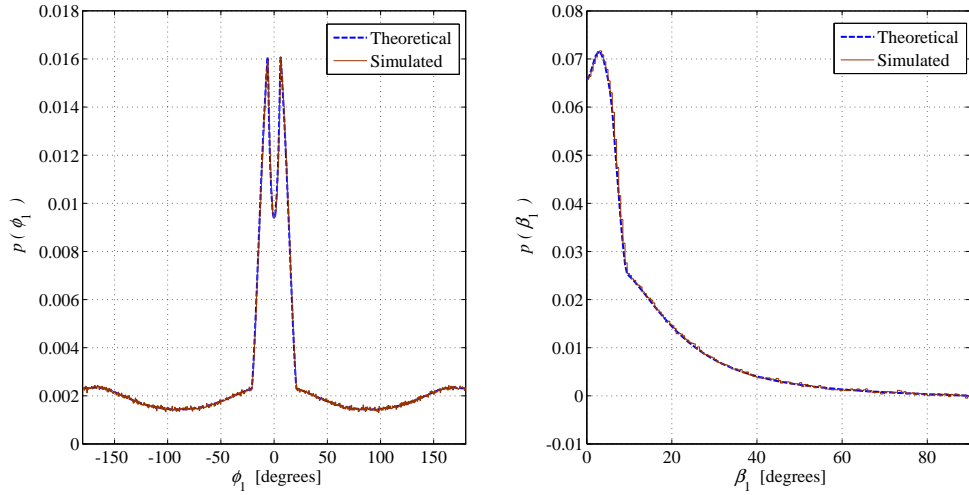
FIGURE 5.20: Simulation results and analytical marginal PDF of AoA curves in (a) Azimuth plane, (b) Elevation plane, ($a_{1,o} = 65$m, $b_{1,o} = 40$m, $c_{1,o} = 30$m, $a_{1,i} = 25$m, $b_{1,i} = 20$m, $a_{2,o} = 55$m, $b_{2,o} = 35$m, $c_{2,o} = 30$m, $a_{2,i} = 20$m, $b_{2,i} = 15$m, $c_{2,i} = 15$m, $\theta_{1,o} = 0^o$, $\theta_{1,i} = 0^o$, $\theta_{2,o} = 0^o$, $\theta_{2,i} = 0^o$, $d = 100$).

however, for larger scattering object sizes with less number, the simulated results may exhibit slight roughness with no deviation from the major trend.

Moreover, the proposed model is also validated by comparing its results with those reported in measurement campaigns for different channel scenarios available in the literature [16-20]. It is important to note that our model is a generalized one, by substituting all the dimensions of the semi-ellipsoid around MS_1 and inner semi-ellipsoid around MS_2 equal to zero, our model deduces for F2M macrocellular environment. For this specific scenario, a comparison of obtained analytical results with those in [20] is shown in Fig. 21.

Moreover, the proposed model is also validated by comparing its results with those reported in measurement campaigns for different channel scenarios available in the literature [3, 56–59]. It is important to note that our model is a generalized one, by substituting all the dimensions of the semi-ellipsoid around MS_1 and inner semi-ellipsoid around MS_2 equal to zero, our model deduces for F2M macrocellular environment. For this specific scenario, a comparison of obtained analytical results with those in [3] is shown in Fig. 5.22.

94
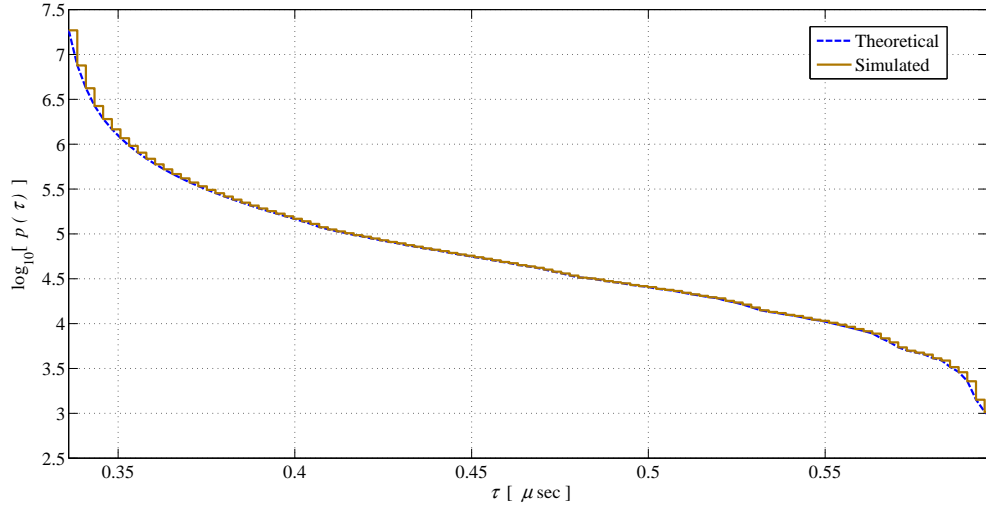
FIGURE 5.21: Simulation results and analytical marginal PDF of ToA curves, ($a_{1,o} = 50$m, $b_{1,o} = 40$m, $a_{1,i} = 20$m, $b_{1,i} = 16$m, $a_{2,o} = 25$m, $b_{2,o} = 20$m, $a_{2,i} = 18$m, $b_{2,i} = 15$m, $\theta_{1,o} = 0^o$, $\theta_{1,i} = 0^o$, $\theta_{2,o} = 0^o$, $\theta_{2,i} = 0^o$, and $d = 100$m).
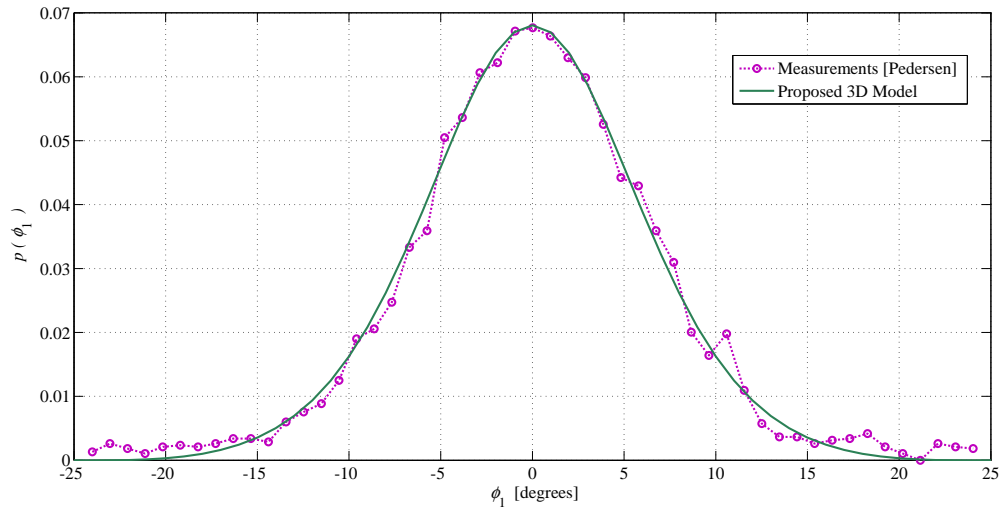
FIGURE 5.22: Marginal PDF of azimuth AoA observed at MS_1 for the proposed model in comparison with experimentally measured data in [3], ($a_{1,i} = b_{1,i} = c_{1,i} = 0$, $a_{2,i} = b_{2,i} = c_{2,i} = 0$ $a_{1,o} = b_{1,o} = c_{1,o} = 0$, $a_{2,o} = 70$m, $b_{2,o} = 20$m, $c_{2,o} = 15$m, $\theta_{1,o} = 0^o$, $\theta_{1,i} = 0^o$, $\theta_{2,o} = 0^o$, $\theta_{2,i} = 0^o$, $d = 100$)
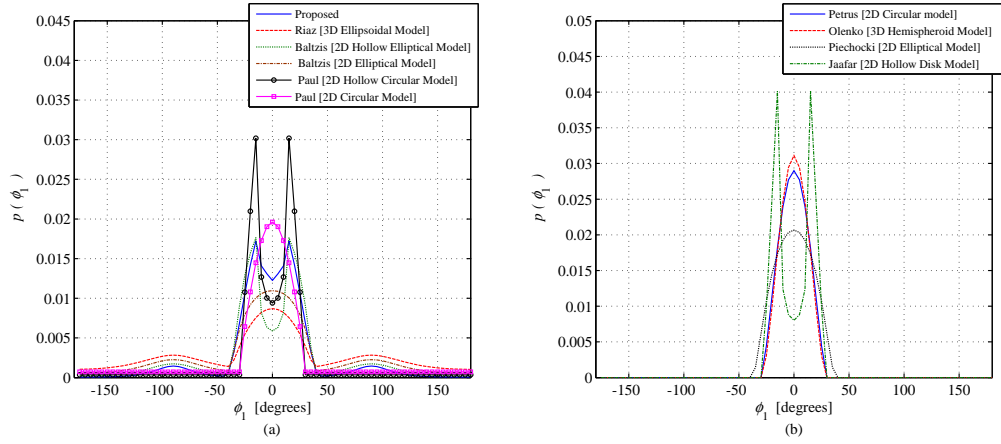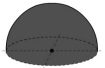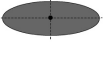
FIGURE 5.23: Comparison of the marginal PDF of AoA in azimuth plane of the proposed model with the existing (a) M2M Models, (b) F2M Models, ($a_{1,o} = 65$m, $b_{1,o} = 40$m, $c_{1,o} = 30$m, $a_{1,i} = 25$m, $b_{1,i} = 20$m, $c_{1,i} = 20$m, $a_{2,o} = 55$m, $b_{2,o} = 35$m, $c_{2,o} = 30$m, $a_{2,i} = 20$m, $b_{2,i} = 15$m, $c_{2,i} = 15$m, $\theta_{1,o} = 0^o$, $\theta_{1,i} = 0^o$, $\theta_{2,o} = 0^o$, $\theta_{2,i} = 0^o$, $d = 100$).

Furthermore, as far as generalization of the proposed model is concerned, we show that some notable geometrical channel models in the literature can be deduced from our proposed generalized model by substituting some suitable values for certain parameters listed in Table 5.1. Using these parameters, we plotted the PDF of AoA in azimuth plane for M2M and F2M as shown in Fig. 5.23(a) and Fig. 5.23(b), respectively. From Fig. 5.23 and Table 5.1, it is verified that these models are the special cases of our generalized 3D geometrical model.

5.5   Conclusion

In this chapter, a 3D generalized and realistic geometrical model for M2M communication environments has been proposed. Hollow rotatable semi-ellipsoids with variable dimensions in all axes have been considered around both the ends of communication link to model the scattering region. Joint and marginal PDFs of AoA, observed at both the ends of communication links, have been derived. Furthermore, using the proposed model, closed-form expressions for the trivariate PDF of ToA in correspondence with azimuth and elevation AoA have been derived. The obtained theoretical results have been presented along with a comprehensive

TABLE 5.1: Comparison of the proposed model with the existing 2D and 3D channel models.

Scattering Model	Communication Scenarios	Corresponding Substitutions	Respective Scattering Models	Geometry of Scattering Regions
Proposed	M2M	-	3D Hollow Ellipsoidal Model	
Riaz *et al.* [49]	M2M	$a_{m,i} = b_{m,i} = c_{m,i} = 0$	3D Ellipsoidal Model	
Baltzis *et al.* [41]	M2M	$c_{m,q} \to 0$	2D Hollow Elliptical Model	
Baltzis *et al.* [2]	M2M	$a_{m,i} = b_{m,i} = 0$, and $c_{m,q} \to 0$	2D Elliptical Model	
Paul *et al.* [38]	M2M	$a_{m,o} = b_{m,o} = R_o$, $a_{m,i} = b_{m,i} = R_i$, and $c_{m,q} \to 0$	2D Hollow Circular Model	
Paul *et al.* [1]	M2M	$a_{m,o} = b_{m,o} = R$, $a_{m,i} = b_{m,i} = c_{m,i} = 0$, and $c_{m,o} \to 0$	2D Circular Model	
Olenko *et al.* [60]	F2M	$a_{1,q} = b_{1,q} = c_{1,q} = 0, a_{2,i} = b_{2,i} = c_{2,i} = 0$, and $a_{2,o} = b_{2,o} = c_{2,o} = R$	3D Hemispheroid Model	
Piechocki *et al.* [61]	F2M	$a_{1,q} = b_{1,q} = c_{1,q} = 0, a_{2,i} = b_{2,i} = c_{2,i} = 0$, and $c_{2,o} \to 0$	2D Elliptical Model	
Noor *et al.* [62]	F2M	$a_{1,q} = b_{1,q} = c_{1,q} = 0, a_{2,o} = b_{2,o} = R_o, a_{2,i} = b_{2,i} = R_i$ and $c_{2,q} \to 0$	2D Hollow Disk Model	
Petrus *et al.* [18]	F2M	$a_{1,q} = b_{1,q} = c_{1,q} = 0, a_{2,i} = b_{2,i} = c_{2,i} = 0, a_{2,o} = b_{2,o} = R$ and $c_{2,o} \to 0$	2D Circular Model	

and meticulous analysis. The effect of various parameters on the PDF of AoA and ToA have been discussed in detailed. It has been established that it is significantly important to consider the propagation of multipath signals in 3D space to model the propagation environment more realistically. In order to validate the proposed results, a thorough comparison of the proposed model with notable model in the literature has been presented. The results obtained from such geometrical models can be used as a theoretical reference for the practical experiments and can be helpful to design precise communication equipment for enhancing the data rates.

Chapter 6

CONCLUSIONS AND FUTURE DIRECTIONS

This chapter concludes the dissertation in Section 6.1 and presents future research work in Section 6.2 on the basis of research work carried out in this dissertation.

6.1 Conclusions

In this dissertation, we have proposed a 3D semi-ellipsoid geometrical channel model for M2M radio propagation environment. It has been assumed that the MSs are surrounded by uniformly distributed scatterers within the semi-ellipsoid geometrical shape. In order to model M2M communication environment realistically, a flexible geometry of the semi-ellipsoids has been employed whose dimensions are made adjustable and rotatable about their vertical axes according to the directions of the MSs and the shapes of the streets and canyons where MSs reside. Using the developed geometrical channel model, expressions for the joint and marginal probability distribution functions (PDFs) of angle-of-arrival (AoA) and time-of-arrival (ToA) in azimuth and elevation planes have been derived. Mobility, being an important parameter in radio mobile channel modeling, has been analyzed through the characterization of Doppler spectrum of the developed channel model. Respective analysis includes joint PDF of the normalized Doppler shift and elevation AoA, marginal PDF of normalized Doppler for specific values of elevation angles and distribution of normalized Doppler spread with respect to direction of relative motion. Furthermore, the proposed 3D semi-ellipsoid geometrical channel model has been extended by developing a more realistic and generalized 3D channel model M2M communication environment. The generalized 3D spatial channel model consists of concentric semi-ellipsoids such that the inner semi-ellipsoids are scatter-free regions and uniformly distributed scatterers reside outside the inner and inside the outer semi-ellipsoids. It has been assumed that the semi-ellipsoids around each MS are independently rotatable about the vertical axis. In order to

make the scattering region around the MSs more realistic, a bound on the dimensions of the semi-ellipsoids has been applied i.e., the semi-major axis and height of the inner semi-ellipsoid should be lesser than the semi-minor axis and height of the outer semi-ellipsoid. By exploiting the generalized 3D channel model, mathematical expressions for the joint and marginal PDFs of AoA and ToA in azimuth and elevation planes have been derived. These spatial and temporal characteristics have been analyzed for various channel parameters like elevation and orientation of each of the semi-ellipsoids.

The model has been validated through its comparison with simulation results. For this purpose, uniformly distributed scatterers have been created as point objects within semi-ellipsoidal geometrical scattering regions. Using the simulation setup, PDF curves of the AoA and ToA have been plotted and compared with the analytical curves, where an excellent agreement has been seen. The model has also been validated by comparing its results with those reported in the literature for measurement campaigns for various channel scenarios. Moreover, generalization of the model has been confirmed by its comparisons with various existing geometrical models. It has been shown that some notable geometrical channel models for F2M and M2M communication environments in the literature could be deduced from the proposed generalized model through the substitution of certain suitable values for a few channel parameters.

6.2 Future Work

In future, we plan to extend the developed 3D spatial channel models for multibounce propagation to make them more realistic for fulfilling the requirements of the M2M communication environment. Furthermore, in view of the suggestions and comments of the reviewers of this dissertation and of the papers published during the PhD research study, the model characterization can also be extended to the study of power delay spectrum, power angular spectrum and power azimuth spectrum.

REFERENCES

[1] B. Paul, A. Hasan, H. Madheshiya, and R. Bhattacharjee, "Time and angle of arrival statistics of mobile-to-mobile communication channel employing circular scattering model," *IETE Journal of Research*, vol. 55, no. 6, p. 275, 2009.

[2] K. Baltzis, "A simplified geometric channel model for mobile-to-mobile communications," *Radioengineering*, vol. 20, no. 4, p. 961, 2011.

[3] K. I. Pedersen, P. E. Mogensen, and B. H. Fleury, "A stochastic model of the temporal and azimuthal dispersion seen at the base station in outdoor propagation environments," *IEEE Trans. Veh. Technol.*, vol. 49, no. 2, pp. 437–447, 2000.

[4] C. S. Raghavendra, K. M. Sivalingam, and T. Znati, *Wireless sensor networks.* Springer, 2004.

[5] J. Macker and S. Corson, "Mobile ad hoc networks (MANET)," 1997.

[6] H. Hartenstein and K. P. Laberteaux, "A tutorial survey on vehicular ad hoc networks," *IEEE Commun. Magazine*, vol. 46, no. 6, pp. 164–171, 2008.

[7] T. Vaa, M. Penttinen, and I. Spyropoulou, "Intelligent transport systems and effects on road traffic accidents: state of the art," *IET Intelligent Transport Systems*, vol. 1, no. 2, pp. 81–88, 2007.

[8] W. C. Y. Lee, *Communications Engineering.* McGraw Hill, 1982.

[9] G. Karagiannis, O. Altintas, E. Ekici, G. Heijenk, B. Jarupan, K. Lin, and T. Weil, "Vehicular networking: A survey and tutorial on requirements, architectures, challenges, standards and solutions," *IEEE Commun. Surveys and Tutorials*, vol. 13, no. 4, pp. 584–616, 2011.

[10] H. Wu, R. M. Fujimoto, G. F. Riley, and M. Hunter, "Spatial propagation of information in vehicular networks," *IEEE Trans. Veh. Technol.*, vol. 58, no. 1, pp. 420–431, 2009.

[11] A. Akki and F. Haber, "A statistical model of mobile-to-mobile land communication channel," *IEEE Trans. Veh. Technol.*, vol. 35, no. 1, pp. 2–7, Feb. 1986.

[12] G. L. Stüber, *Principles of mobile communication.* Springer Verlag, 2011.

[13] R. Clarke, "A statistical theory of mobile radio reception," *Bell System Technical Journal*, vol. 47, pp. 957–1000, 1968.

[14] T. Aulin, "A modified model for the fading signal at a mobile radio channel," *IEEE Trans. Veh. Technol.*, vol. 28, pp. 182–203, Aug. 1979.

[15] A. S. Akki, "Statistical properties of mobile-to-mobile land communication channels," *IEEE Trans. Veh. Technol.*, vol. 43, no. 4, pp. 826–831, Nov 1994.

[16] M. K. Simon and M. S. Alouini, *Digital communication over fading channels.* Wiley. com, 2005, vol. 95.

[17] R. B. Ertel and H. J. Reed, "Angle and time of arrival statistics for circular and elliptical scattering models," *IEEE Journal on Selected Areas in Communications*, vol. 17, no. 11, pp. 1829–1840, 1999.

[18] P. Petrus, J. H. Reed, and T. S. Rappaport, "Geometrical-based statistical macrocell channel model for mobile environments," *IEEE Trans. Commun.*, vol. 50, no. 3, pp. 495–502, 2002.

[19] J. C. Liberti and T. S. Rappaport, "A geometrically based model for line-of-sight multipath radio channels," in *Proc. IEEE Veh. Tech. conf.*, pp. 844–848.

[20] M. P. Lötter and P. V. Rooyen, "Modeling spatial aspects of cellular cdma/sdma systems," *IEEE Trans. Comm. Lett.*, vol. 3, no. 5, pp. 128–131, May 1999.

[21] R. Janaswamy, "Angle and time of arrival statistics for the gaussian scatter density model," *IEEE Trans. Wireless Comm.*, vol. 1, no. 3, pp. 488–497, Jul. 2002.

[22] Y. Chen and V. K. Dubey, "Accuracy of geometric channel-modeling methods," *IEEE Trans. Veh. Technol.*, vol. 53, no. 1, pp. 82–93, 2004.

[23] K. B. Baltzis and J. N. Sahalos, "A simple 3D geometric channel model for macrocell mobile communications," *Wireless Personal Communications*, vol. 51, no. 2, pp. 329–347, 2009.

[24] A. Borhani and M. Patzold, "Time-of-arrival, angle-of-arrival, and angle-of-departure statistics of a novel simplistic disk channel model," in *Proc. Signal Processing and Communication Systems (ICSPCS)*. IEEE, 2011, pp. 1–7.

[25] S. Qu and T. Yeap, "A three-dimensional scattering model for fading channels in land mobile environment," *IEEE Trans. Veh. Technol.*, vol. 48, no. 3, pp. 765–781, 1999.

[26] R. Janaswamy, "Angle-of-arrival statistics for a 3D spheroid model," *IEEE Trans. Veh. Technol.*, vol. 51, no. 5, pp. 1242–1247, 2002.

[27] S. J. Nawaz, B. H. Qureshi, and N. M. Khan, "A generalized 3D scattering model for a macrocell environment with a directional antenna at the BS," *IEEE Trans. Veh. Technol.*, vol. 59, no. 7, pp. 3193–3204, Sept. 2010.

[28] F. Vatalaro and A. Forcella, "Doppler spectrum in mobile-to-mobile communications in the presence of three-dimensional multipath scattering," *IEEE Trans. Veh. Technol.*, vol. 46, no. 1, pp. 213–219, Feb. 1997.

[29] M. Pätzold, B. O. Hogstad, N. Youssef, and D. Kim, "A MIMO mobile-to-mobile channel model: Part I- the reference model," in *Proc. IEEE 16th International Symp. on Personal, Indoor and Mobile Radio Communications (PIMRC)*, vol. 1, 2005, pp. 573–578.

[30] A. G. Zajić and G. L. Stüber, "Space-time correlated MIMO mobile-to-mobile channels," in *Proc. IEEE 17th International Symp. on Personal, Indoor and Mobile Radio Communications (PIMRC)*, 2006, pp. 1–5.

[31] C. Wei, H. Zhiyi, and Z. Lili, "A reference model for MIMO mobile-to-mobile fading channel," in *Proc. of International Conference on Wireless Communications, Networking and Mobile Computing*. IEEE, 2007, pp. 228–231.

[32] M. Pätzold, B. Hogstad, and N. Youssef, "Modeling, analysis, and simulation of MIMO mobile-to-mobile fading channels," *IEEE Trans.Wireless Commun.*, vol. 7, no. 2, pp. 510–520, 2008.

[33] M. Riaz and N. M. Khan, "Closed-form expressions for correlation function and power density spectrum in MIMO mobile-to-mobile channels using two-erose-ring model," in *Proc. IEEE International Conference on Information and Communication Technologies (ICICT)*, 2011, pp. 1–5.

[34] T. Wu and C. Kuo, "3D space-time-frequency correlation functions of mobile-to-mobile radio channels," in *Proc. IEEE Veh. Techn. Conf.*, 2007, pp. 334–338.

[35] A. G. Zajic and G. Stuber, "Space-time correlated mobile-to-mobile channels: modelling and simulation," *IEEE Trans. Veh. Technol.*, vol. 57, no. 2, pp. 715–726, 2008.

[36] L. Wang, W. Liu, and Y. Cheng, "Statistical analysis of a mobile-to-mobile rician fading channel model," *IEEE Trans. Veh. Technol.*, vol. 58, no. 1, pp. 32–38, 2009.

[37] A. Zajić and G. Stüber, "Three-dimensional modeling, simulation, and capacity analysis of space-time correlated mobile-to-mobile channels," *IEEE Trans. Veh. Technol.*, vol. 57, no. 4, pp. 2042 –2054, july 2008.

[38] B. Paul and R. Bhattacharjee, "Time and angle of arrival statistics of mobile-to-mobile communication channel employing dual annular strip model," *IETE Journal of Research*, vol. 56, no. 6, p. 327, 2010.

[39] P. Samarasinghe, T. Lamahewa, T. Abhayapala, and R. Kennedy, "3D mobile-to-mobile wireless channel model," in *Proc. Australian Communications Theory Workshop*, Feb. 2010, pp. 30–34.

[40] T. Batool, P. Matthias *et al.*, "A geometrical three-ring-based model for MIMO mobile-to-mobile fading channels in cooperative networks," *EURASIP Journal on Advances in Signal Processing*, 2011.

[41] K. Baltzis, "A generalized elliptical scattering model for the spatial characteristics of mobile channels," *Wireless Personal Communications*, pp. 1–14, 2011.

[42] A. F. Molisch, *Wireless communications.* Wiley. com, 2010, vol. 15.

[43] K. Le, "On angle-of-arrival and time-of-arrival statistics of geometric scattering channels," *IEEE Trans. Veh. Technol.*, vol. 58, no. 8, pp. 4257–4264, 2009.

[44] I. Jaafar, H. Boujemaa, and M. Siala, "Angle and time of arrival statistics for hollow-disc and elliptical scattering models," in *Proc. Signals, Circuits and Systems (SCS)*, 2008, pp. 1–4.

[45] N. M. Khan, M. T. Simsim, and P. B. Rapajic, "A generalized model for the spatial characteristics of the cellular mobile channel," *IEEE Trans. Veh. Technol.*, vol. 57, no. 1, pp. 22–37, 2008.

[46] S. J. Nawaz, N. M. Khan, M. N. Patwary, and M. Moniri, "Effect of directional antenna on the doppler spectrum in 3D mobile radio propagation environment," *IEEE Trans. Veh. Technol.*, vol. 60, no. 7, pp. 2895 –2903, Sept. 2011.

[47] K. Leung and S.-N. Suen, *Vectors, Matrices and Geometry.* Hong Kong University Press, 1994, vol. 1.

[48] A. Kuchar, J. P. Rossi, and E. Bonek, "Directional macro-cell channel characterization from urban measurements," *IEEE Trans. Antennas and Propag.*, vol. 48, no. 2, pp. 137–146, Feb. 2000.

[49] M. Riaz, S. J. Nawaz, and N. M. Khan, "3D ellipsoidal model for mobile-to-mobile radio propagation environments," *Wireless Personal Communications*, vol. 72, no. 4, pp. 2465–2479, Oct. 2013.

[50] C. S. Patel, G. L. Stuber, and T. G. Pratt, "Simulation of rayleigh-faded mobile-to-mobile communication channels," *IEEE Trans. Commun.*, vol. 53, no. 11, pp. 1876–1884, 2005.

[51] A. Zajić and G. Stüber, "Three-dimensional modeling and simulation of wideband mimo mobile-to-mobile channels," *IEEE Trans. Wireless Commun.*, vol. 8, no. 3, pp. 2042 –2054, Mar. 2009.

[52] S. Qu, "An analysis of probability distribution of doppler shift in three-dimensional mobile radio environments," *IEEE Trans. Veh. Technol.*, vol. 58, no. 4, pp. 1634–1639, 2009.

[53] M. Walter, D. Shutin, and U.-C. Fiebig, "Delay-dependent doppler probability density functions for vehicle-to-vehicle scatter channels," *IEEE Trans. Antenna and propagation*, vol. 62, no. 4, pp. 2238–2249, Apr.

[54] ——, "Joint delay doppler probability density functions for air-to-air channels," *International Journal of Antennas and Propagation*, vol. 2014, pp. 1–11, 2014.

[55] G. L. Stüber, *Principles of mobile communication.* Springer, 2011.

[56] R. Verdone and A. Zanella, *Pervasive Mobile and Ambient Wireless Communications: COST Action 2100.* Springer, 2012.

[57] T. Abbas, "Measurement based channel characterization and modeling for vehicle-to-vehicle communications," *http://lup.lub.lu.se/record/4251789*, 2014.

[58] T. Abbas, K. Sjöberg, J. Karedal, and F. Tufvesson, "A measurement based shadow fading model for vehicle-to-vehicle network simulations," *arXiv preprint arXiv:1203.3370*, 2012.

[59] J. Maurer, W. Sörgel, and W. Wiesbeck, "Ray-tracing for vehicle-to-vehicle communications," in *Proc. URSI-GA*, 2005.

[60] A. Y. Olenko, K. T. Wong, and E. Hui-On Ng, "Analytically derived ToA-DoA statistics of uplink/downlink wireless multipaths arisen from scatterers on a hollow-disc around the mobile," *IEEE Antennas and Wireless Propagation Letters*, vol. 2, no. 1, pp. 345–348, 2003.

[61] R. J. Piechocki, G. V. Tsoulos, and J. P. McGeehan, "Simple general formula for PDF of angle of arrival in large cell operational environments," *Electronics Letters*, vol. 34, no. 18, pp. 1784–1785, 1998.

[62] N. M. Khan, "Modeling and characterization of multipath fading channels in cellular mobile communication systems," Ph.D. dissertation, University of New South Wales, 2006.